

Marquette University

e-Publications@Marquette

---

Dissertations (1934 -)

Dissertations, Theses, and Professional  
Projects

---

## Intrinsic Photodynamic Study on Photocatalytic Materials

Wenhui Hu

*Marquette University*

Follow this and additional works at: [https://epublications.marquette.edu/dissertations\\_mu](https://epublications.marquette.edu/dissertations_mu)



Part of the [Chemistry Commons](#)

---

### Recommended Citation

Hu, Wenhui, "Intrinsic Photodynamic Study on Photocatalytic Materials" (2022). *Dissertations (1934 -)*. 1140.

[https://epublications.marquette.edu/dissertations\\_mu/1140](https://epublications.marquette.edu/dissertations_mu/1140)

INTRINSIC PHOTODYNAMIC STUDY ON PHOTOCATALYTIC MATERIALS

By

Wenhui Hu

A Dissertation submitted to the Faculty of the Graduate School,

Marquette University,

in Partial Fulfillment of the Requirements

for the Degree of Doctor of Philosophy

Milwaukee, Wisconsin

May 2022

## ABSTRACT

### INTRINSIC PHOTODYNAMIC STUDY ON PHOTOCATALYTIC MATERIALS

Wenhui Hu

Marquette University 2021

To relieve the global energy crisis and environmental pollution caused by the combustion of traditional fossil fuels, developing an environmental-friendly renewable energy to replace fossil fuel is urgent. Among the possible energy sources, solar energy has attracted numerous attentions because of the abundant storage. However, it is challenging to efficiently utilize and store solar energy. One attractive strategy to address this challenge is to convert solar energy to fuel through artificial photosynthesis (e.g. photocatalytic water splitting to generate  $H_2$ ). A technologically significant solar-driven water splitting system requires an efficient photocatalytic system that can not only effectively harvest light but also can perform the subsequent charge separation and catalytic reaction. The objective of my research projects is to develop such photocatalytic materials that can be used as light absorption and charge separation materials for light driven proton reduction to generate hydrogen. The materials that were of interest include semiconductor nanocrystals and porous crystalline materials. To establish their structure and property relationship, a suit of advanced spectroscopic methods including steady state absorption and emission spectroscopy, time resolved optical and X-ray absorption spectroscopy were used to examine their excited state, energy transfer, and charge separation dynamics during photoinduced reaction.

One class of semiconductor photocatalytic materials that I have studied were  $CuInS_2$  quantum dots. The dependence of carrier dynamics of  $CuInS_2$  quantum dots on their sizes are presented in chapter 3. Their photocatalytic activity together with catalytic mechanism for visible light driven hydrogen generation are discussed in chapter 4.

Zeolitic imidazolate frameworks (ZIFs), a subclass of metal organic frameworks (MOFs), are the second class of materials that I have investigated. The impact of the chemical compositions on ZIFs on their photophysical and photocatalytic property are discussed in chapter 5 and chapter 6. The energy transfer dynamics from the encapsulated chromophores to ZIFs is discussed in chapter 7 and chapter 8.

## ACKNOWLEDGEMENTS

Wenhui Hu

First and foremost, I would like to express my sincere gratitude to my advisor, Prof. Jier Huang for her continuous support of my PhD study and research. Without her patient guidance and encouragement, the goal of my work would not have been realized. I could not have imagined having a better advisor for my PhD work. I would also like to express my sincere appreciation to the members of our group, without their help, the PhD work will be more difficult.

Besides my advisor, I would like to thank my committee, Prof. Adam Fiedler, Prof. James Gardinier, Prof. James Kincaid and Prof. Reid, for their extensive professional guidance, insightful comment and encouragement. I'd like to acknowledge the assistance from the faculty in Chemistry department that provide a positive and collaborative environment for research.

My sincere thanks also go to Dr. Xiaoyi Zhang at Advanced Photon Source of Argonne National laboratory for training me the measurement and understanding of the time-resolved X-ray absorption spectroscopy which is very important in my research.

I would like to thank our collaborators, Dr. Jing Gu from San Diego State University and Dr. John Berry from University of Wisconsin-Madison, for their effective collaboration.

Last but not least, I would like to thank my family members, for supporting me all the time during my life.

## Table of Contents

ACKNOWLEDGEMENTS .....	i
LIST OF TABLES .....	iv
LIST OF FIGURES .....	v
Chapter 1 .....	1
Introduction.....	1
1.1 Why solar energy?.....	1
1.2 The conversion of solar energy to fuels .....	1
1.3 Semiconductor quantum dots as light harvesting materials .....	3
1.3.1 Intrinsic optical properties of CuInS <sub>2</sub> quantum dots .....	7
1.3.2 Photocatalytic hydrogen generation by CuInS <sub>2</sub> .....	11
1.4 Zeolitic imidazolate frameworks as photocatalytic material.....	12
1.4.1 Intrinsic light harvesting properties of zeolitic imidazolate frameworks .....	13
1.4.2 Photocatalytic properties of zeolitic imidazolate frameworks .....	19
Chapter 2.....	24
Experiment and Characterization.....	24
2.1 Standard Characterization .....	24
2.2. Experimental Details for Chapter 3.....	27
2.3. Experimental Details for Chapter 4.....	27
2.4. Experimental Details for Chapter 5.....	29
2.5. Experimental Details for Chapter 6.....	30
2.6. Experimental Details for Chapter 7.....	32
2.7. Experimental Details for Chapter 8.....	33
Chapter 3.....	36
Unravelling the Correlation of Electronic Structure and Carrier Dynamics in CuInS <sub>2</sub> Nanoparticles .....	36
3.1 Introduction .....	36
3.2 Results and discussion.....	37
3.3 Conclusion.....	48
Chapter 4.....	50
Composition Effect on the Carrier Dynamics and Catalytic Performance of CuInS <sub>2</sub> /ZnS Quantum Dots for Light Driven Hydrogen Generation.....	50

4.1 Introduction .....	50
4.2 Results and discussion.....	51
4.3 Conclusion.....	63
Chapter 5.....	64
The Impact of Coordination Ligand on Electronic Structure and Photophysical properties of Zeolitic imidazolate Frameworks (ZIFs).....	64
5.1 Introduction .....	64
5.2 Results and discussion.....	66
5.3 Conclusion.....	78
Chapter 6.....	79
Enhanced ZIF-67 Photocatalytic Hydrogen Generation Efficiency of ZIF-67 due to Imidazole Doping.....	79
6.1 Introduction .....	79
6.2 Results and discussion.....	80
6.3 Conclusion.....	88
Chapter 7.....	89
Distance Dependent Energy Transfer Dynamics from Molecular Donor to Zeolitic Imidazolate Framework Acceptor.....	89
7.1 Introduction .....	89
7.2 Results and discussion.....	90
7.3 Conclusion.....	99
Chapter 8.....	100
Energy Transfer Dynamics of Rhodamine B encapsulated Zeolitic imidazolate Frameworks.....	100
8.1 Introduction .....	100
8.2 Results and Discussion.....	101
8.3 Conclusion.....	108
Chapter 9.....	110
Conclusion and Future work.....	110
9.1 Conclusion and future work of CuInS <sub>2</sub> .....	110
9.2 Conclusion and future work of zeolitic imidazolate frameworks (ZIFs).....	112
Reference .....	116

## LIST OF TABLES

**Table 2-1.** The varied amount of imidazole in the synthesis of Im-ZIF-67.

**Table 2-2.** The amount of metal precursor in different samples.

**Table 3-1.** XAFS fitting parameters for CIS.

**Table 3-2.** Fitting Parameters for TA Kinetics of CIS NPs.

**Table 4-1.** EDX results and sample name of CIS/ZnS with different Cu to In ratios.

**Table 4-2.** Fitting Parameters for PL decays of CIS/ZnS with different Cu to In ratios.

**Table 4-3.** Fitting Parameters for TA kinetics decays of CIS/ZnS with different Cu to In ratios.

**Table 5-1.** Mulliken charges on N center in different imidazole.

**Table 5-2.** Mulliken charges on Co center in 1 unit of ZIF.

**Table 5-3.** Fitting time constants of TA kinetics under 1200 nm excitation.

**Table 5-4.** Kinetics fitting results of ZIFs under 350 nm excitation.

**Table 6-1.** the percentage of Im in starting materials and final products.

**Table 7-1.** Al<sub>2</sub>O<sub>3</sub> film thickness at different ALD cycles.

**Table 7-2.** The half lifetime of RuN<sub>3</sub> GSB on different films and estimated ENT time and efficiency of RuN<sub>3</sub>/Al<sub>2</sub>O<sub>3</sub>/ZIF-67.

**Table 8-1.** Energy transfer parameter of RB-CoZIF-8 system.

**Table 8-2.** RB concentration in different samples.

**Table 8-3.** ICP results of Co concentration in different samples.

## LIST OF FIGURES

**Figure 1-1** Schematic diagram of natural photosynthesis.

**Figure 1-2** Schematic diagram of artificial photosynthesis.

**Figure 1-3** Schematic representation of the hybrid photocatalyst system.

**Figure 1-4** Cartoon of charge separation dynamics in CdSe QDs through electron transfer to NiS and hole transfer to AA.

**Figure 1-5** (a) Schematic representation of the photocatalyst system developed in this work; (b) UV-vis absorption spectra of ZnSe quantum dots.

**Figure 1-6** Optical band gaps for ternary I-III-VI semiconductors with particle size from 2 nm to 5 nm.

**Figure 1-7** Illustration diagrams of the three main tuning methods.

**Figure 1-8** UV-vis absorption (a) and emission spectra (b) of CuInS<sub>2</sub> with different nanoparticle size.

**Figure 1-9** (a) Photograph of the resulting CuInS<sub>2</sub> samples with different [Cu]/[In] molar ratio in toluene and corresponding picture under a UV lamp. (b) Absorption and emission spectra of as-prepared CuInS<sub>2</sub> NCs with different [Cu]/[In] molar ratios.

**Figure 1-10** Illustration of photoelectrochemical water splitting.

**Figure 1-11.** (a) UV-Vis-Near IR absorption spectrum of ZIF-67 thin film. The inset shows the synthetic scheme for the formation of ZIF-67 crystal; (b) The schematic representation of energy diagram of Co<sup>2+</sup> (T<sub>d</sub>) and excited state relaxation of ZIF-67; (c) The kinetic trace of ZIF-67 TA spectra (inset) at 610 nm; (d) XANES spectrum of ZIF-67 at Co K edge before (laser-off) and 500 ps after (laser-on) laser excitation. The difference spectrum is obtained by subtracting the laser-off spectrum from laser-on spectrum.

**Figure 1-12.** (a) UV-visible-near IR absorption spectrum of Co[im\*]<sup>-</sup><sub>2</sub>. The inset shows the molecular structure of Co[im\*]<sup>-</sup><sub>2</sub>; (b) XANES spectrum of Co[im\*]<sup>-</sup><sub>2</sub> and Co(NO<sub>3</sub>)<sub>2</sub>·6H<sub>2</sub>O at Co K edge. The inset shows the EXAFS spectrum in R-space and its fitting; (c) TA spectra of Co[im\*]<sup>-</sup><sub>2</sub> following 1000 nm excitation; (d) The kinetic trace at 580 nm representing ground state bleach recovery.

**Figure 1-13.** (a) The schematic representation of ECS formation pathway in Zn or Cu doped ZIF-67; (b) The kinetic traces of the ECS state at 610 nm and the ground state bleach (GSB, inset) at 585 nm for ZIF-67 with variable Co:Zn ratios; (c) ECS and GSB traces for Cu@ZIF-67 with variable % Cu (c); (d) Representative Cu K-edge XANES spectrum (black line) and XTA difference spectra at the Cu K-edge for Cu@ZIF-67 after 590 nm excitation at 120 and 500 ps time delays.

**Figure 1-13.** (a) The schematic representation of ECS formation pathway in Zn or Cu doped ZIF-67; (b) The kinetic traces of the ECS state at 610 nm and the ground state bleach (GSB, inset) at 585 nm for ZIF-67 with variable Co:Zn ratios; (c) ECS and GSB traces for Cu@ZIF-67 with variable % Cu (c); (d) Representative Cu K-edge XANES spectrum (black line) and XTA difference spectra at the Cu K-edge for Cu@ZIF-67 after 590 nm excitation at 120 and 500 ps time delays.

**Figure 1-14.** (a) TA spectra of  $[\text{Ru}(\text{bpy})_3]^{2+}$  on ZIF-67 and  $\text{Al}_2\text{O}_3$  control (inset) following 410 nm excitation; (b) The comparison of TA kinetics of  $[\text{Ru}(\text{bpy})_3]^{2+}$  excited state decay (b) and ground state bleach (c) between  $\text{Al}_2\text{O}_3$  and ZIF-67; The inset of (c) is the XTA spectra of ZIF-67 at Co k-edge upon the excitation of  $[\text{Ru}(\text{bpy})_3]^{2+}$  at 400nm. (d) The full-time profile of  $\text{H}_2$  evolution under the optimized catalytic conditions.

**Figure 1-15.** (a) Possible reaction mechanism for the Co-ZIF-9 cocatalyzed photoreduction of  $\text{CO}_2$  employing CdS as the light harvester; (b) the dependence of the wavelength of incident light on the evolution of CO and  $\text{H}_2$  from the Co-ZIF-9 promoted  $\text{CO}_2$  photoreduction system. The histogram represents the production of CO and  $\text{H}_2$ . The lines are the UV–Vis diffuse reflectance spectrum of CdS (solid) and Co-ZIF-9 (dash); (c) PL spectra of the reaction systems under 400 nm laser irradiation at room temperature; (d) Schematic illustration of  $\text{CO}_2$  photoreduction process of  $\text{CsPbBr}_3/\text{ZIFs}$ ; (e) time-resolved PL decay plots of  $\text{CsPbBr}_3$  and  $\text{CsPbBr}_3/\text{ZIFs}$ .

**Figure 3-1.** XRD patterns of CIS NPs synthesized with nucleation time 15, 30, and 60 min.

**Figure 3-2.** (a) SAXS data (symbols) and fit (solid lines) using spherical particle model whose size follows log-normal distribution. (b) Particle radius distribution yielded from the SAXS data fitted under spherical shape assumption of CIS NPs synthesized with nucleation time 15, 30, and 60 min.

**Figure 3-3.** UV–visible absorption spectra (a) and emission spectra (b) of CIS NPs synthesized with different nucleation time.

**Figure 3-4.** Comparison of XANES spectra (a) and Fourier-transformed EXAFS spectra (b) of CIS NPs synthesized with different nucleation time. Inset: first derivative of the XANES spectra

**Figure 3-5.** XAFS spectra (open dot) and the best fit (solid line) of CIS NPs in R-space and k space with nucleation times 15 min (a, b), 30 min (c, d), and 60 min (e, f), respectively.

**Figure 3-6.** Femtosecond OTA spectra of CIS NPs with 15 mins (a), 30 mins (b), and 60 mins nucleation time following 480 nm excitation. (d) The comparison of 1 ps TA spectra of CIS NPs.

**Figure 3-7.** The comparison of OTA kinetic traces of CIS NPs at various probe wavelengths for samples with 15 mins (a), 30 mins (b), and 60 mins (c) nucleation time following 480 nm excitation. (d) The comparison of ground state bleach recovery kinetics (inverted) for 15min, 30 mins, and 60 mins samples. These kinetic traces are normalized at 5 ns for better comparison.

**Figure 3-8.** (a) XANES spectrum (black plot) and difference XANES spectrum (red plot) of CIS NPs with 60 min nucleation time at Cu K-edge. The difference XANES spectrum was obtained after subtracting the XANES spectrum without laser excitation from the XANES spectrum collected at 110 ps after laser excitation. (b) Scheme illustration of carrier dynamics in CIS NPs following photoexcitation.

**Figure 4-1.** XRD patterns (a), UV-visible absorption spectra (b) and Mott-Schottky plots (c) for CIS/ZnS QDs with different Cu to In ratios.

**Figure 4-2.** (a) emission spectra, (b) the plots of integrated fluorescence intensity vs absorbance, and (c) emission lifetime decay kinetics of CIS/ZnS QDs with different Cu to In ratios. The excitation wavelength for emission spectra and emission lifetime measurement is at 400 nm. The probing wavelength is 600 nm, 580 nm, 550 nm, and 550 nm for samples with  $\text{Cu}_{0.54}\text{InS}_2$ ,  $\text{Cu}_{0.28}\text{InS}_2$ ,  $\text{Cu}_{0.17}\text{InS}_2$  and  $\text{Cu}_{0.12}\text{InS}_2$ , respectively.

**Figure 4-3.** Femtosecond transient absorption spectra of CIS/ZnS QDs with different Cu to In ratios: (a)  $\text{Cu}_{0.54}\text{InS}_2$ ; (b)  $\text{Cu}_{0.28}\text{InS}_2$ ; (c)  $\text{Cu}_{0.17}\text{InS}_2$ ; (d)  $\text{Cu}_{0.12}\text{InS}_2$ . The excitation wavelength is at 400 nm.

**Figure 4-4.** The TA spectra of  $\text{Cu}_{0.54}\text{InS}_2$  (a) and  $\text{Cu}_{0.12}\text{InS}_2$  (b) following 450 nm excitation. The inset shows the early time spectra. The comparison of kinetic traces of electron absorption at 650 nm following 400 nm and 450 nm excitation for  $\text{Cu}_{0.54}\text{InS}_2$  (c) and  $\text{Cu}_{0.12}\text{InS}_2$  (d).

**Figure 4-5.** (a) The comparison of exciton bleach recovery for  $\text{Cu}_{0.54}\text{InS}_2$ ,  $\text{Cu}_{0.28}\text{InS}_2$ , and  $\text{Cu}_{0.17}\text{InS}_2$ . (b) The comparison of kinetic traces of electron absorption decay of CIS/ZnS QDs at 650 nm with different Cu to In ratios. The excitation wavelength is at 400 nm.

**Figure 4-6.**  $\text{H}_2$  generation time profile of CIS/ZnS QDs with four different Cu to In ratios under 405 nm illumination with 3 mW power. AA is used as the proton source and sacrificial electron donor.

**Figure 4-7.** Stern-Volmer plots of prepared CIS/ZnS QDs: a)  $\text{Cu}_{0.54}\text{InS}_2$ ; b)  $\text{Cu}_{0.28}\text{InS}_2$ ; c)  $\text{Cu}_{0.17}\text{InS}_2$  and d)  $\text{Cu}_{0.12}\text{InS}_2$  inset: the emission spectra of prepared CIS/ZnS QDs in the presence of different concentrations of AA.

**Figure 5-1.** XRD (a), X-ray absorption near edge structure spectra (b) and fourier transformed extended X-ray absorption fine structure (EXAFS) spectra (c) of prepared ZIFs

**Figure 5-2.** SEM images of prepared ZIFs.

**Figure 5-3.** (a) UV-vis-NIR diffuse reflectance spectra of ZIFs (b) Calculated transitions in ZIFs.

**Figure 5-4.** Femtosecond transient absorption (TA) spectra of ZIFs under 1200 nm excitation: a) ZIF-67 and b) ZIF-9; Kinetics traces of ground bleach feature recovery (GSB) (c) and charge separation state at 609 nm (d).

**Figure 5-5.** Femtosecond transient absorption (TA) spectra of ZIFs under 350 nm excitation: a) ZIF-67; b) ZIF-9 and c) ZIF-65, Inset: early time TA spectra of each sample.

**Figure 5-6.** Kinetics traces of ZIFs at different wavelength under 350 nm excitation.

**Figure 6-1.** a) XRD patterns of ZIF-67 and Im doped ZIF-67; b) X-ray absorption near edge structure of ZIF-67 based samples.

**Figure 6-2.** SEM images of ZIF-67 and Im doped ZIF-67.

**Figure 6-3.** UV-visible absorption spectra of ZIF-67 based samples.

**Figure 6-4.** Femtosecond transient absorption spectra of ZIF-67 (a), 0.02Im-ZIF-67(b), 0.05Im-ZIF-67 (c) and (d) 0.1Im-ZIF-67 under 1200nm excitation; The comparison of TA spectra at 1 ps (e) and 5 ns (f).

**Figure 6-5.** kinetic traces of ZIF-67 based samples under 1200 nm excitation.

**Figure 6-6.** Photocatalysis hydrogen generation efficiency of ZIF-67 based samples under 20h illumination.

**Figure 6-7.** TA spectra of  $\text{Ru}(\text{bpy})_3^{2+}/\text{Al}_2\text{O}_3$  (a),  $\text{Ru}(\text{bpy})_3^{2+}/\text{ZIF-67}$  (b) and  $\text{Ru}(\text{bpy})_3^{2+}/0.05\text{Im-ZIF-67}$ (c) under 430 nm excitation. (d) Excited state decay traces of  $\text{Ru}(\text{bpy})_3^{2+}$  on different samples.

**Figure 6-8.** TA spectra of  $\text{Ru}(\text{bpy})_3^{2+}/0.02\text{Im-ZIF-67}$  (a) and  $\text{Ru}(\text{bpy})_3^{2+}/0.1\text{Im-ZIF-67}$  (b) under 430 nm excitation. (c) GSB recovery traces of  $\text{Ru}(\text{bpy})_3^{2+}$  on different samples.

**Figure 7-1.** TEM images of various cycles of  $\text{Al}_2\text{O}_3$  deposited on ZIF-67. (a) 20-cycle (b) 30-cycle (c) 40-cycle (d)100-cycle (e) cycles and thickness relationship of deposited  $\text{Al}_2\text{O}_3$ .

**Figure 7-2.** a) XRD patterns of glass,  $\text{Al}_2\text{O}_3/\text{glass}$ ,  $\text{ZIF-67}/\text{glass}$ ,  $\text{Al}_2\text{O}_3$  (8.5nm)/ZIF-67 and  $\text{RuN3}/\text{Al}_2\text{O}_3$  (8.5nm)/ZIF-67; XRD patterns of  $\text{Al}_2\text{O}_3$  on ZIF-67 films; (b), RuN3 sensitized films (c), ZIF-67 crystals synthesized from standard growth (denoted ZIF-67 standard) and ZIF-67 powder scratched from ZIF-67 film (denoted ZIF-67-F) (d).

**Figure 7-3.** UV-visible absorption spectra of  $\text{RuN3}/\text{ZIF-67}$ ,  $\text{Al}_2\text{O}_3(8.5\text{nm})/\text{ZIF-67}$ ,  $\text{RuN3}/\text{Al}_2\text{O}_3$  (8.5nm)/ZIF-67 and  $\text{RuN3}/\text{Al}_2\text{O}_3$  (a). UV-visible absorption spectra of  $\text{Al}_2\text{O}_3$  on ZIF-67 film (b) and RuN3 sensitized films (c) with different thickness of  $\text{Al}_2\text{O}_3$ .

**Figure 7-4.** Transient absorption spectra of  $\text{RuN3}/\text{ZIF-67}$  (a),  $\text{RuN3}/\text{Al}_2\text{O}_3(3\text{nm})/\text{ZIF-67}$  (c),  $\text{RuN3}/\text{Al}_2\text{O}_3(5\text{nm})/\text{ZIF-67}$  (d), and  $\text{RuN3}/\text{Al}_2\text{O}_3(8.5\text{nm})/\text{ZIF-67}$  (e); b) the comparison of GSB recovery and ESA decay kinetics of RuN3 on ZIF-67 and  $\text{Al}_2\text{O}_3$ ; f) The comparison of GSB recovery kinetics of RuN3 on different substrate.

**Figure 7-5.** Transient absorption spectra of  $\text{RuN3}/\text{Al}_2\text{O}_3$  (a) and  $\text{RuN3}/\text{Al}_2\text{O}_3(6.5\text{nm})/\text{ZIF-67}$  (b).

**Figure 7-6.** The ENT efficiency as a function of distance between ZIF-67 and RuN3.

**Figure 8-1.** XRD (a), UV-Visible diffuse reflectance (b) and emission spectra (c) of prepared ZIF-8 and RB-ZIF-8.

**Figure 8-2.** XRD (a) and UV-Visible diffuse reflectance (b) of different amount of Co doped RB-ZIF-8.

**Figure 8-3.** TA spectra of the obtained RB-ZIF-8 (a), 1 mg Co (b), 3 mg (c), 5 mg (d), 10 mg (e) and 20 mg Co (f) samples under 510 nm excitation.

**Figure 8-4.** Kinetic traces of RB/ZIF-8 (a), (b) 20 mg Co (b) and kinetics comparison between RB-ZIF-8 and 20 mg Co sample (c).

**Figure 8-5.** Kinetics comparison of RB-CoZIF-8 system: (a) excited state decay; (b) ground state bleach recovery.

**Figure 8-6.** (a) emission of RB in MeOH solution with different concentration; (b) emission intensity vs. RB concentration plot; (c) emission of three digested samples.

**Figure 8-7.** the plot of energy transfer vs. Co to RB ratio

## Chapter 1 Introduction

### **1.1 Why solar energy?**

The environment problems today such as greenhouse gas emission and air pollution caused by the combustion of fossil fuel and the increasing energy demand require people to develop renewable and environmentally friendly energy sources.<sup>1-4</sup> Among all the renewable energy sources, sunlight represents one of the most promising sources because it is free and abundant. However, the main challenge of using solar energy is how to effectively convert sun light to energy that humans can use and simultaneously solve the energy storage problem. One attractive strategy to solve such problems is solar to fuel conversion through water splitting process, where the energy is stored in the chemical bond of fuels.

### **1.2 The conversion of solar energy to fuels**

A solar fuel is a synthetic chemical fuel which is produced directly/indirectly from solar energy. The classical example for converting solar energy to chemical energy is natural photosynthesis<sup>5</sup> (Figure.1-1). This process provides most of the necessary energy for life on earth and also sustains oxygen levels. Typically, the first step in this process is the light harvesting on photosystem II (PS II) followed by charge separation. The photogenerated hole participates the water oxidation reaction to generate oxygen while the photogenerated electrons are transferred to the photosystem I (PS I) through the electron transport chain. In PS I, the photosensitizer such as P700 harvests light again to gain additional energy for this system, which can help the electrons to have sufficiently high redox potential to reduce

NADP<sup>+</sup> to NADPH which can help to reduce CO<sub>2</sub> to generate carbohydrate after a series of physical and chemical reactions.<sup>6-7</sup>

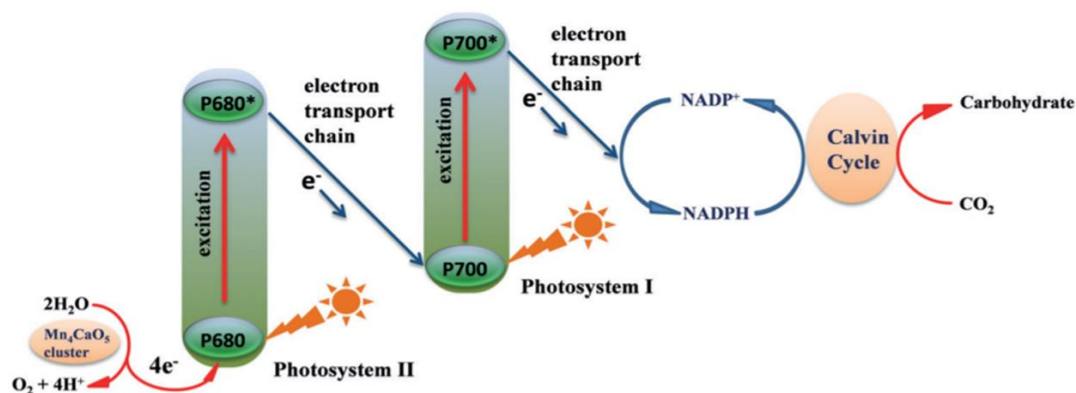


Figure 1-1 Schematic diagram of natural photosynthesis (ref.5)

To mimic this natural photosynthesis process, the researchers designed the artificial photosynthesis system<sup>8-10</sup> (Figure 1-2). The procedure in the artificial photosynthesis process is similar to the natural photosynthesis. The first step is the light absorption by photosensitizer on the photoanode to generate electron-hole pairs which play the same role as PS II in the natural photosynthesis process. The photoinduced hole participates H<sub>2</sub>O oxidation reaction and generate O<sub>2</sub>. After electron transport and additional input energy from photocathode (PS I), H<sup>+</sup> is reduced to H<sub>2</sub>. Since the first study on artificial photosynthesis performed by Fujishima and Honda in the 1970s,<sup>11</sup> great efforts have been devoted to studying how to utilize solar energy for water splitting.

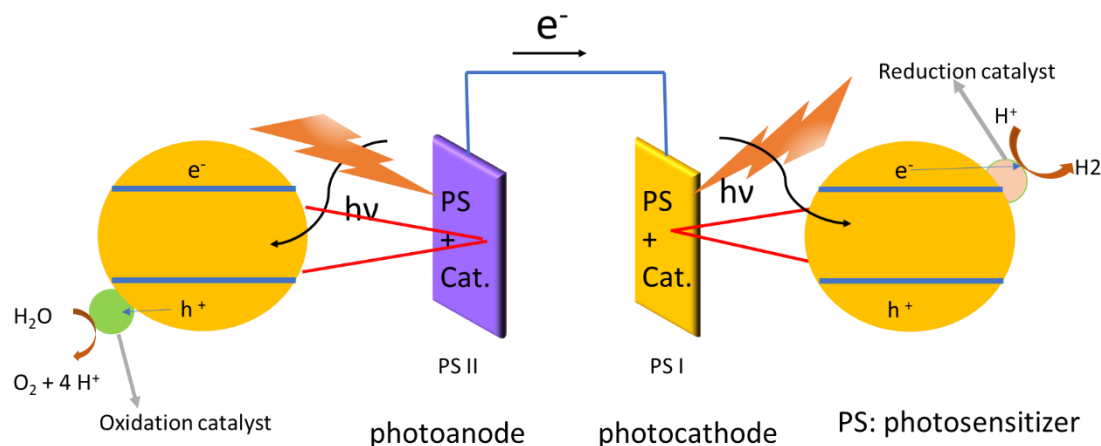


Figure 1-2 Schematic diagram of artificial photosynthesis

For solar energy to fuel conversion, the light harvesting materials play a very important role. Without light harvesting material, both conversions cannot be finished due to inability to capture sunlight. The light harvesting materials in green plants are some proteins and chlorophyll molecules.<sup>12-13</sup> Inspired by the green plants, scientists have found that some organic molecules (molecular dyes) and semiconductors can also capture light.<sup>14-16</sup>

### 1.3 Semiconductor quantum dots as light harvesting materials

In recent years, the colloidal quantum confined semiconductor nanocrystals or quantum dots (QDs) have attracted tremendous attention due to their low cost and strong and broad light absorption properties.<sup>17-18</sup> Compared to molecular chromophores, semiconductor QDs have many advantages as a photosensitizer, including adjustable bandgap, multiple exciton generation, rich surface binding sites and exceptional stability.<sup>19</sup>

Many QDs such as CdSe, CdS, PbSe, ZnSe and CuInS<sub>2</sub> have been widely studied as photosensitizer in photocatalysis to utilize solar energy. Eisenberg's work<sup>20</sup> proved that

with CdSe as the photosensitizer, the hydrogen generation overpotential through photoelectrochemical (PEC) method is much smaller than the catalyst without modified by CdSe. Reisner's work<sup>21</sup> reported that CdS can be used as the photosensitizer for CO<sub>2</sub> reduction (Figure 1-3). In this work, CdS QDs absorbed light and the photogenerated electron was transferred to the Ni-based catalyst then reduce CO<sub>2</sub> to CO. Triethanolamine (TEOA) worked as the electron donor to provide electrons which are used in the catalytic process. The Ni catalyst was anchored to CdS through different anchoring groups, it turned out that only with terpyC (terpyridine), this system had the highest CO selectivity, indicating that the performance of this system depended heavily on the interface between CdS and Ni catalyst.

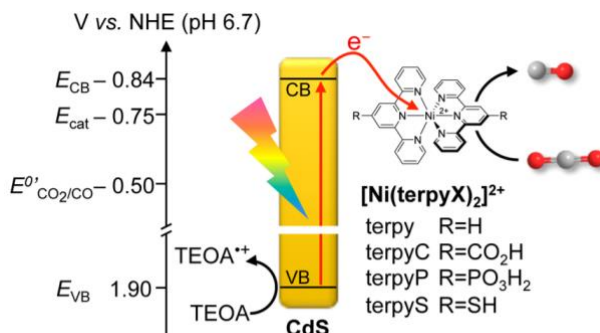


Figure 1-3 Schematic representation of the hybrid photocatalyst system. (ref.21)

Our group also have worked on CdSe as the photosensitizer and NiS as the co-catalyst for photocatalytic hydrogen generation.<sup>22</sup> In the presence of Ascorbic acid (AA), the turnover number can reach 511 with photon to H<sub>2</sub> efficiency 12.5%, which suggest the great promise to use this system for solar to fuel conversion. As shown in Figure 1-4, in

this system, the light was harvested by CdSe QDs followed by the photoinduced electron transfer to NiS co-catalyst to drive the reduction of proton to generate H<sub>2</sub>.

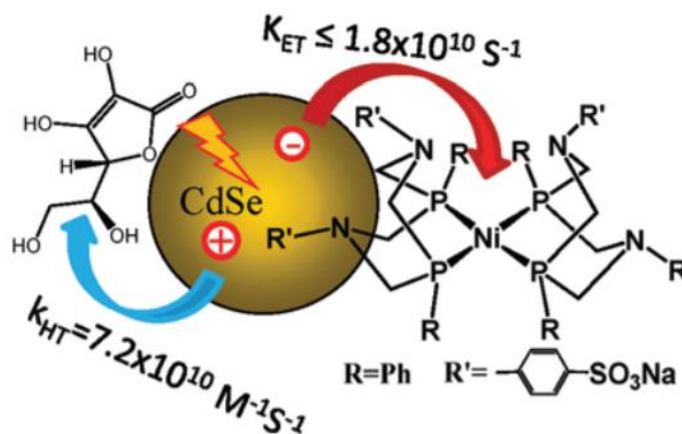


Figure 1-4 Cartoon of charge separation dynamics in CdSe QDs through electron transfer to NiS and hole transfer to AA. (ref. 22)

ZnSe QDs have been used as the photosensitizer for CO<sub>2</sub> reduction reaction. Reisner et al. reported that ZnSe can be modified by a Ni catalyst and used as the photosensitizer to increase the selectivity of CO.<sup>23</sup> As illustrated in Figure 1-5a, the electron transfer path from the QDs to H<sup>+</sup> is prevented by MEDA (2-Dimethylaminoethanethiol hydrochloride). As a result, the electron can transfer to the Ni catalyst to reduce CO<sub>2</sub> and generate CO. The limit of QDs as the light absorbing material is the lack of absorption at green and red region. It can only absorb light in the blue region (Figure 1-5b). To utilize solar energy more effectively, the photosensitizer with broader absorption in the visible region is desired.

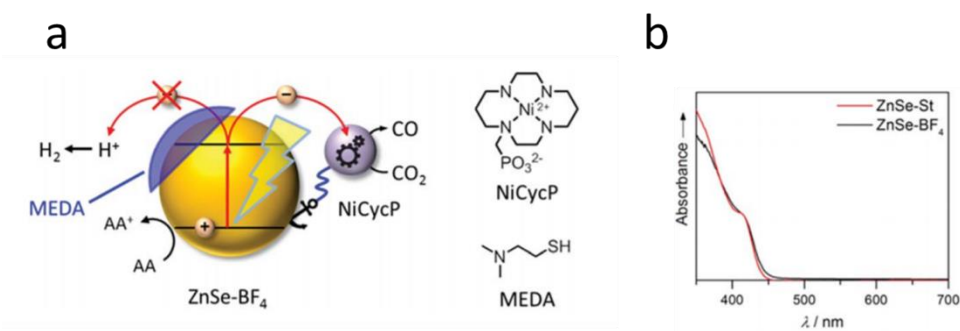


Figure 1-5 (a) Schematic representation of the photocatalyst system developed in this work; (b) UV-vis spectra of ZnSe quantum dots. (ref. 23)

Nowadays, we are pursuing green materials to protect environment. CdS, CdSe and PbSe QDs all have toxic heavy metal elements. As a result, it is not a perfect choice to use them as the photosensitizer in solar energy conversion for industrial application. Among different types of semiconductor QDs, ternary I-III-VI semiconductors have attracted intense attention because they have similar optical properties as Cd based QDs but toxic heavy metal are not involved.<sup>24-25</sup> Figure 1-6 displayed the optical band gaps for ternary I-III-VI semiconductors.<sup>26</sup> AgInSe<sub>2</sub>, CuGaSe<sub>2</sub>, CuInS<sub>2</sub>, AgGaSe<sub>2</sub> and CuInSe<sub>2</sub> have absorption in visible region while the absorption of CuGaS<sub>2</sub> and AgCaS<sub>2</sub> is near to UV region. To avoid the selenium toxicity, CuInS<sub>2</sub> is a better choice as the photosensitizer and it's absorption covers both yellow region and red region. The bulk bandgap of CuInS<sub>2</sub> is 1.45 eV and the bandgap can be tuned by the size of the nanoparticles or the change in composition.<sup>27</sup> CuInS<sub>2</sub> QDs have high extinction coefficient, emission quantum yield and

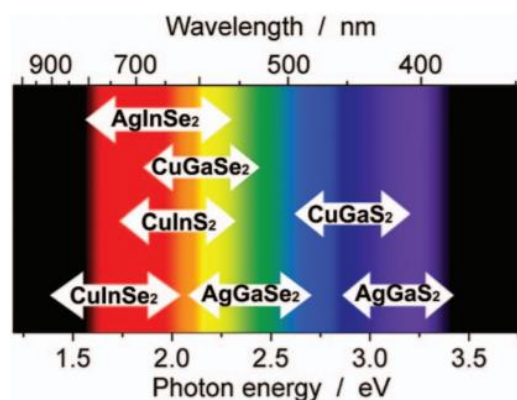


Figure 1-6 Optical band gaps for ternary I-III-VI semiconductors with particle size varies from 2 nm to 5 nm. (ref. 26 )

appropriate band gaps, which have rendered these semiconductor QDs desirable as light-harvesting and charge separation materials in photovoltaics, light emitting device and photocatalysis.<sup>28-29</sup>

### 1.3.1 Intrinsic optical properties of CuInS<sub>2</sub> quantum dots

Since the first report of CuInS<sub>2</sub> in 2003 by Castro,<sup>30</sup> CuInS<sub>2</sub> has attracted great attention as light harvesting materials for photocatalysis<sup>31-32</sup> and solar cells.<sup>33-34</sup> Similar to other semiconductor QDs, the optical properties of CuInS<sub>2</sub> QDs including bandgap, photoluminescence and photoinduced charge separation<sup>25, 35-36</sup> can be affected by many factors such as the size of the nanoparticles, the composition of CuInS<sub>2</sub> and the surface defects. As illustrated in Figure 1-7,<sup>35</sup> the bandgap of CuInS<sub>2</sub> semiconductor changes when the size or the composition changes. With larger nanoparticle size, the bandgap of CuInS<sub>2</sub> become smaller due to the quantum confined effect. For composition tuning, dopants such as Zn can be doped into CuInS<sub>2</sub> QDs structure. When Zn is doped into CuInS<sub>2</sub> structure,

the bandgap becomes larger, which is due to that the bandgap of ZnS is larger than that of CuInS<sub>2</sub>. For surface tuning, for example, CuInS<sub>2</sub> QDs coated with ZnS shell become heterostructure with type I band alignment.

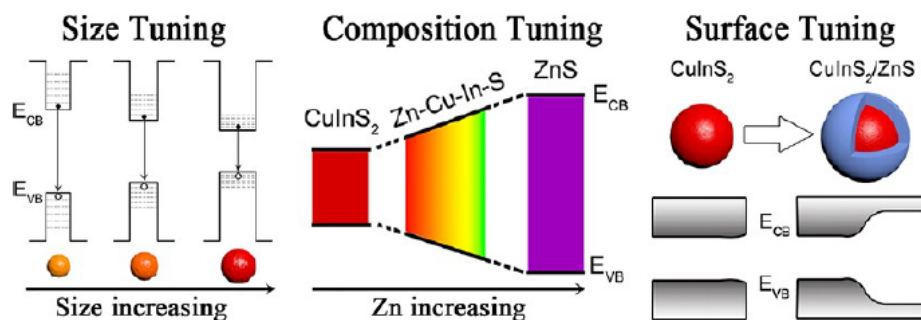


Figure 1-7 Illustration diagrams of the three main tuning methods. (ref.35)

The optical properties which depend on the size of the nanoparticles have been extensively investigated. To synthesize the QDs with different size, the synthesis condition is very important. Peng's group tuned the size of CuInS<sub>2</sub> nanoparticles by using Cationic precursors with different reactivity.<sup>25</sup> As shown in Figure 1-8a, the absorbance of CuInS<sub>2</sub> shifts to red part with larger particle size, indicating the smaller bandgap. Another strategy to tune the size is controlling the nucleation time of CuInS<sub>2</sub> during the growth process. Klimov's group studied the effect of nucleation time of CuInS<sub>2</sub>.<sup>37</sup> In their work, the reagents were the same and the only difference is the growth time at the 230 °C. Figure 1-8b displays the emission spectra of CuInS<sub>2</sub> with different growth time in Klimov's work. It clearly shows that with longer growth time the emission peak shifts from 630 nm to 780 nm, with is due to the increasing of the particle size (confirmed by the transmission electron microscopy (TEM)). In this work, it also confirms that the ratio between Cu and In of

CuInS<sub>2</sub> with different growth time is close to 1, suggesting that the emission peak shift is not due to the changes of the composition.

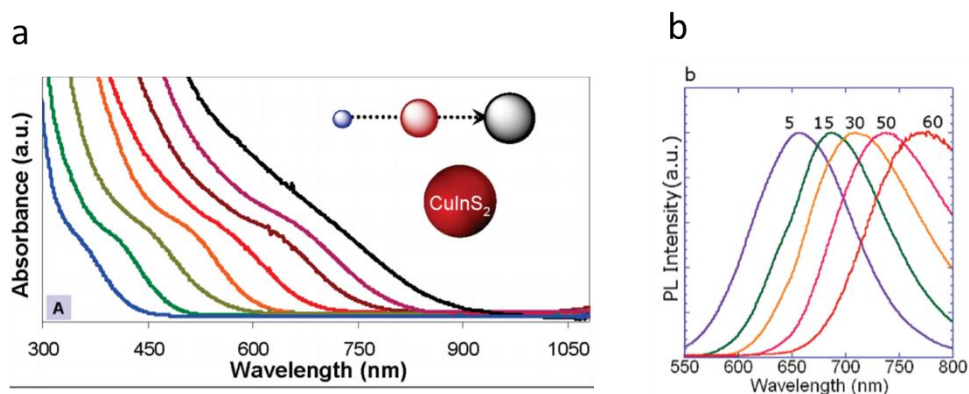


Figure 1-8 UV-vis absorption (a) and emission spectra (ref.25) (b) of CuInS<sub>2</sub> with different particle size (ref.37).

The composition of the multi-ternary semiconductor CuInS<sub>2</sub> can largely affect the optical properties and the composition tuning is much more complicated than QDs that have two elements such as CdSe. However, it also suggests that we have more choices in varying the composition. As mentioned at the beginning of this section, the doping of Zn can change the bandgap of the as-prepared CuInZnS QDs; In addition, CuInS<sub>2</sub> QDs with different Cu to In ratio show different bandgap because the bandgap of Cu<sub>2</sub>S is different from the bandgap of In<sub>2</sub>S<sub>3</sub>. Zunger's theoretical model on defects of CuInSe<sub>2</sub> supports that I-III-VI semiconductors have large structural tolerance to the off-stoichiometry,<sup>38</sup> resulting in copper-rich or copper deficient CuInS<sub>2</sub> QDs without changing the structure of CuInS<sub>2</sub>. Zhong's work studied the off-stoichiometry effect on CuInS<sub>2</sub> optical properties.<sup>39</sup> As illustrated in Figure 1-9 a, the In-rich CuInS<sub>2</sub> QDs are much more emissive than the Cu-rich CuInS<sub>2</sub> QDs and that the quantum yield increases with the decrease of Cu

concentration and reach the maximum at Cu to In ratio equals to 0.7 (Figure 1-9b). The emission peak of the as-prepared CuInS<sub>2</sub> shifts to blue with the increasing concentration of In. Kamat's group<sup>36</sup> proved that changing the composition of CuInS<sub>2</sub> doesn't change the QDs size, which can exclude the size effect when we work on the optical properties of CuInS<sub>2</sub>.

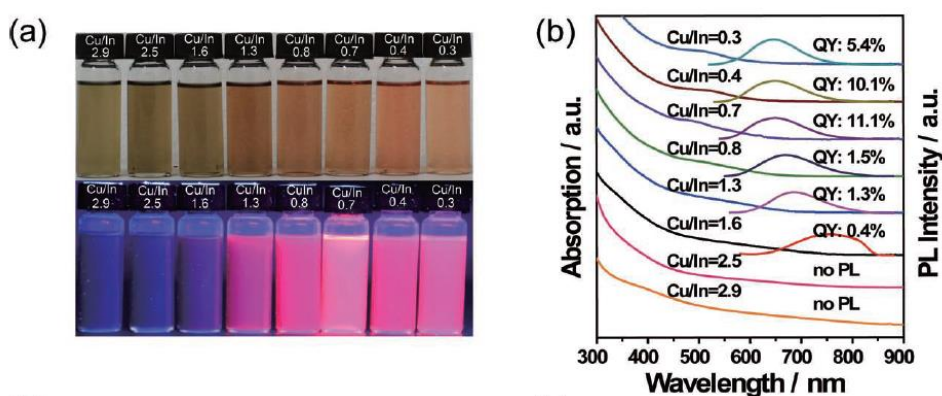


Figure 1-9 (a) Photograph of the resulting CuInS<sub>2</sub> samples with different [Cu]/[In] molar ratio in toluene and corresponding picture under a UV lamp. (b) Absorption and emission spectra of as-prepared CuInS<sub>2</sub> NCs with different [Cu]/[In] molar ratios. (ref.39)

Previous studies<sup>40</sup> show that the emission of CuInS<sub>2</sub> is dominated by the recombination process which is related to the donor-acceptor pair defects and surface defects, suggesting that changing the surface defect states can also facilitate tuning the photoluminescence properties. Klimov and coworkers<sup>37</sup> have investigated both ZnS shell and CdS shell on CuInS<sub>2</sub>. After coating with ZnS shell, the emission peak of the as-prepared sample has blue shift due to the etching of the core material under shell growth conditions. The coating of CdS caused the slightly blue shift, which is followed by red shift and is consistent with slight delocalization of the electron into the CdS layer due to the significantly lower-lying

conduction band. The result also shows that the quantum yield increases with the coating of ZnS or CdS shell, which can be attributed to the suppression of a fast, primarily non-radiative recombination process associated with surface-related defects.

### **1.3.2 Photocatalytic hydrogen generation by CuInS<sub>2</sub>**

Solar H<sub>2</sub> generation through photocatalytic water splitting, an attractive strategy to partially resolve the energy crisis, requires an efficient photocatalytic system that is not only capable of efficient light harvesting but also that can perform the subsequent catalytic reaction.<sup>1,41</sup> Since the initial report of light-driven H<sub>2</sub> generation,<sup>11,42</sup> extensive efforts have been made to develop semiconductor nanocrystals as photocatalytic materials.<sup>43-46</sup> Among the various kinds of semiconductor nanocrystals reported, most of them are either wide band gap semiconductors,<sup>47-48</sup> which only respond to UV light, or contain highly toxic element, such as Cd and Pb, largely limiting their practical application.<sup>49</sup> As a result, there is significant interest in developing multinary semiconductor nanocrystals to replace these highly toxic materials for photocatalytic applications. Among the semiconductor nanocrystals, CuInS<sub>2</sub> draws intensive attention because of non-toxicity element included in CuInS<sub>2</sub>. CuInS<sub>2</sub> has been used for hydrogen generation in both photoelectrochemical (PEC) and photocatalytic devices.<sup>32, 50</sup> Marsan's group<sup>51</sup> investigated the potential of CuInS<sub>2</sub>/silicon nanowires (SiNWs) on silicon substrate for photoelectrochemical hydrogen generation (Figure 1-11). The heterostructure semiconductor was used the anode and platinum as the cathode. The heterosemiconductor can absorb light and the photogenerated electrons were transferred to the cathode to reduce H<sup>+</sup> and generate hydrogen. In this work, it points out that the resistance of SiNWs is much higher than that of CuInS<sub>2</sub>/SiNWs, indicating better photoelectrochemical hydrogen generation efficiency.

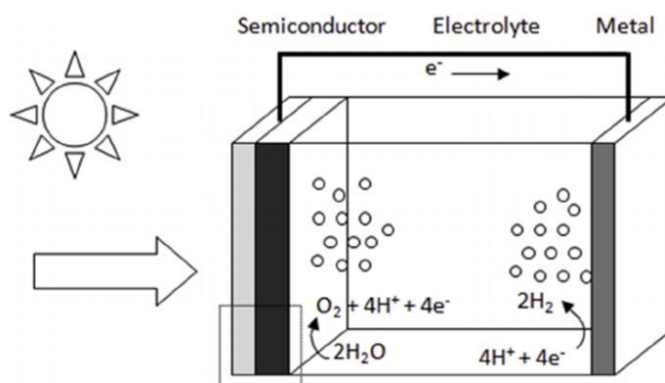


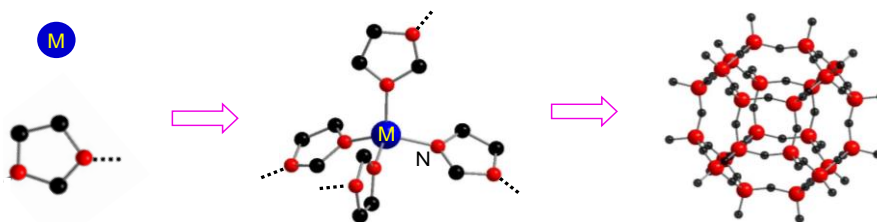
Figure 1-10 Illustration of photoelectrochemical water splitting. (ref.51)

#### 1.4 Zeolitic imidazolate frameworks as photocatalytic material

Zeolitic imidazolate frameworks (ZIFs) are a unique subclass of metal organic frameworks (MOFs) that are composed of transition metal ion nodes tetrahedrally coordinated by imidazolate linkers (Scheme 1-1).<sup>52-54</sup> Through the choice of metal nodes and functionalization of the imidazolate linkers, over 150 ZIF structures have, to date, been synthesized.<sup>53, 55-57</sup> Many of them are microporous with inherently large surface areas and tunable cavities, and additionally exhibit exceptional thermal and chemical stability.<sup>58-60</sup> These attributes make ZIF materials ideal for a variety of applications such as gas separation and storage,<sup>61-69</sup> chemical sensing,<sup>70</sup> and heterogeneous catalysis,<sup>71-77</sup> which have resulted into large number of publications in the past decades. In addition, owing to the large availability of building blocks, ZIFs with different structure and properties can be achieved by tuning the chemical compositions (metal nodes and linkers) to control the shape,<sup>58-60</sup> the size,<sup>61-65</sup> and the pore structure.<sup>62, 66-67</sup> These unique features have resulted into their additional applications in fields such as using ZIFs as host for white light

emitting,<sup>68-70</sup> catalysis<sup>71-72</sup> and sensing,<sup>73</sup> and using ZIFs as templates to synthesize nanoporous materials that can be used for electrocatalysis,<sup>74-77</sup> photocatalysis,<sup>78-80</sup> batteries,<sup>81-83</sup> and supercapacitor.<sup>84-86</sup> Moreover, many ZIFs are constructed from transition metals such as Co, Ni and Cu, which have rich redox chemistry and exhibit broad absorption in UV-visible spectrum in tetrahedral geometry. These features imply their great potential as intrinsic light harvesting and charge separation materials, which is in stark contrast to many other transition metal-based MOFs and Zr based UIO MOFs, where additional photosensitizers and/or cocatalysts are needed for photocatalytic applications.<sup>87-</sup>

92



Scheme 1-1 illustration of the formation of ZIFs

#### 1.4.1 Intrinsic light harvesting properties of zeolitic imidazolate frameworks

While ZIFs have attracted tremendous attention in photocatalysis in the past few years, they are mainly used as simple hosts or passive medium for dispersing other catalytic active species or reaction substrates,<sup>78, 80, 93</sup> largely resembling the roles of zeolites in catalysis.<sup>94</sup> In contrast, our recent study on ZIF-67 constructed from Co metal nodes tetrahedrally coordinated by 2-methyl imidazolate (inset of Figure 1-11a) shows that ZIF-67 has broad absorption in UV-visible and Near IR absorption region (Figure 1-11a),<sup>95</sup> including a strong ligand-to-metal charge transfer (LMCT) band at < 350 nm, a higher-lying [<sup>4</sup>A<sub>2</sub>(F)-

${}^4T_1(P)$ ] and lower-lying [ ${}^4A_2(F)$ - ${}^4T_1(F)$ ] d-d ligand field transitions in visible and near IR region, respectively, which result from  $Co^{2+}$  ion in  $T_d$  environment.<sup>96-97</sup> The excited state dynamics examined by transient absorption (TA) spectroscopy shows that the photoexcitation of either transition results into the formation of a long-lived intermediate state with 2.9  $\mu s$  lifetime (Figure 1-11b and 1-11c). Using X-ray transient absorption (XTA) spectroscopy, we found that the photoexcitation of ZIF-67 results into the reduction at Co center (Figure 1-11d), suggesting that this long-lived intermediate state is an excited charge separated (ECS) state with electrons located in Co center while holes in imidazolate ligands. These results suggest the potential of using ZIF-67 as light harvesting and charge separation materials rather than inert host for photocatalytic applications.

The question that naturally follows our spectroscopic studies on the formation of long-lived ECS state in ZIF-67 film is whether this state is localized in the single unit or delocalized in the ZIF-67 framework. Unravelling the nature of carrier localization/delocalization is essential for their application in photocatalysis. We hypothesize that, if the photo-generated carriers are delocalized in the framework, the lifetime of the ECS state is expected to increase with increasing dimension of the framework due to long-distance charge separation. In contrast, if the ECS state is localized in the single strut of the framework, varying the dimension of ZIF framework is less likely to impact the ECS lifetime. The rationale of this hypothesis is based on previous findings on inorganic<sup>98-103</sup> and organic semiconductors,<sup>104-106</sup> where enhanced spatial separation of

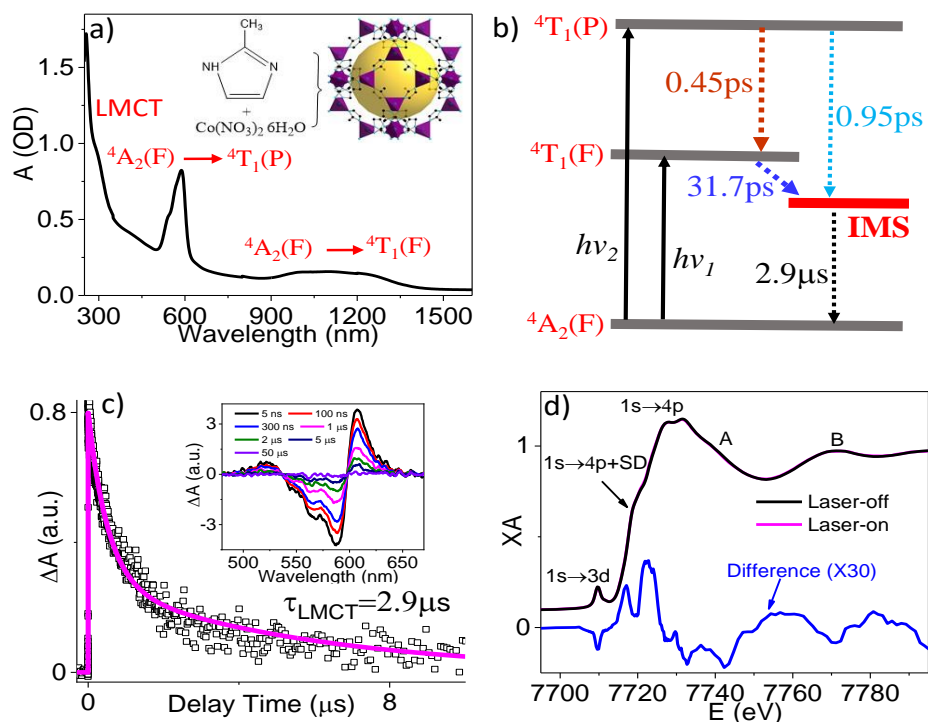


Figure 1-11. (a) UV-Vis-Near IR absorption spectrum of ZIF-67 thin film. The inset shows the synthetic scheme for the formation of ZIF-67 crystal; (b) The schematic representation of energy diagram of  $\text{Co}^{2+}$  ( $T_d$ ) and excited state relaxation of ZIF-67; (c) The kinetic trace of ZIF-67 TA spectra (inset) at 610 nm; (d) XANES spectrum of ZIF-67 at Co K edge before (laser-off) and 500 ps after (laser-on) laser excitation. The difference spectrum is obtained by subtracting the laser-off spectrum from laser-on spectrum.

(Ref.95)

photogenerated electrons and holes can inhibit carrier recombination and hence elongated lifetime. Guided by this idea, we have investigated the effect of dimension on ECS dynamics by comparing the TA spectra of ZIF-67 with a model coordination complex which only includes a single unit of  $\text{Co}[\text{im}^*]_2$  ( $\text{im}^* = 1,3\text{-dimethylimidazolite}$ , inset of Figure 1-12a). Because the nitrogen atom at 'position 3' in  $\text{Im}^*$  is capped by the  $-\text{CH}_3$  group, continued growth of the complex to form ZIF framework is prevented. The  $T_d$  geometry of this complex was confirmed by UV-visible-near IR absorption spectroscopy (Figure 1-12a), which is featured by LMCT and two d-d transitions that are characteristic

of tetrahedral  $\text{Co}^{2+}$  center and resembles that of ZIF-67. The X-ray absorption near edge structure (XANES) spectrum of  $\text{Co}[\text{im}^*]_2$  shows the prominent dipole forbidden 1s-3d pre-edge feature and flat 1s-4p transition (Figure 1-12b), which is distinct from that of  $\text{Co}(\text{NO}_3)_2$  with  $\text{O}_h$  Co center and analogous to ZIF-67 with  $\text{T}_d$  geometry. Quantitative analysis of the extended X-ray absorption fine structure (EXAFS) spectrum of  $\text{Co}[\text{im}^*]_2$  reveals that each Co center is coordinated by 4 nitrogen neighbors with Co-N distance 1.99 Å (inset of Figure 1-12b). These results together confirm the  $\text{T}_d$  geometry of Co atom in  $\text{Co}[\text{im}^*]_2$ . Figure 1-12c shows the TA spectra of this single unit model complex following 1000 nm excitation. Unlike ZIF-67, the TA spectra of this model complex are featured only by its ground state bleach centered at ~580 nm and excited state absorption > 654 nm, without any additional features associated with ECS state. Furthermore, the excited state lifetime of this complex (3.7 ps, Figure 1-12d) is orders of magnitude shorter than that of ZIF-67 (~2.9 μs). These results together indicate that ECS state is not formed in this model complex, which also suggests that the porous framework in ZIF-67 plays a central role in the formation of long-lived ECS state and the long-lived ECS state is likely delocalized in the ZIF-67 framework. Additional support of the delocalization nature of ECS arises from a recent report by Li et al.,<sup>107</sup> which demonstrated that the transition for the higher lying d-d transition shows 14 nm blue shift when the particle size of ZIF-67 decreases from 1208 nm to 180 nm, suggesting that excited state energy is dependent on the dimension of ZIF-67.

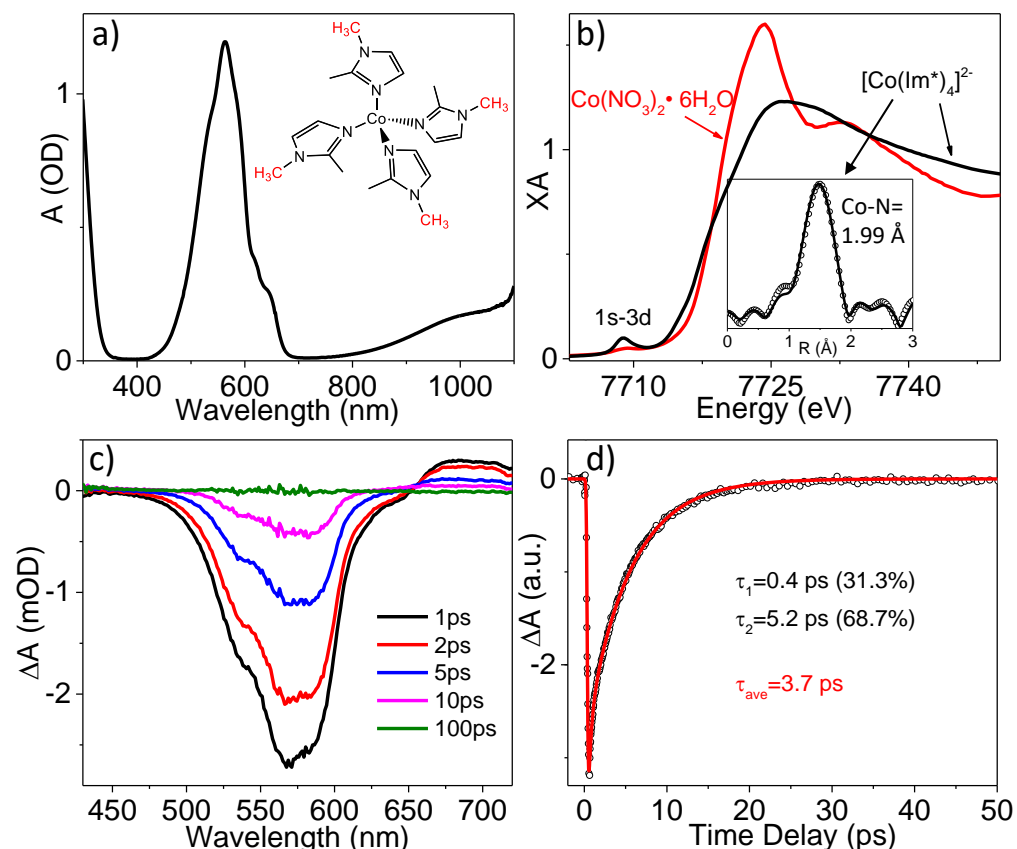


Figure 1-12. (a) UV-visible-near IR absorption spectrum of  $\text{Co}[\text{im}^*]_2$ . The inset shows the molecular structure of  $\text{Co}[\text{im}^*]_2$ ; (b) XANES spectrum of  $\text{Co}[\text{im}^*]_2$  and  $\text{Co}(\text{NO}_3)_2 \cdot 6\text{H}_2\text{O}$  at Co K edge. The inset shows the EXAFS spectrum in R-space and its fitting; (c) TA spectra of  $\text{Co}[\text{im}^*]_2$  following 1000 nm excitation; (d) The kinetic trace at 580 nm representing ground state bleach recovery.

A key question that emerged following the discovery of the delocalization nature of ECS state in ZIF-67 is how the charge carriers transport across the framework. Inspired from the previous studies, where ZIFs based on  $\text{Co}^{2+}$  ( $3d^7$ ) node show higher conductivity than those based on closed shell  $\text{Zn}^{2+}$  ( $3d^{10}$ ) node,<sup>108</sup> and the d orbitals of the metal nodes in ZIFs are predicted to participate the formation of a continuous band,<sup>109-112</sup> we hypothesized that charge transport in ZIFs may proceed through metal nodes. If this is true, the introduction of a guest metal into the parent ZIF is anticipated to perturb charge

transport mechanism and thus impacts the ECS dynamics. To test this hypothesis, we recently designed the mixed-metal isostructural ZIFs by introducing a guest metal ( $\text{Zn}^{2+}$  or  $\text{Cu}^{2+}$ ) to the ZIF-67 parent framework (Figure 1-13a).<sup>113</sup> Using TA spectroscopy, we found that the incorporation of a statistical number of redox-inert metal node ( $\text{Zn}^{2+}$ ) into ZIF-67 partially blocks the inherent ECS through Co-Co communication, resulting into the slower formation of ECS state and faster ground state recovery through  $^4\text{T}_1$  to  $^4\text{A}_2$  pathway (Figure 1-13b). These results suggest that metal-metal charge transfer (MMCT) is likely responsible for the observed long-lived ECS state. To further test MMCT mechanism, we next designed a second mixed-metal system by incorporating some open-shell  $\text{Cu}^{2+}$  ions into ZIF-67. TA results show that the presence of redox active  $\text{Cu}^{2+}$  ions has negligible impact on the formation of ECS state (Figure 1-13c) and ground state recovery (inset of Figure 1-13c). More interestingly, using the element specific XTA spectroscopy, we found that the selective excitation of  $\text{Co}^{2+}$  center results into the reduction at  $\text{Cu}^{2+}$  center (Figure 1-13d), i. e. electrons migrate from  $\text{Co}^{2+}$  to  $\text{Cu}^{2+}$  following photoexcitation of  $\text{Co}^{2+}$ , which unambiguously confirms the MMCT pathway and the delocalized nature of the long-lived ECS state. Furthermore, node-to-node communication was also observed in the ground state of ZIFs investigated by SQUID magnetometry,<sup>113</sup> where the paramagnetic susceptibility data for ZIF-67 and Cu doped ZIF-67 samples all exhibit a transition to an antiferromagnetically ordered state at temperatures lower than  $\sim 21$  K ( $T_N$ ), whereas the introduction of  $\text{Zn}^{2+}$  shuts down the magnetic exchange interactions responsible for the ordering behavior.<sup>114</sup>

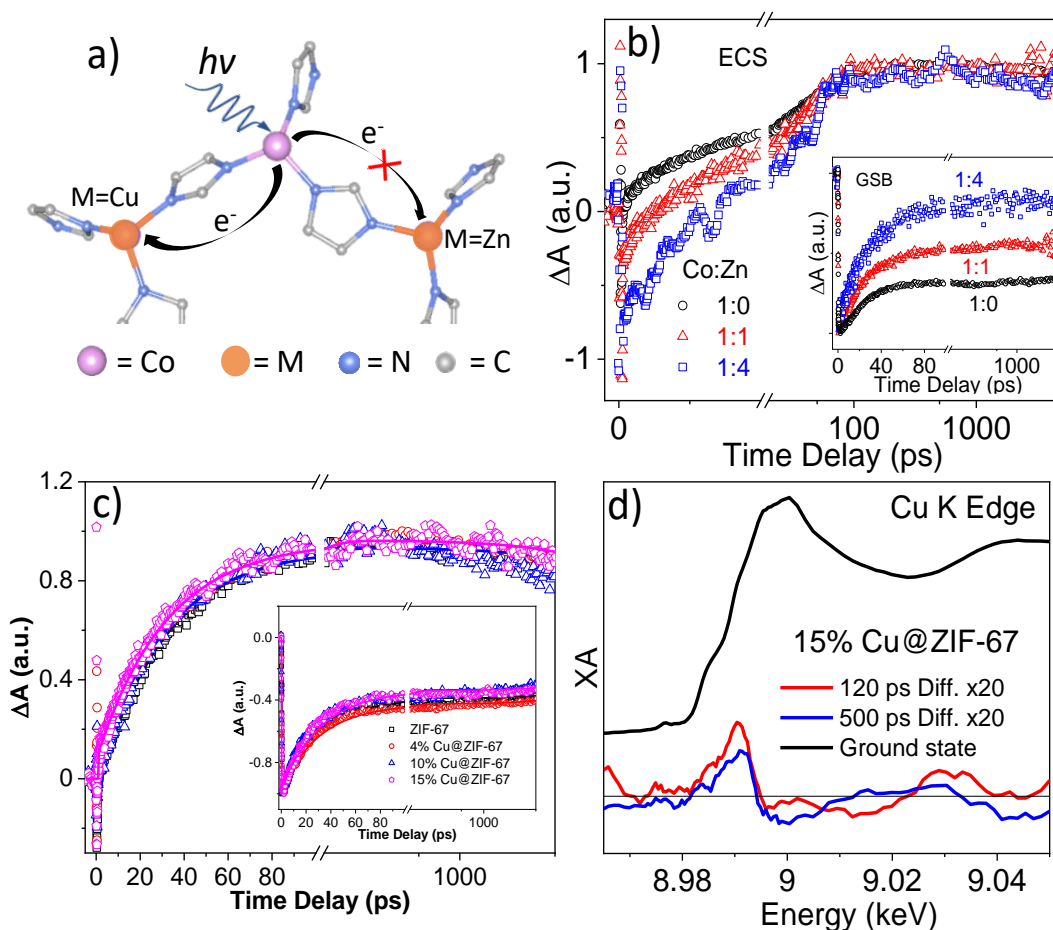


Figure 1-13. (a) The schematic representation of ECS formation pathway in Zn or Cu doped ZIF-67; (b) The kinetic traces of the ECS state at 610 nm and the ground state bleach (GSB, inset) at 585 nm for ZIF-67 with variable Co:Zn ratios; (c) ECS and GSB traces for Cu@ZIF-67 with variable % Cu (c); (d) Representative Cu K-edge XANES spectrum (black line) and XTA difference spectra at the Cu K-edge for Cu@ZIF-67 after 590 nm excitation at 120 and 500 ps time delays. Ref. [113]

#### 1.4.2 Photocatalytic properties of zeolitic imidazolate frameworks

While the discovery of the long-lived ECS and the capability to enhance light harvesting ability of ZIFs through ENT process imply the potential applications of ZIFs as light absorption materials for photocatalysis, the fast and efficient charge transfer from photosensitizer (PS) to photocatalyst is essential to make the subsequent photocatalytic

processes possible. Both molecular and semiconductor chromophores have been encapsulated/adsorbed into ZIF frameworks/surface and used as photosensitizers for ZIF based photocatalytic systems. One renowned example of molecular photosensitizers in ZIF based photocatalytic system is  $\text{Ru}(\text{bpy})_3\text{Cl}_2$  (bpy= 2,2'-bipyridyl). For example, the group of Wang have reported two photocatalytic systems based on  $\text{Ru}(\text{bpy})_3\text{Cl}_2$  as photosensitizer and ZIF-9<sup>115</sup> (Co coordinated to benzimidazolate) and ZIF-67<sup>116</sup> as cocatalyst, respectively. Both systems demonstrated catalytic activity for light driven  $\text{CO}_2$  reduction to form CO, with a catalytic turn over number (TON) of about 450 in 2.5 hours for ZIF-9 system and 112 in 30 mins for ZIF-67. While direct experimental evidence of charge separation was not provided, a systematic study on photocatalytic activity for  $\text{CO}_2$  reduction to CO suggests that charge separation occurs through ET from the excited  $\text{Ru}(\text{bpy})_3\text{Cl}_2$  to ZIFs.<sup>115-116</sup> The direct observation of the charge separated state in  $\text{Ru}(\text{bpy})_3\text{Cl}_2/\text{ZIF-67}$  was reported in 2018 by our group.<sup>117</sup> Using TA spectroscopy, we found that selectively exciting  $\text{Ru}(\text{bpy})_3\text{Cl}_2$  leads to the faster decay of  $\text{Ru}(\text{bpy})_3\text{Cl}_2$  excited state absorption and slower recovery of ground state bleach (Figure 1-14a-c). This is accompanied by the formation of the ground state bleach of ZIF-67 (Figure 1-14a), suggesting that charge separation occurs between  $\text{Ru}(\text{bpy})_3\text{Cl}_2$  to ZIF-67. Moreover, XTA, an element specific technique that can selectively probe the electron density change at Co center in ZIF-67, shows the reduction of Co center in ZIF-67 following the excitation of  $\text{Ru}(\text{bpy})_3\text{Cl}_2$ , which unambiguously confirms that ET from  $\text{Ru}(\text{bpy})_3\text{Cl}_2$  to ZIF-67 is the charge separation pathway (inset of Figure 1-14c). This system can efficiently generate  $\text{H}_2$  (40,500  $\mu\text{mol/g}$  ZIF-67) steadily for at least 24 hours in the presence of TEOA as sacrificial electron donor (Figure 1-14d), which can be attributed to the efficient charge separation process due to much faster ET

(2.7 ns) than charge recombination ( $> 1 \mu\text{s}$ ). Additional observation of the formation of charge separation process was reported in  $\text{Ru}(\text{bpy})_3\text{Cl}_2$  decorated 2D ZIF-67 with leaf like morphology by Sun and co-workers.<sup>118</sup> Using TA spectroscopy, they observed the faster quenching of  $\text{Ru}(\text{bpy})_3\text{Cl}_2$  excited state and the formation of the reduced ZIF-67, which leads to the reduction of  $\text{CO}_2$  to form  $\text{CO}$ .

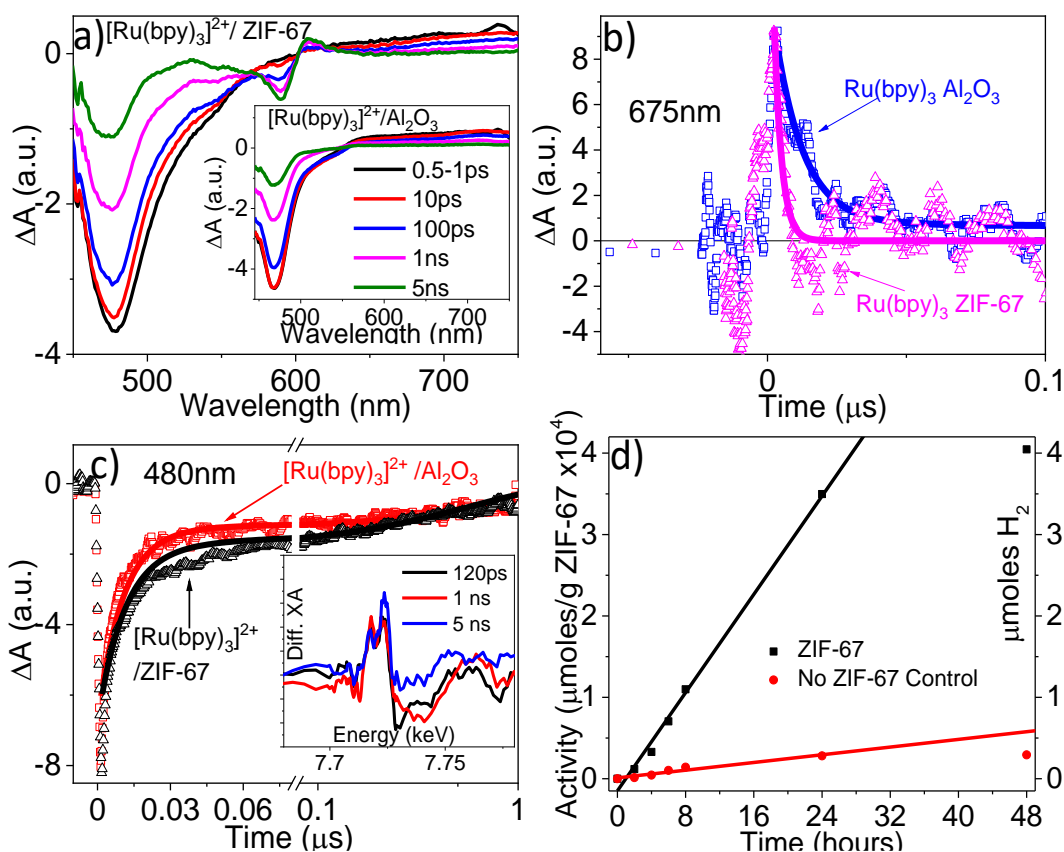


Figure 1-14. (a) TA spectra of  $[\text{Ru}(\text{bpy})_3]^{2+}$  on ZIF-67 and  $\text{Al}_2\text{O}_3$  control (inset) following 410 nm excitation; (b) The comparison of TA kinetics of  $[\text{Ru}(\text{bpy})_3]^{2+}$  excited state decay (b) and ground state bleach (c) between  $\text{Al}_2\text{O}_3$  and ZIF-67; The inset of (c) is the XTA spectra of ZIF-67 at Co k-edge upon the excitation of  $[\text{Ru}(\text{bpy})_3]^{2+}$  at 400nm. (d) The full-time profile of  $\text{H}_2$  evolution under the optimized catalytic conditions. Ref. (117)

In addition to molecular chromophores, semiconductors can also be encapsulated into ZIFs to initiate charge separation process. As early as 2014, Wang and coworkers have reported ET from CdS to ZIF-9 (Figure 1-15a).<sup>119</sup> The trend of the reduction of CO<sub>2</sub> to form CO/H<sub>2</sub> matches well with the optical absorption spectrum of CdS rather than ZIF-9 (Figure 1-15b), and that in situ photoluminescence spectroscopic study demonstrates the inhibited electron hole recombination due to the presence of ZIF-9 (Figure 1-15c). These results together suggest that charge separation occurs between CdS and ZIF-9, where the former acts as a photosensitizer and the latter serves as a cocatalyst. Halide perovskite is another class of semiconductor material that have been incorporated to ZIFs as photosensitizers.<sup>120-122</sup> For example, Su et al. synthesized CsPbBr<sub>3</sub>@ZIF hybrid with CsPbBr<sub>3</sub> QD coated on the surface of ZIF-67 through in situ growth approach, where the pre-synthesized CsPbBr<sub>3</sub> was added to the ZIF precursor solution (Figure 1-15d).<sup>120</sup> Using both time resolved photoluminescence spectroscopy (Figure 1-15e) and TA spectroscopy, charge separation in CsPbBr<sub>3</sub>@ZIF hybrid was found to occur through ET from CsPbBr<sub>3</sub> to ZIF-67, which eventually leads to the reduction of CO<sub>2</sub> to form CH<sub>4</sub> and CO.

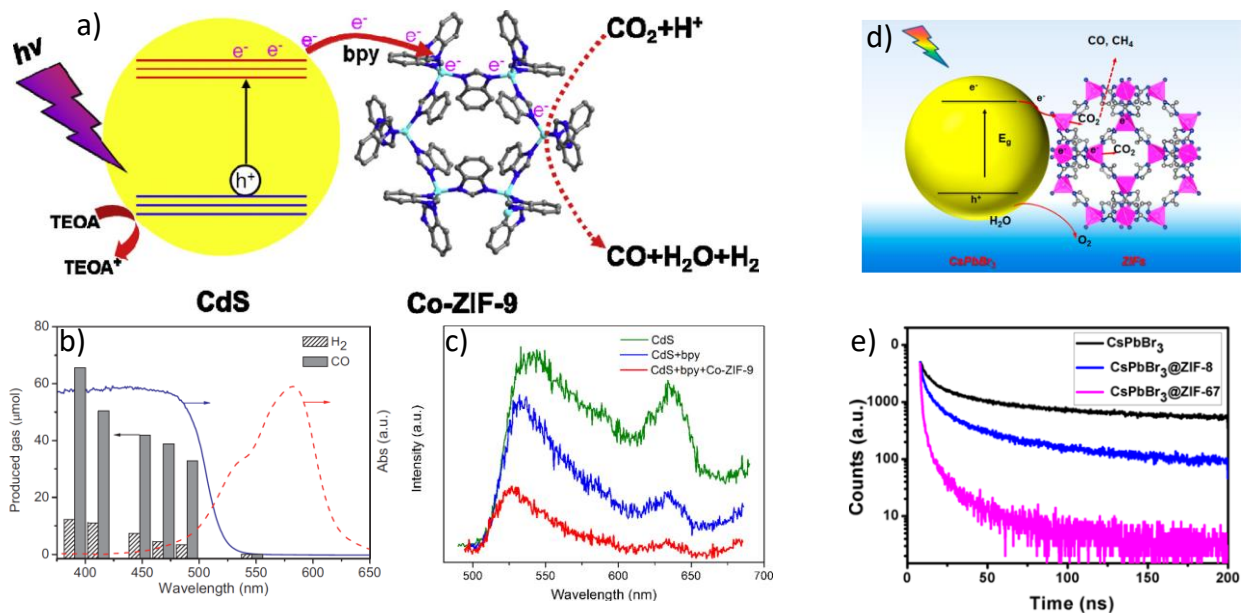


Figure 1-15. (a) Possible reaction mechanism for the Co-ZIF-9 cocatalyzed photoreduction of CO<sub>2</sub> employing CdS as the light harvester; (b) the dependence of the wavelength of incident light on the evolution of CO and H<sub>2</sub> from the Co-ZIF-9 promoted CO<sub>2</sub> photoreduction system. The histogram represents the production of CO and H<sub>2</sub>. The lines are the UV-Vis diffuse reflectance spectrum of CdS (solid) and Co-ZIF-9 (dash); (c) PL spectra of the reaction systems under 400 nm laser irradiation at room temperature. Ref (119) (d) Schematic illustration of CO<sub>2</sub> photoreduction process of CsPbBr<sub>3</sub>/ZIFs; (e) time-resolved PL decay plots of CsPbBr<sub>3</sub> and CsPbBr<sub>3</sub>/ZIFs. Ref. (120)

## Chapter 2 Experiment and Characterization

In this chapter, the details of the synthesis and characterization of the samples used in this work will be summarized. The samples in my PhD works include CuInS<sub>2</sub> (CIS) QDs, ZIFs with different ligands, dye encapsulation into ZIFs. Besides the standard characterization such as UV-vis absorption spectra, X-ray diffraction (XRD) and scanning electron microscope (SEM), the pump and probe transient absorption spectroscopy and time-resolved X-ray absorption spectroscopy were used to examine the photodynamics of the samples. The photocatalytic hydrogen generation was also performed and the experiment details will be discussed later.

### **2.1 Standard Characterization**

Steady-state UV–visible absorption spectra were taken using an HP Agilent 8453 spectrophotometer (UV-Visible) and a Cary 5000 spectrometer (UV-Visible-NIR). Steady-state emission spectra and time-correlated single photon counting (TCSPC) lifetime were measured using a Photon Technology International QuantaMaster 40 spectrofluorometer. Powder X-ray diffraction (XRD) data were collected by using Rigaku Miniflex II XRD diffractometer with Cu K $\alpha$  radiation. Transmission Electron Microscopy (TEM) was taken with a JEOL JEM-2100UHR electron microscope. Energy dispersive X-ray (EDX) data were collected on a Hitachi S-4800 scanning electron microscope with an EDAX XM2–60S energy dispersive spectrometer. Scanning Electron Microscope (SEM) were taken by JSM 6510-LV (JEOL Ltd, Tokyo).

### **Small-Angle X-ray Scattering (SAXS)**

The size and distribution of CuInS<sub>2</sub> (CIS) quantum dots were determined by SAXS which was measured at beamline 12ID-B at the Advanced Photon Source, Argonne National Laboratory. The wavelength,  $\lambda$ , of X-ray radiation was set as 0.886 Å. Scattered X-ray intensities were measured using a Pilatus 2 M detector. The sample-to-detector distance was set such that the detecting range of momentum transfer  $q$  ( $=4\pi \sin \theta/\lambda$ , where  $2\theta$  is the scattering angle) was 0.006–0.90 Å<sup>-1</sup>. A flow cell that is made of a cylindrical quartz capillary with a diameter of 1.5 mm and a wall of 10 μm was used for SAXS measurements. To obtain good signal-to-noise ratio, 20 scattering images were collected for each sample or solvent. The 2-D scattering images were converted to 1-D SAXS ( $I(q)$  vs  $q$ ) curves through azimuthally averaging after solid angle correction and then normalizing with the intensity of the transmitted X-ray beam flux, using a software package developed for the beamline. After subtraction of the solvent background, the SAXS profiles were fit using Irena package with the assumption of spherical particle shape and log-normal size distribution.

### **Steady-State X-ray Absorption Spectroscopy (XAS)**

XAS measurements were performed at the beamline 12BM at the Advanced Photon Source, Argonne National Laboratory. The XAS spectra were collected at room temperature by fluorescence mode using a 13-element germanium solid-state detector. One ion chamber is placed before the sample and used as the incident X-ray flux reference signal. There are two ion chambers (second and third chambers) after the sample. The metal foil is placed between the second and third ion chambers and used for energy calibration and collecting metal spectrum.

### **Time-Resolved Optical Absorption Spectroscopy (OTA)**

The femtosecond OTA setup is based on a regenerative amplified Ti-sapphire laser system (Solstice, 800 nm, <100 fs fwhm, 3.5 mJ/pulse, 1 kHz repetition rate). The tunable pump (235–1100 nm), chopped at 500 Hz, is generated in TOPAS (Light Conversion) from 75% of the split output from the Ti-sapphire laser. The tunable UV–visible probe pulses are generated from the other 25% of the Ti-sapphire output through white light generation in a sapphire (430–750 nm) window on a translation stage. The femtosecond OTA measurements were performed in a Helios ultrafast spectrometer (Ultrafast Systems LLC). The sample was placed in a cuvette with a path length of 2 mm, which was continuously stirred during measurements to avoid sample degradation. The probe light meets with the pump light at the sample cell with a delay  $\tau$  with respect to pump. The pump light was used to excite the sample to its excited state and the probe light (white light) can measure the absorbance of the sample with and without pump.

### **Time-Resolved X-ray Absorption Spectroscopy (XTA)**

XTA was performed at beamline 11ID-D, Advanced Photon Source (APS) at Argonne National Laboratory. The sample was excited with 400 nm, 100 fs laser pulse that was generated from the second harmonic of Ti:sapphire regenerative amplified laser operating at 10 kHz repetition rate. The experiment was carried out under the hybrid-timing mode where an intense X-ray pulse was used as the probe pulse. This intense pulse (117 ps, 271.5 kHz) contains 16% of the total average photon flux and was separated in time from other weak X-ray pulses. Two avalanche photodiodes (APD) were positioned at a 90° angle on both sides of the incident X-ray beam to collect the X-ray fluorescence signals. The sample solution was flowed through a stainless-steel tube and formed a free jet (600  $\mu\text{m}$  diameter) in the sample chamber. Custom-designed soller slit/Ni filter combination was placed at a

specific distance between the sample and the detectors. The X-ray fluorescence photons from the synchronized X-ray pulse at 110 ps after the laser pulse excitation were used to build the laser-on spectrum. The fluorescence signals averaged over 20 bunches before laser pulse were used to construct the ground state spectrum.

## **2.2. Experimental Details for Chapter 3**

### **Materials.**

Copper(I) iodide (CuI, 98%), indium(III) acetate ( $\text{In}(\text{OOCCH}_3)_3$ , 99.99% metals basis), 1-dodecanethiol (DDT, 98%), acetone (HPLC grade, 99.5+%), n-hexane (spectrophotometric grade, 95+%), and toluene (anhydrous, 99.8%) were purchased from Alfa Aesar (Tewksbury, MA).

### **Synthesis of $\text{CuInS}_2$ nanoparticles.**

Following the published procedure,<sup>37</sup> CuI (382 mg, 2 mmol),  $\text{In}(\text{OOCCH}_3)_3$  (580 mg, 2mmol), and DDT (10 mL) were mixed in a three-neck flask, degassed under vacuum for 5 min, and then purged with  $\text{N}_2$  for 10 min. The flask was heated to 120 °C for 10 min to dissolve the reagents and then to 200 °C for nucleation of the NPs. At the desired time point (15, 30, or 60 min), the flask was placed in a water bath to stop the growth of the NPs. The cooled samples were transferred to a centrifuge tube with ~20 mL of acetone and centrifuged to isolate the sample after decanting the supernatant. The CIS NPs were then redispersed in toluene for further experimentation.

## **2.3. Experimental Details for Chapter 4**

### **Chemicals and Materials.**

Copper(I) iodide (CuI, 98%), indium(III) acetate ( $\text{In}(\text{OOCCH}_3)_3$ , 99.99% metals basis), 1-dodecanethiol (DDT, 98%), and toluene (anhydrous, 99.8%) were purchased from Alfa

Aesar. 1-octadecene (ODE) and oleylamine (OLA) were purchased from Sigma-Aldrich. The rest chemicals and solvents were purchased from VWR. All chemicals were used as received without further purification.

### **Synthesis of CuInS<sub>2</sub>/ZnS (CIS/ZnS) quantum dots.**

In a typical synthesis for CuInS<sub>2</sub> with a Cu:In ratio of 1:2,<sup>123</sup> CuI (10 mg, 0.05 mmol), In(OAc)<sub>3</sub> (29.2 mg, 0.1 mmol), and 1-dodecanethiol (DDT) (5 ml) were mixed in a three-necked flask. The reaction mixture was degassed with N<sub>2</sub> for 30 min at room temperature. After that, the mixture was heated to 150 °C until a clear yellow solution was formed. Then, the mixture was heated to 230 °C and kept at this temperature for 5 min. For further growth of the ZnS shell, the Zn stock solution (4 ml) (see below for details) was added dropwise into the reaction mixture, after which the mixture was heated to 240 °C and kept at this temperature for 1 h. The zinc stock solution was prepared in advance by mixing Zn(OAc)<sub>2</sub> (0.219 mg, 1 mmol), oleylamine (OLA) (1 ml), and ODE (3 ml) in a flask, which is followed by degassing with N<sub>2</sub> for 30 min and heating to 100 °C until a colorless solution was formed. The resulting CIS/ZnS QDs were precipitated out using acetone, followed by centrifuging and decanting the supernatant. Half of the obtained samples were dispersed in toluene for optical property measurement, while the other half were used to prepare water soluble CIS/ZnS QDs. To synthesize CIS/ZnS QDs with different Cu to In ratios (i.e., 1:5, 1:8, and 1:10), the amount of CuI was kept the same while the amount of the In source was varied.

### **The synthesis of water soluble CIS/ZnS QDs.**

The water soluble CIS/ZnS QDs were prepared through ligand exchange procedure in the presence of mercaptopropionic acid (MPA).<sup>35</sup> In a typical synthesis, 2 ml of MPA, 3

ml of N, N-dimethylformamide (DMF), and 100 mg of CIS/ZnS QDs were added into a 25 ml flask, and degassed with N<sub>2</sub> for 30 min. The mixture was then heated to 130 °C and kept at this temperature for 30 min, which results in the formation of a clear solution. The CIS/ZnS was precipitated out by adding 40 ml of 2-propanol and centrifugated at 6000 rpm for 10 min. The obtained MPA capped CIS/ZnS QDs were dispersed in 15 ml H<sub>2</sub>O.

### **Photocatalytic Hydrogen Generation.**

All photocatalytic reactions were performed in a 11 ml vial under the illumination of a 405 nm light-emitting diode (LED) (3 mW). Typically, 0.1 ml of the CIS/ZnS QD solution was mixed with ascorbic acid (AA) (1.00 ml, 0.2M in H<sub>2</sub>O, pH = 5) and H<sub>2</sub>O (2.9 ml) in a sample vessel. The vial was sealed, degassed with nitrogen, and transferred to photocatalysis apparatus. The amount of evolved hydrogen (taken from 200 µl of the headspace of the vial) was quantified by using an Agilent 490 micro gas chromatograph (5 Å molecular sieve column).

## **2.4. Experimental Details for Chapter 5**

### **Chemicals and Materials.**

Cobalt (II) nitrate hexahydrate, Cobalt (II) acetate and benzimidazole (bIM) were purchased from Alfa Aesar. 2-Methylimidazole (2mIm 99%) was purchased from Acros Organics. 2-nitroimidazole (2nIm) was purchased from TCI chemicals. Methanol (MeOH), N,N-Dimethylmethanamide (DMF), sulfuric acid (H<sub>2</sub>SO<sub>4</sub>), Hydrogen Peroxide (H<sub>2</sub>O<sub>2</sub>, 30%) and Microscope slides were purchased from Fisher Scientific. Ethanol (EtOH 200 proof, anhydrous) was purchased from Decon Laboratories. All chemicals were used as received without further purification.

### **Growth of ZIF-67 and ZIF-67 film.**

The synthesis of ZIF-67 followed the protocols reported previously.<sup>124</sup> Typically, 0.73g  $\text{Co}(\text{NO}_3)_2 \cdot 6\text{H}_2\text{O}$  and 1.65 g 2-methylimidazole (2mIm) were dissolved in 50 mL MeOH respectively. 4 mL of metal solution was added into 4 mL of imidazole solution in 20 mL glass vial, which turns out purple color. Two pieces of etched glass slides were immersed into the purple solution and sit for 1 h. The obtained ZIF-67 films were rinsed with MeOH and dried with  $\text{N}_2$  flow. The powder sample was obtained by the centrifuge of the purple mixture and washed with MeOH.

#### **Growth of ZIF-9 and ZIF-9 film.**

The synthesis of ZIF-9 followed the modified method reported previously.<sup>125</sup> 2.08 g bIm was dissolved in 50 mL DMF while the Co precursor is the same as ZIF-67. 4 mL of metal solution was added into 4 mL of bIm solution in 20 mL glass vial and two glass slides were immersed into the mixed solution. Then the glass vial was placed in the oven under 50 °C for 3h. The obtained ZIF-9 films were rinsed with MeOH and dried with  $\text{N}_2$  flow. The powder ZIF-9 sample was obtained through centrifuge followed by washed with MeOH and dried under room temperature.

#### **Growth of ZIF-65 and ZIF-65 film.**

ZIF-65 was synthesized by a modified method according to the literature protocols.<sup>126</sup> 0.125 g  $\text{Co}(\text{CH}_3\text{COO})_2 \cdot 4\text{H}_2\text{O}$  was dissolved in 5 mL MeOH. 0.45 g 2nIm was dissolved in 5 mL DMSO. After mixing two solutions in a 20 mL glass vial, two pieces of glass slides were immersed into the mixed pink slurry and set it for 12h. ZIF-9 film was rinsed with MeOH and centrifuged to get the powder ZIF-9.

## **2.5. Experimental Details for Chapter 6**

### **Chemicals and Materials.**

Cobalt (II) nitrate hexahydrate was purchased from Alfa Aesar. 2-methylimidazole (2mIm, 99%) and imidazole was purchased from Acros Organics. Methanol (MeOH), sulfuric acid ( $\text{H}_2\text{SO}_4$ ), hydrogen peroxide ( $\text{H}_2\text{O}_2$ , 30%) and microscope slides were purchased from Fisher Scientific. Ethanol (EtOH 200 proof, anhydrous) was purchased from Decon Laboratories. All chemicals were used as received without further purification.

**Synthesis of ZIF-67 and ZIF-67 film.** ZIF-67 was synthesized by a reported method with some modification.<sup>124</sup> Typically, 30 mg of  $\text{Co}(\text{NO}_3)_2$  was dissolved in 5 mL MeOH and 272 mg 2mIm was dissolved in 5 mL of MeOH. After mixing two solutions, two pieces of glass slides etched with Piranha solution were immersed into the purple solution and sit for 2 h. The ZIF-67 film on glass slide was rinsed by MeOH and dried by  $\text{N}_2$  flow. ZIF-67 powder sample was obtained by centrifugation and washed with MeOH for three times.

**Synthesis of Im-ZIF-67 and Im-ZIF-67 film.** The imidazole doped sample was prepared by varying the percentage of Im in total imidazole linker. The amount of imidazole linkers for Im doped ZIF-67 was listed in Table 2-1. The Im-ZIF-67 films were prepared under the same treatment as ZIF-67 film.

Table 2-1 The varied amount of imidazole in the synthesis of Im-ZIF-67

Starting	2mIm (mg)	Im (mg)
0.02-Im	272	0
0.05-Im	266.6	4.5
0.1-Im	245	22.6

## 2.6. Experimental Details for Chapter 7

### Chemicals and Materials.

Cobalt (II) nitrate hexahydrate was purchased from Alfa Aesar. 2- methylimidazole (2mIm, 99%) was purchased from Acros Orvanics. Ruthenizer 535 (RuN3) was purchased from Solaronix. Methanol (MeOH), sulfuric acid (H<sub>2</sub>SO<sub>4</sub>), hydrogen peroxide (H<sub>2</sub>O<sub>2</sub>, 30%) and microscope slides were purchased from Fisher Scientific. Ethanol (EtOH 200 proof, anhydrous) was purchased from Decon Laboratories. Trimethylaluminum (98%) was purchased from Strem Chemicals. All chemicals were used as received without further purification.

### Treatment of glass slides.

Typically, the microscope slides were first cut into 1.2 cm × 2.5 cm pieces. The glass slides were then washed with acetone, ethanol and water under sonication for 10 mins and rinsed with water. After the first step cleaning, the glass slides were immersed into 40 mL of

Piranha solution (30 mL H<sub>2</sub>SO<sub>4</sub> and 10 mL H<sub>2</sub>O<sub>2</sub>) and set it for 30 mins. The etched slides were washed sufficiently with deionized (DI) water and kept in DI water for later use.

**Growth of ZIF-67 film.** The synthesis of ZIF-67 was followed by previously reported method.<sup>124</sup> Typically, 0.73 g Co(NO<sub>3</sub>)<sub>2</sub>·6H<sub>2</sub>O and 1.65 g 2mIm were dissolved in 50 mL MeOH, respectively. 4 mL of Co(NO<sub>3</sub>)<sub>2</sub> solution was added into 4 mL of 2mIm solution in 20 mL glass vial, where the mixture shows purple color. Two pieces of etched glass slides were immersed into the purple solution and sit for 1 h, during which ZIF-67 crystals form continuous and transparent thin film on the glass slides. The obtained ZIF-67 film was rinsed with MeOH and dried with N<sub>2</sub> flow. Because ZIF-67 films form on both sides of the glass, we scratched ZIF-67 off from one side of the film to make single-side ZIF-67 film.

#### **Atomic Layer Deposition of Al<sub>2</sub>O<sub>3</sub>.**

A GEMStar™ XT Atomic Layer Deposition System was used for the Al<sub>2</sub>O<sub>3</sub> deposition. The ZIF-67 films on glass slide were put at the center of the reactor. The gas lines of the system were held at 110°C to avoid precursor condensations. Trimethylaluminum (TMA) and H<sub>2</sub>O were used as Al and O sources, respectively, and were reacted at 120°C. The deposition process was performed in the following sequence: 0.05 s TMA pulse, 60 s exposure, 60 s N<sub>2</sub> purge, 0.05 s H<sub>2</sub>O pulse, 60 s exposure, 60 s N<sub>2</sub> purge. 10-40 cycles deposition cycles were applied to create 3-8.5 nm Al<sub>2</sub>O<sub>3</sub> layers. The morphology and thickness of the Al<sub>2</sub>O<sub>3</sub> were characterized by a HITACHI H-7700 TEM with an accelerating voltage of 100 kV. Due to the instability of ZIF-67 and ZIF-67 with 10 cycles of Al<sub>2</sub>O<sub>3</sub> under electron beam, a 100-cycle Al<sub>2</sub>O<sub>3</sub> deposited on ZIF-67 is measured by TEM.

## **2.7. Experimental Details for Chapter 8**

### **Chemicals and Materials.**

Cobalt (II) acetate, Zinc (II) acetate, Rhodamine B (RB) and 2-methylimidazole (2mIm, 99%) were purchased from purchased from Acros Organics. Cetyltrimethylammonium Bromide (CTAB) was purchased from EMD Millipore Corp. Methanol (MeOH), was purchased from Fisher Scientific. Ethanol (EtOH 200 proof, anhydrous) was purchased from Decon Laboratories. All chemicals were used as received without further purification.

### **Synthesis of ZIF-8.**

The synthesis of ZIF-8 followed a reported method.<sup>69</sup> 11.15 g 2mIm and 10 mg CTAB were dissolved into 50 mL deionized water. 5 mL of 2mIm solution was mixed with 5 mL Zinc acetate aqueous solution which contains 300 mg cobalt acetate under stirring for 10 s, followed by sitting for 2 h. ZIF-8 sample was obtained by centrifuging at 10000 rpm for 9 mins and washing with MeOH for 3 times.

### **Encapsulate RB into ZIF-8 (RB-ZIF-8).**

To encapsulate RB into ZIF-8 structure, a reported method was followed.<sup>69</sup> In addition to the synthesis of ZIF-8, 0.5 mL of 5 mM aqueous RB solution was added into the mixture of 2mIm solution and metal solution. The mixture was kept stirring for 10 s. The RB-ZIF-8 sample was obtained by centrifuging at 10000 rpm for 9 mins and washing with MeOH for 3 times.

**Synthesis of Cobalt doped RB-ZIF-8 (Co-RB-ZIF-8).** The synthesis procedure is similar to RB-ZIF-8. The only difference is adding different amount of cobalt acetate into the metal solution. The amount of the metal source was listed in Table 2-2.

Table 2-2 The amount of metal precursor in different samples.

<b>sample</b>	<b>Zn(CH<sub>3</sub>COO)<sub>2</sub></b>	<b>Co(CH<sub>3</sub>COO)<sub>2</sub></b>
RB/ZIF-8	300 mg	0
1 mg Co	299 mg	1 mg
2 mg Co	298 mg	2 mg
3 mg Co	297 mg	3 mg
5 mg Co	295 mg	5 mg
10 mg Co	290 mg	10 mg
20 mg Co	280 mg	20 mg

## Chapter 3

### Unravelling the Correlation of Electronic Structure and Carrier Dynamics in CuInS<sub>2</sub> Nanoparticles

#### 3.1 Introduction

Colloidal semiconductor nanocrystals are under intense investigation due to their wide range of applications including solar cells, light-emitting diodes, catalysis, and bioimaging<sup>127-129</sup>. However, most of the previous works have focused on using semiconductors based on toxic elements such as Cd and Pb,<sup>43, 130-132</sup> which largely limits their practical applications. As a result, recent efforts have been geared toward low toxicity multinary nanocrystals such as copper indium sulfide (CIS). These nanocrystals possess tunable band structure and optical properties, which have led to their use in optoelectronics and biological applications.<sup>127, 130</sup> They have high extinction coefficient, emission quantum yield, and appropriate band gaps, which have rendered these nanocrystals desirable as light-harvesting and charge separation materials in photovoltaics and photocatalysis.<sup>133-137</sup>

As the functions of CIS in these applications are mainly dictated by their light-absorbing and emission behaviors, it is essential to develop a deep understanding of the excited state dynamics of CIS. Indeed, there are a handful of recent reports that have explored the excited state properties of CIS or CIS based nanocrystals using time-resolved spectroscopic techniques.<sup>138-140</sup> For example, a few studies have reported the origins of the extremely long radiative lifetimes and large Stokes shift of CIS vs CdSe nanocrystals, which was attributed to the presence of Cu-related intragap emission center.<sup>37, 141-143</sup> Other studies based on transient absorption spectroscopy have explained the multiple-component carrier cooling and recombination dynamics, which was assigned to the transition involving the

band gap, sub-band gap, or surface trap states.<sup>36, 144-145</sup> While these studies provide valuable information on the excited state properties of CIS nanocrystals, few efforts have been made to explore the correlation of these optical properties with their electronic structure, yet they are essential to fully understand the photophysical properties of CIS as a whole.

In this project, I investigated the direct correlation of carrier dynamics with electronic structure of CIS nanoparticles (NPs) using the combination of synchrotron-based X-ray absorption (XAS) and X-ray transient absorption (XTA) spectroscopies and optical transient absorption (OTA) spectroscopy. We found that CIS NPs contain large amount of surface Cu atoms without tetrahedral coordination, which likely serve as hole trapping sites during the photoinduced trapping process. The surface structure of Cu site in CIS NPs can be controlled by the nucleation time during synthesis, where tetrahedral structure of Cu center is more developed in CIS NPs with longer nucleation time, which leads to longer electron-hole recombination time, suggesting the possibility to control the carrier dynamics by controlling the surface structure of CIS NPs. This study provides important insight into the correlation of carrier dynamics with surface structure of CIS NPs, which will facilitate rational design of CIS NPs toward their application in photovoltaic and light-emitting devices.

### **3.2 Results and discussion**

The synthesis of CIS with different size was summarized in chapter 2. The bulk structure of CIS NPs synthesized under three different nucleation times was first characterized using X-ray diffraction (XRD). As shown in Figure 3-1, the XRD patterns of these NPs show three main peaks with  $2\theta$  values of  $28.0^\circ$ ,  $46.5^\circ$ , and  $54.9^\circ$ , which are consistent with

literature values and can be assigned to the (112), (204)/ (220), and (116)/ (312) planes of tetragonal chalcopyrite structure of CIS, respectively.<sup>36, 146-148</sup>

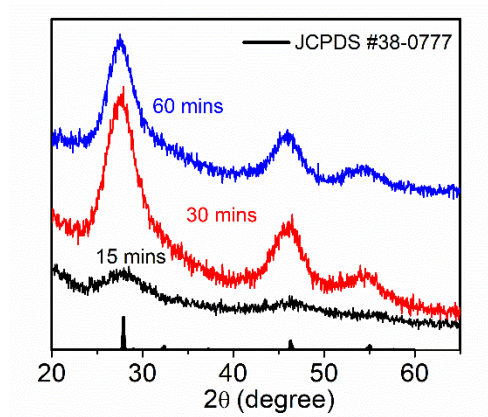


Figure 3-1 XRD patterns of CIS NPs synthesized with nucleation time 15, 30, and 60 min.

To obtain the size information of as prepared CIS NPs, the small-angle X-ray scattering (SAXS) measured at 12ID-B of the Advanced Photon Source at Argonne National Laboratory. As shown in Figure 3-2 a and b, the scattering profiles of these samples could all be fit with spherical particle model<sup>149</sup> with mean radius of 9.8, 12.2, and 14.7 Å for 15, 30, and 60 min, respectively. The sizes of these CIS NPs are smaller than the Bohr exciton radius (3.8 nm) of bulk CIS,<sup>150-151</sup> indicating a strong quantum confinement effect, which explains the strong dependence of optical properties on sizes. The quantum confinement effect was confirmed by the UV-vis absorption spectra and emission spectra which were shown in Figure 3-3a and 3-3b respectively. These UV-visible spectra (Figure 3-3a) show broad absorption with the lack of a well-defined excitonic peak, which are commonly seen

in CIS NPs and result from the inhomogeneity of the band gap states.<sup>136, 143</sup> The presence of multiple donor and trap states within the band gap leads to the formation of a broad

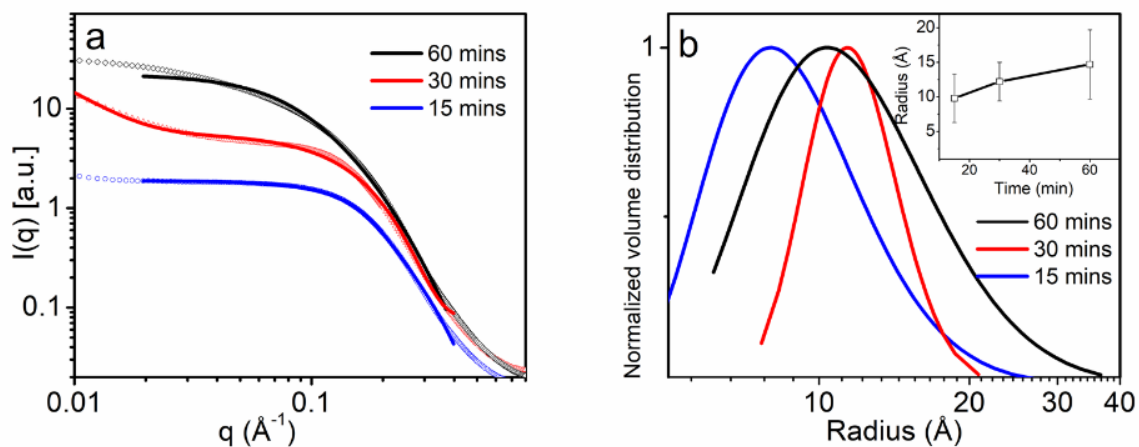


Figure 3-2 (a) SAXS data (symbols) and fit (solid lines) using spherical particle model whose size follows log-normal distribution. (b) Particle radius distribution yielded from the SAXS data fitted under spherical shape assumption of CIS NPs synthesized with nucleation time 15, 30, and 60 min.

shoulder. Meanwhile, the shoulders of these spectra as well as their corresponding emission spectra (Figure 3-3b) show red shift with increasing nucleation time, which can be attributed to the reduction of quantum confinement effects from the increase of particle dimensions.

In addition to the bulk structure, the effect of the nucleation time on the local structure was examined using X-ray absorption spectroscopy (XAS). Figure 3-4a shows the normalized X-ray absorption near-edge structure (XANES) spectra of CIS NPs at Cu K-edge. All three spectra show a peak at 8.986 keV and a broad transition from 8.99 to 9.01

keV. These features have been previously observed in chalcopyrite NPs and can be assigned to  $1s-4p_z$  and  $1s-4p_{xy}$  transitions of  $\text{Cu}^{1+}$ , respectively.<sup>152-153</sup> The  $\text{Cu}^{1+}$  oxidation state was further supported by the absence of the pre-edge feature at  $\sim 8.98$  keV (inset of Figure 3-4a), which represents the quadrupole  $1s-3d$  transition of Cu center and is only allowed if there is  $\text{Cu}^{2+}$  with  $3d^9$  configuration.<sup>152</sup> Meanwhile, the edge energy shows negligible shift among these samples (inset of Figure 3-4a), suggesting that the oxidation

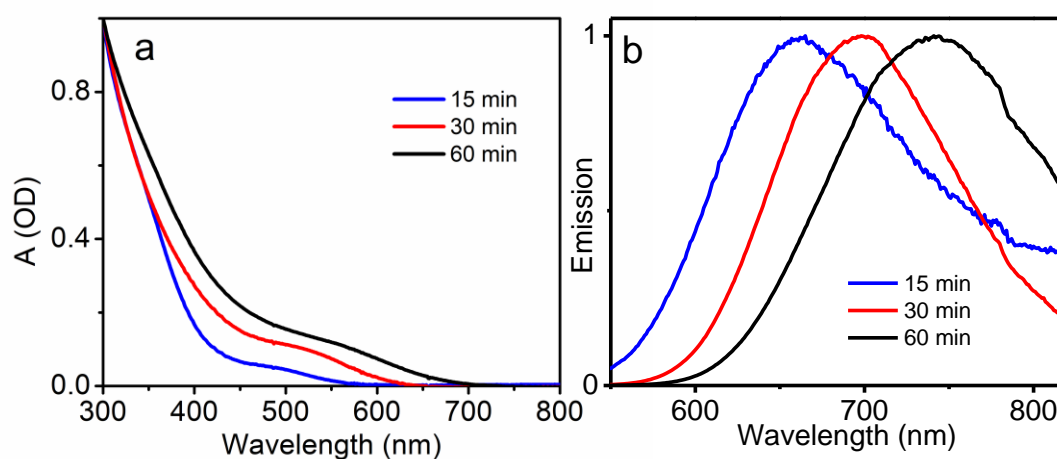


Figure 3-3 UV-visible absorption spectra (a) and emission spectra (b) of CIS NPs synthesized with different nucleation time

state of  $\text{Cu}^{1+}$  retains regardless of nucleation time. However, notable differences were observed in the peak corresponding to  $1s-4p_z$  transition, where the peak becomes sharper in the spectra of the NPs with longer nucleation time. It has been shown that the sharp nature of  $1s-4p_z$  transition is an indication of tetrahedrally coordinated Cu, while a smoother feature is characteristic of triangular coordination.<sup>153-154</sup> These results suggest that the tetrahedral structure of  $\text{Cu}^{1+}$  is more developed in the 60 min sample than in samples with shorter nucleation times. Additional difference was observed among these samples in their extended X-ray absorption fine structure (EXAFS) spectra in R-space,

where the intensity of the peak representing Cu–S shows slight increase with increasing nucleation time (Figure 3-4b). It has been shown that the increase of peak intensity is associated with either the increasing coordination number or the decrease of disorder around the metal center.<sup>155</sup>

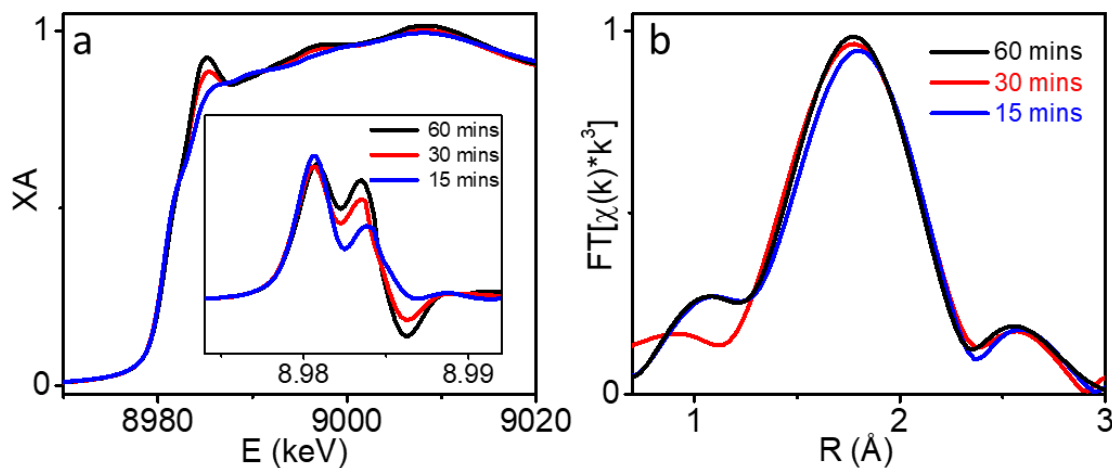


Figure 3-4 Comparison of XANES spectra (a) and Fourier-transformed EXAFS spectra (b) of CIS NPs synthesized with different nucleation time. Inset: first derivative of the XANES spectra

To gain more insight into these two possibilities, we quantitatively analyzed the local structure of these NPs through fitting EXAFS data using IFEFF modeling. Figure 3-5 shows the best fits to the EXAFS spectra in both R- and k-space for all three samples. The resulting fitting parameters are listed in Table 3-1. While the Cu–S bond distance shows negligible change among three samples notable increase of coordination number of Cu and slight increase of Debye–Waller factor

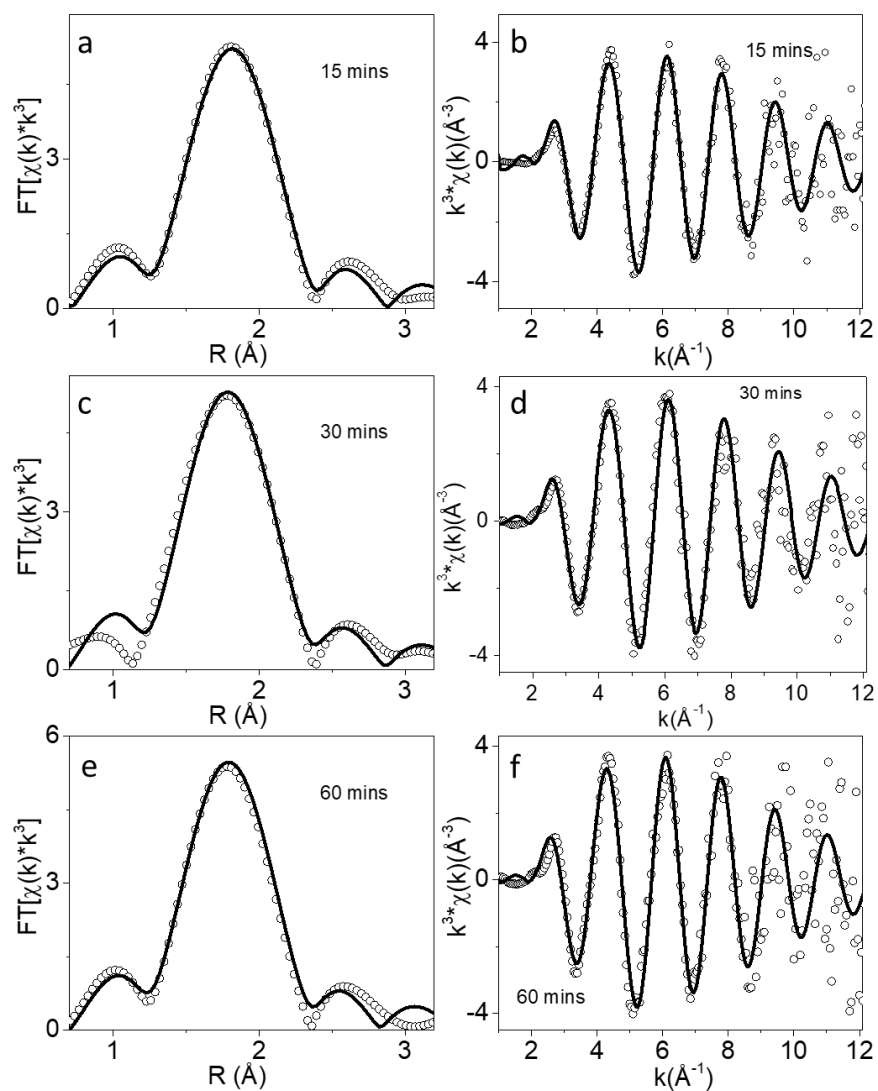


Figure 3-5 XAFS spectra (open dot) and the best fit (solid line) of CIS NPs in R-space and k space with nucleation times 15 min (a, b), 30 min (c, d), and 60 min (e, f), respectively.

were observed with nucleation time, suggesting that the enhanced peak intensity in NPs with nucleation time (Figure 3-4a) is primarily due to the increase of average coordination number at Cu center. This is consistent with the XANES results, where the CIS NPs with longer nucleation time contain more four-coordinated tetrahedral Cu centers than those

with shorter nucleation time. Furthermore, it is noted that the average coordination number of Cu center in all samples is  $\sim 2$ , which is only half of the expected coordination number in a tetrahedrally coordinated Cu center. This has been observed previously in similar semiconductor nanoparticles and can be attributed to the presence of a large number of vacancy defects at surface Cu centers, which do not possess tetrahedron.<sup>156-157</sup> These results together suggest that a larger portion of surface Cu atoms with nontetrahedral coordination is present in smaller CIS NPs synthesized under shorter nucleation times, which leads to the less developed tetrahedral Cu center and smaller average coordination number at Cu center uncovered by XAS. The presence of a large percentage of surface Cu atoms in CIS NPs also well explains the observed poorly defined excitonic peak and broad shoulder in UV–visible spectra, large Stokes shift, as well as the presence of multiple trap states within CIS band gap.

Table 3-1. XAFS fitting parameters for CIS

Vector	15 mins			30 mins			60 mins		
	N	R (Å)	$\sigma^2(10^{-3}\text{Å}^2)$	N	R (Å)	$\sigma^2(10^{-3}\text{Å}^2)$	N	R (Å)	$\sigma^2(10^{-3}\text{Å}^2)$
Cu-S	2.05±0.18	2.27±0.02	6.7 ±1.4	2.24±0.33	2.28±0.02	7.4±2.3	2.36±0.21	2.28±0.02	8.0±1.4

To reveal the effect of surface defects on the photophysical properties of CIS NPs, we examined its carrier dynamics using femtosecond transient optical absorption (fs-OTA) spectroscopy. Figure 3-6 shows the fs-OTA spectra of these samples following 480 nm excitation. All spectra (Figure 3-6 a–c) were featured by a prominent ground-state bleach (GSB) band, which shifts to longer wavelength with nucleation time (Figure 3-6d),

consistent with their UV–visible absorption spectra (Figure 3-3 a). Meanwhile, broad absorption bands were observed on both sides of the GSB for each sample. Similar absorption features have been observed previously and can be assigned to the photoinduced electron signals as these features are quenched upon the addition of an electron acceptor, i.e., methyl viologen hydrate.<sup>147</sup>

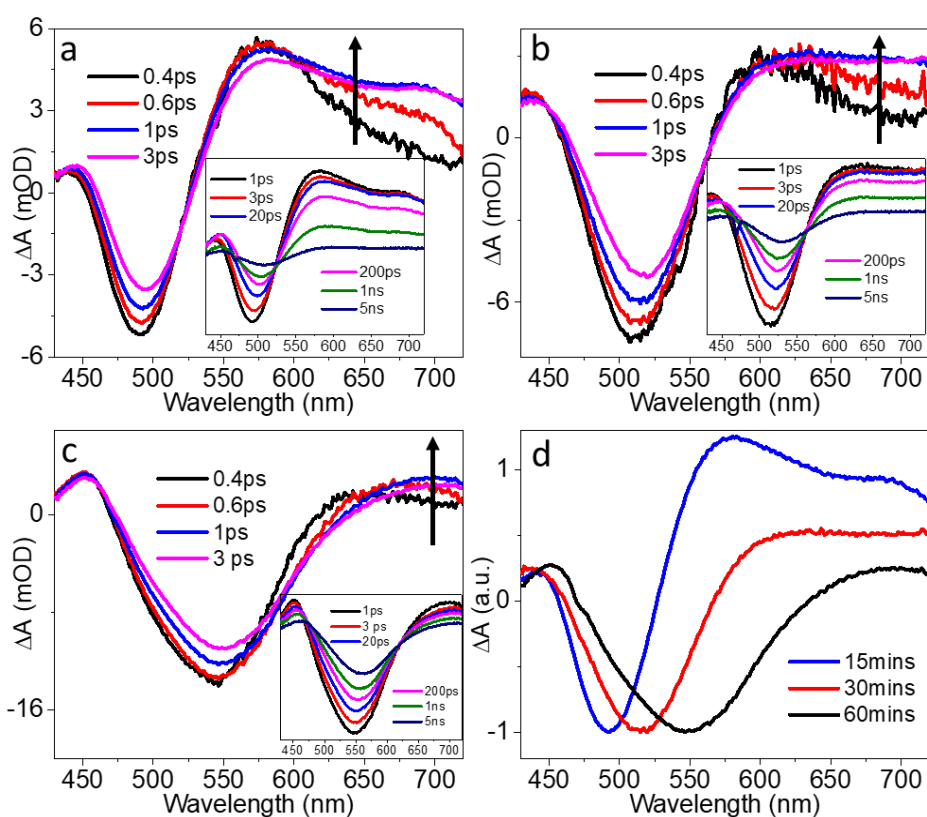


Figure 3-6 Femtosecond OTA spectra of CIS NPs with 15 mins (a), 30 mins (b), and 60 mins nucleation time following 480 nm excitation. (d) The comparison of 1 ps TA spectra of CIS NPs at different nucleation times. The insets show the late time spectra.

To further analyze the carrier dynamics of CIS NPs, we compared the kinetic traces of GSB and photoinduced electron signals among the samples with different nucleation times.

As shown in Figure 3-7 a–c, the kinetic traces of electron absorption dynamics are strongly dependent on probe wavelengths, characteristic of carrier-trapping process, indicating that electron-trapping process<sup>152, 158-159</sup> occurs in each sample. The kinetic traces at different probe wavelength for each sample can be adequately fit by a four-exponential function,

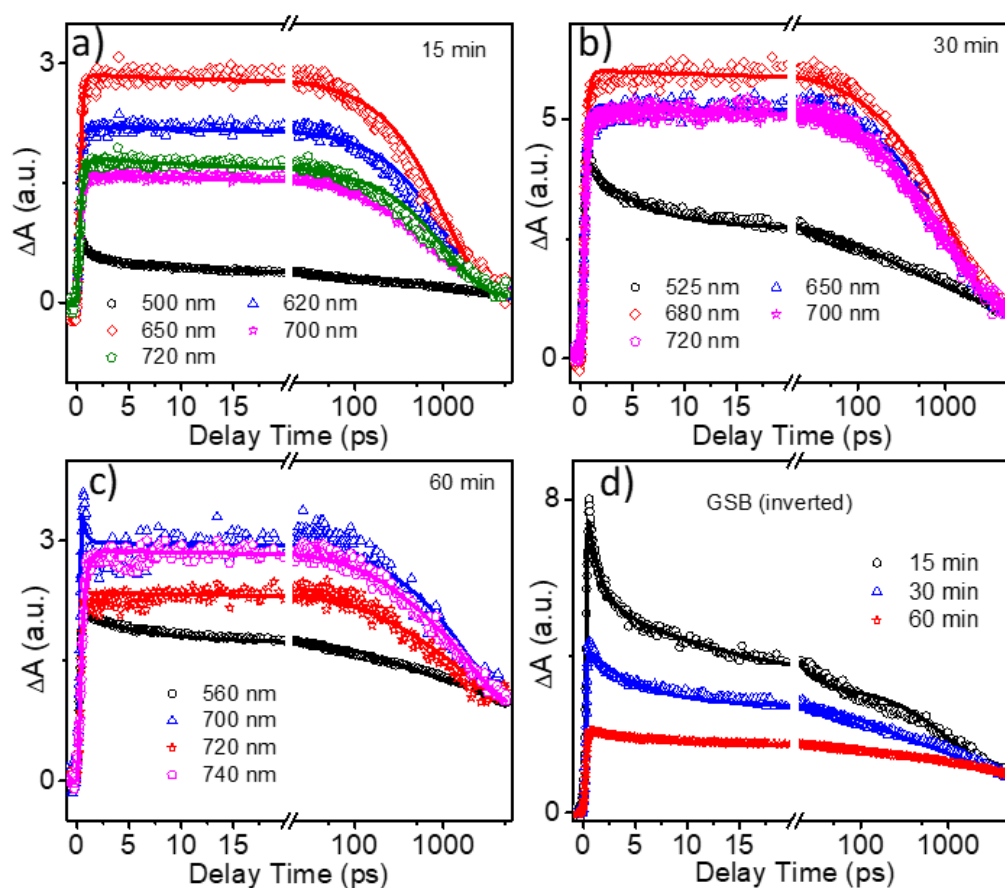


Figure 3-7 The comparison of OTA kinetic traces of CIS NPs at various probe wavelengths for samples with 15 mins (a), 30 mins (b), and 60 mins (c) nucleation time following 480 nm excitation. (d) The comparison of ground state bleach recovery kinetics (inverted) for 15min, 30 mins, and 60 mins samples.

including an ultrafast rising/decay time constant followed by three decay components. We attributed the ultrafast sub picosecond component for all samples to electron-trapping process, which remains relatively similar among the three samples as shown in Table 3-2. We attributed the three decay components to electron–hole recombination which was fixed during the fitting process according to the rationale that the late time decay kinetics at different wavelengths remain similar. While there is no clear dependence of electron-trapping time on sample nucleation time, notable difference was observed in the GSB recovery kinetics. As shown in Figure 3-7 d, the GSB recovery (inverted) slows down with nucleation time, suggesting a slower electron–hole recombination process. Due to the presence of  $\gg 5$  ns time constant which is beyond the fs-OTA time window, we are not able to quantitatively determine the charge recombination time. Instead, half recovery time ( $\tau_{1/2}$ ), when the amplitude of GSB recovers to its half, was used to evaluate the charge recombination time. The estimated  $\tau_{1/2}$  was 15.2, 169.9, and 5033 ps for 15, 30, and 60 min sample, respectively, indicating the elongated electron–hole recombination time in CIS NPs synthesized using longer nucleation time.

In addition to the carrier dynamics, the nature of trap states was investigated by probing the oxidation state change at Cu center using time-resolved X-ray absorption spectroscopy (XTA). Figure 3-8 shows the XANES spectrum of CIS NPs with 60 min nucleation time at Cu K-edge without laser excitation (laser-off spectrum). This spectrum resembles the XANES spectrum in Figure 3-4a, representing the steady-state XANES spectrum of CIS NPs. Also shown in Figure 3-8 a is the transient XANES signal, presented as the difference XANES spectrum obtained by subtracting the steady-state XANES spectrum from the XANES spectrum with laser excitation at 110 ps (laser-on spectrum). A prominent negative

feature at 8.983 keV in the difference spectrum indicates that the Cu transition edge shifts to higher energy, suggesting the oxidation at Cu center following photoexcitation.<sup>160</sup> This assignment was further confirmed by the small positive feature at 8.98 keV which

Table 3-2. Fitting Parameters for TA Kinetics of CIS NPs

Nucleation time	Probe	$\tau_1, \text{ps}$	(A <sub>1</sub> ,%)	$\tau_2, \text{ps}$	(A <sub>2</sub> ,%)	$\tau_3, \text{ps}$	(A <sub>3</sub> ,%)	$\tau_4, \text{ps}$	(A <sub>4</sub> ,%)
15 min	500 nm	$1.09 \pm 0.13$	30.5		29.1		27.4		13
	620 nm	$r 0.23 \pm 0.01$	100		2.0		93.5		4.5
	650 nm	$r 0.23 \pm 0.01$	100	$13.9 \pm 3.7$	1.9	$1040 \pm 27$	95.2	$\gg 5 \text{ ns}$	2.9
	700 nm	$r 0.29 \pm 0.01$	100		6.1		88.1		5.8
	720 nm	$r 0.32 \pm 0.01$	100		7.9		87.5		4.9
30 min	525 nm	$4.58 \pm 0.17$	33		17.8		23.9		25.4
	650 nm	$r 0.27 \pm 0.01$	100		5.0		73.3		16.7
	680 nm	$r 0.25 \pm 0.01$	100	$135 \pm 4.5$	7.9	$1190 \pm 43$	75.5	$\gg 5 \text{ ns}$	16.6
	700 nm	$r 0.35 \pm 0.01$	100		10.8		70.7		18.5
	720 nm	$r 0.31 \pm 0.01$	100		13.2		67.8		19.0
60 min	560 nm	$5.79 \pm 0.19$	16.1		14.1		22.2		47.4
	700 nm	$0.35 \pm 0.01$	19.6		7.37		50		22.9
	720 nm	$r 0.14 \pm 0.01$	100	$237 \pm 7.8$	15.1	$1990 \pm 76$	47.8	$\gg 5 \text{ ns}$	37.8
	740 nm	$r 0.38 \pm 0.01$	100		14.7		54.8		30.5

\*r Rising Component in a Multiexponential Function

to quadrupole 1s–3d transition. Because 1s–3d transition is forbidden in Cu<sup>1+</sup> with 3d<sup>10</sup> configuration but is possible in Cu<sup>2+</sup> center, the appearance of this transition indicates the oxidation of Cu center. Because the full-width at half-maximum (fwhm) of X-ray probe is ~117 ps and electron trapping process occurs on a sub picosecond time scale revealed by fs-OTA, the XTA spectrum collected at 110 ps after laser excitation represents the spectrum when electron-trapping process has completed. As a result, the observed oxidation at Cu center indicates that the electrons are removed from Cu site and trapped at

the surrounding sites, such as In or S sites (Figure 3-8 b), implying that holes are located at sites characteristic of Cu. We are unsure whether the holes at Cu center are located in valence band or trap states. However, due to the presence of large amount of surface Cu atoms with defects, as indicated by XAS, we believe that trapped holes play a major role in the oxidation of Cu center, though holes at valence band cannot be excluded.

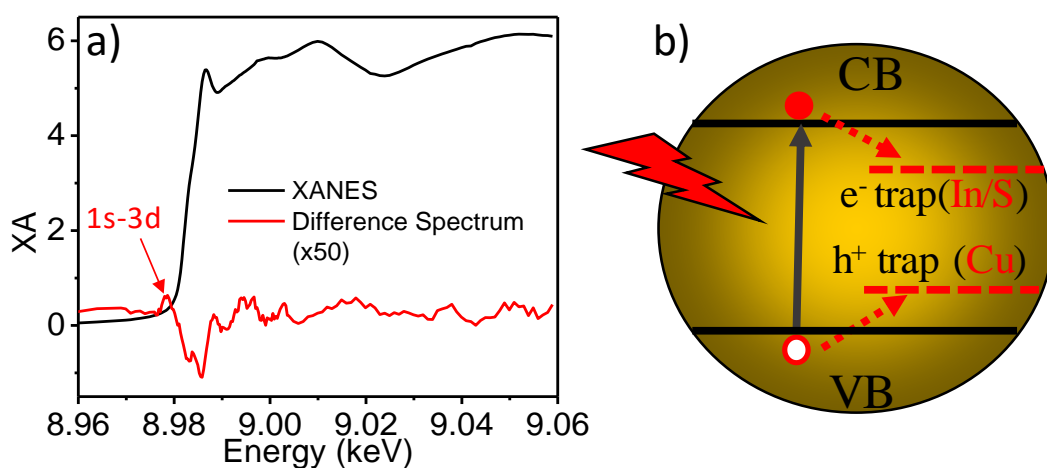


Figure 3-8 (a) XANES spectrum (black plot) and difference XANES spectrum (red plot) of CIS NPs with 60 min nucleation time at Cu K-edge. The difference XANES spectrum was obtained after subtracting the XANES spectrum without laser excitation from the XANES spectrum collected at 110 ps after laser excitation. (b) Scheme illustration of carrier dynamics in CIS NPs following photoexcitation.

### 3.3 Conclusion

In summary, we have examined the correlation of the photoinduced carrier dynamics in CIS NPs with their electronic structure using the combination of multiple spectroscopic techniques. Using steady-state and time-resolved XAS spectroscopy, we show that CIS NPs contain a large portion of surface Cu atoms that do not have tetrahedral structure,

which serve as hole-trapping sites. The structure of surface Cu atoms in CIS NPs can be controlled by nucleation time during synthesis, where the tetrahedral structure at Cu center is more developed in NPs with longer nucleation time (larger size), resulting in longer electron-hole recombination time. These results indicate the possibility to inhibit carrier recombination through controlling the electronic structure of surface Cu atoms, providing important insight in fundamental understanding of carrier dynamics in CIS NPs and facilitating their potential application in photovoltaics and light-emitting devices.

Chapter 4  
Composition Effect on the Carrier Dynamics and Catalytic Performance of CuInS<sub>2</sub>/ZnS  
Quantum Dots for Light Driven Hydrogen Generation

## 4.1 Introduction

The efficient conversion and storage of solar energy represent a promising approach to address the increased energy demand and environmental problems caused by the combustion of fossil fuels.<sup>1-3</sup> One attractive strategy for solar energy conversion is light-driven water splitting to generate H<sub>2</sub> based on semiconductor photocatalysts.<sup>8, 161</sup> Since the first report of light-driven photocatalytic H<sub>2</sub> generation based on semiconductors,<sup>11, 42</sup> various semiconductor nanocrystals have been reported as photocatalytic materials.<sup>41, 162-163</sup> Among them, CuInS<sub>2</sub> (CIS) quantum dots (QDs), known as colloidal semiconductor nanocrystals, have become one of the most promising semiconductor photocatalytic materials for H<sub>2</sub> generation due to their large optical absorption coefficient, tunable bandgap, and high photostability.<sup>39, 164-166</sup> However, majority of CIS based systems reported are decorated with cocatalysts, where CIS mainly serves as a photosensitizer.<sup>32, 167-172</sup> In contrast to these reports, we recently found that CIS/ZnS core/shell QDs alone can efficiently catalyze the H<sub>2</sub> evolution reaction (HER) in an aqueous solution with an exceptionally long lifetime.<sup>147</sup> While this finding demonstrated the promise of CIS/ZnS as a single-component photocatalyst for the HER, the solar-to-H<sub>2</sub> quantum yield is quite low (<1%). Given the promising properties of this single-component system for the HER, it is necessary to further explore this system to improve its quantum efficiency for H<sub>2</sub> generation. Previous studies have shown that one critical limitation of CIS QDs to their application in photovoltaics and photocatalysis is associated with the surface related defect

states, which results in defect-induced nonradiative transition and poor emission quantum yield.<sup>36, 140-141, 173</sup> A number of experimental and theoretical studies have demonstrated that the surface defect states in CIS QDs can originate from sulfur vacancy ( $V_S$ ), copper site substituted by indium ( $In_{Cu}$ ), copper vacancy ( $V_{Cu}$ ), indium vacancy ( $V_{In}$ ), and indium site substituted by copper ( $Cu_{In}$ ), where  $V_S$  and  $In_{Cu}$  act as the donors and  $V_{Cu}$ ,  $V_{In}$ , and  $Cu_{In}$  act as acceptors.<sup>40, 174-175</sup> In general, in Cu rich CIS QDs, the main transitions are from the conduction band to  $V_{In}$  or  $Cu_{In}$  and from  $V_S$  to the valence band. In Cu deficiency CIS QDs, the main transitions should be from  $V_S$  to  $V_{Cu}$  and from  $In_{Cu}$  to  $V_{Cu}$ .<sup>38, 144, 176</sup> These literature data suggested that the defect states in CIS are largely dependent on their composition, and altering the composition of CIS may serve as a viable approach to tune their photophysical properties and photocatalytic activity for the HER.

In this project, I investigated the effect of cation composition on the carrier dynamics, charge separation, and photocatalytic performance of CIS/ZnS QDs for light driven  $H_2$  generation in an aqueous solution, where the ratio of Cu to In cations was systematically varied. We show that decreasing Cu to In ratio (increasing Cu deficiency) leads to slightly faster electron-hole pair recombination but significantly enhanced photocatalytic performance for the HER. This can be explained by improved overall charge separation due to faster electron transfer (ET) from the sacrificial donor to CIS/ZnS QDs in the sample with higher Cu deficiency resulting from the more positive valence band edge.

## 4.2 Results and discussion

Figure 4-1(a) shows the XRD patterns of CIS/ZnS with different Cu to In ratios. The Cu to In ratios of these samples were measured by EDX (Table 4-1) and were used to label these samples. All samples show three main peaks with  $2\theta$  values at  $27.8^\circ$ ,  $46.9^\circ$ , and  $54.9^\circ$ ,

which agree well with the literature data and support the formation of CIS/ZnS.<sup>146, 148</sup>

Figure 4-1(b) shows the UV-visible absorption spectra of CIS/ZnS with four different ratios, which are featured by shoulder absorption bands at around 500 nm corresponding to the optical bandgap.<sup>177</sup> With decreasing Cu to In ratio (increasing Cu deficiency), these absorption bands shift to a shorter wavelength, suggesting increasing bandgap between

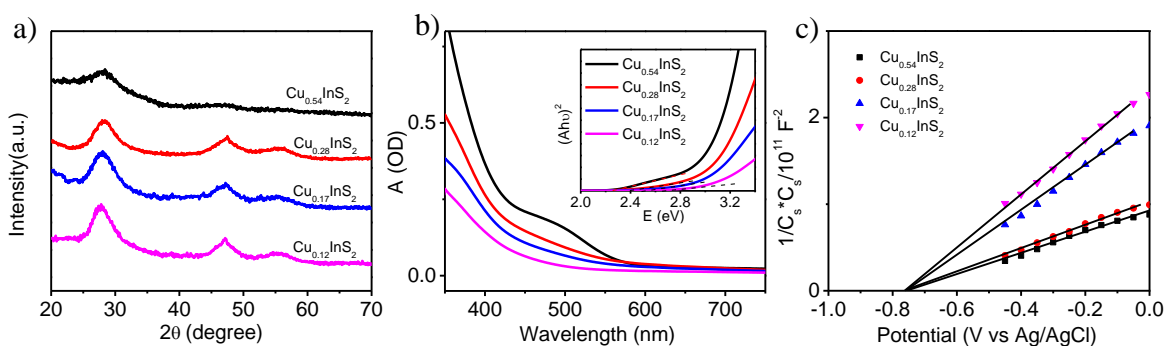


Figure 4-1 XRD patterns (a), UV-visible absorption spectra (b) and (c) Mott-Schottky plots for CIS/ZnS QDs with different Cu to In ratios.

Table 4-1. EDX results and sample name of CIS/ZnS with different Cu to In ratios

Synthesis ratio	EDX Results	Sample name
0.5	0.54	Cu <sub>0.54</sub> InS <sub>2</sub>
0.2	0.28	Cu <sub>0.28</sub> InS <sub>2</sub>
0.125	0.17	Cu <sub>0.17</sub> InS <sub>2</sub>
0.1	0.12	Cu <sub>0.12</sub> InS <sub>2</sub>

conduction and valence bands. Via the least-square fit of the linear region of a  $(Ahv)^2$  vs  $hv$  plot (A, absorbance; h, Planck's constant and  $\nu$ , frequency),<sup>30</sup> the bandgaps of these

CIS/ZnS QDs were estimated to be 2.25 eV, 2.40 eV, 2.50 eV, and 2.65 eV for QDs with  $\text{Cu}_{0.54}\text{InS}_2$ ,  $\text{Cu}_{0.28}\text{InS}_2$ ,  $\text{Cu}_{0.17}\text{InS}_2$  and  $\text{Cu}_{0.12}\text{InS}_2$  respectively (Inset of Figure 4-1b).

In addition, the conduction band edges of these QDs were estimated by Mott-Schottky plots (Figure 4-1c),<sup>178</sup> where a similar conduction band edge ( $\sim 0.75$  eV vs Ag/AgCl) was obtained for these CIS/ZnS QDs, suggesting that altering the Cu to In ratio within the 0.54:1 to 0.12:1 range has negligible impact on the conduction band edge. This also suggests that the change of bandgap with the Cu to In ratio is likely due to the shift of the valence band position, i.e., the valence band edge moves to more positive potential with increasing Cu deficiency. These results are consistent with previously reported data,<sup>179-180</sup> suggesting the validity of the models we used to estimate the bandgap and conduction band edge.

The emission spectra of these samples following excitation at 400 nm are shown in Figure 4-2a. The emission peak position shifts from 600 nm to 554 nm with increasing Cu deficiency. This follows the same trend as their absorption spectra, further supporting that increasing Cu deficiency results into the increase of band gap of CIS/ZnS. The emission quantum yield (QY) is estimated to be 20%, 11%, 9%, and 8% for QDs with  $\text{Cu}_{0.54}\text{InS}_2$ ,  $\text{Cu}_{0.28}\text{InS}_2$ ,  $\text{Cu}_{0.17}\text{InS}_2$  and  $\text{Cu}_{0.12}\text{InS}_2$  respectively, which decreases with increasing Cu deficiency and suggests more defect states in the sample with higher Cu deficiency (Figure 4-2b). In order to gain insight on the average emission lifetime of CIS/ZnS QDs with different Cu to In ratios, the time resolved emission spectra of these samples were measured following 400 nm excitation. Figure 4-2c shows the time-resolved emission lifetime decay kinetics of CIS/ZnS QDs with different Cu to In ratio. It can be seen that  $\text{Cu}_{0.12}\text{InS}_2$  has the

fastest decay, indicating the shortest average emission lifetime. The decay curves of the samples were fitted with a tri-exponential decay function:

$$I(t) = A_1 \exp(-t/\tau_1) + A_2 \exp(-t/\tau_2) + A_3 \exp(-t/\tau_3) \quad (1)$$

where  $A_1$ ,  $A_2$  and  $A_3$  are fractional contributions of PL decay lifetimes of  $\tau_1$ ,  $\tau_2$  and  $\tau_3$ , respectively. The fitting results are listed in Table 4-2. The obtained average lifetimes of these samples are 133.3 ns for  $\text{Cu}_{0.54}\text{InS}_2$ , 123.4 ns for  $\text{Cu}_{0.28}\text{InS}_2$ , 117.5 ns for  $\text{Cu}_{0.17}\text{InS}_2$  and 113.2 ns for  $\text{Cu}_{0.12}\text{InS}_2$ , which shows that the emission lifetimes of these samples are similar with minor trend showing decreasing emission lifetime with increasing Cu

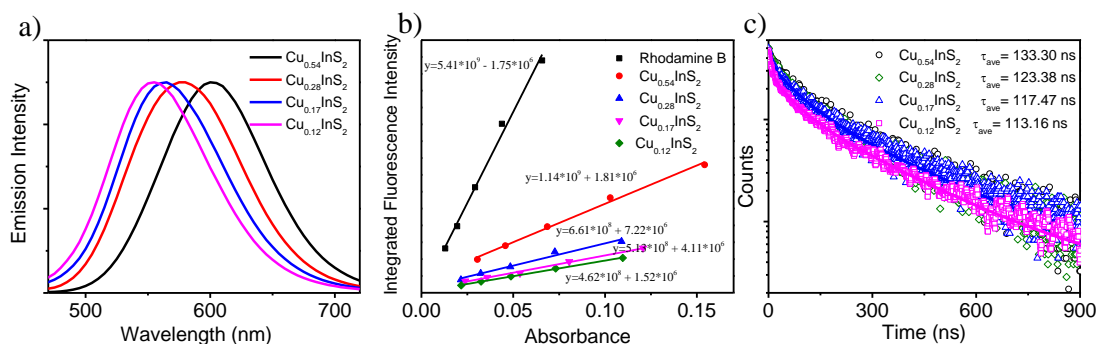


Figure 4-2 (a) emission spectra, (b) the plots of integrated fluorescence intensity vs absorbance and (c) emission lifetime decay kinetics of CIS/ZnS QDs with different Cu to In ratios. The excitation wavelength for emission spectra and emission lifetime measurement is at 400 nm. The probing wavelength is 600 nm, 580 nm, 550 nm, and 550 nm for samples with  $\text{Cu}_{0.54}\text{InS}_2$ ,  $\text{Cu}_{0.28}\text{InS}_2$ ,  $\text{Cu}_{0.17}\text{InS}_2$  and  $\text{Cu}_{0.12}\text{InS}_2$ , respectively.

deficiency. These results also suggest that different Cu to In ratio in the CIS/ZnS QDs has negligible impact on electron-hole carrier recombination time.

Table 4-2. Fitting Parameters for PL decays of CIS/ZnS with different Cu to In ratios

	$\tau_1$ (ns) (A1)	$\tau_2$ (ns) (A2)	$\tau_3$ (ns) (A3)	average (ns)
$\text{Cu}_{0.54}\text{InS}_2$	14.35 (21.84)	86.25 (51.17)	318.78 (26.99)	133.3
$\text{Cu}_{0.28}\text{InS}_2$	9.98 (22.16)	73.85 (48.58)	291.57 (29.16)	123.4
$\text{Cu}_{0.17}\text{InS}_2$	8.92 (23.89)	70.66(42.73)	256.12 (33.38)	117.5
$\text{Cu}_{0.12}\text{InS}_2$	7.73 (27.19)	62.84 (37.1)	245.66 (35.71)	113.2

The carrier recombination dynamics of CIS/ZnS QDs with different Cu to In ratios was further investigated using femtosecond transient absorption (TA) spectroscopy to unravel the early time carrier relaxation dynamics. The TA spectra of these samples were all collected under 400 nm excitation with  $20 \mu\text{J}/\text{cm}^2$  power. Shown in [Figure 4-3](#) are the TA spectra of CIS/ZnS QDs, where the inset shows the early time spectra. The TA spectra of all four CIS/ZnS QDs samples were featured by a negative band and a broad positive absorption, where the former can be assigned to the exciton bleach band and the latter can be attributed to the electron absorption.<sup>147, 181</sup> It can be clearly seen that the exciton bleach band shifts to shorter wavelength with increasing Cu deficiency,

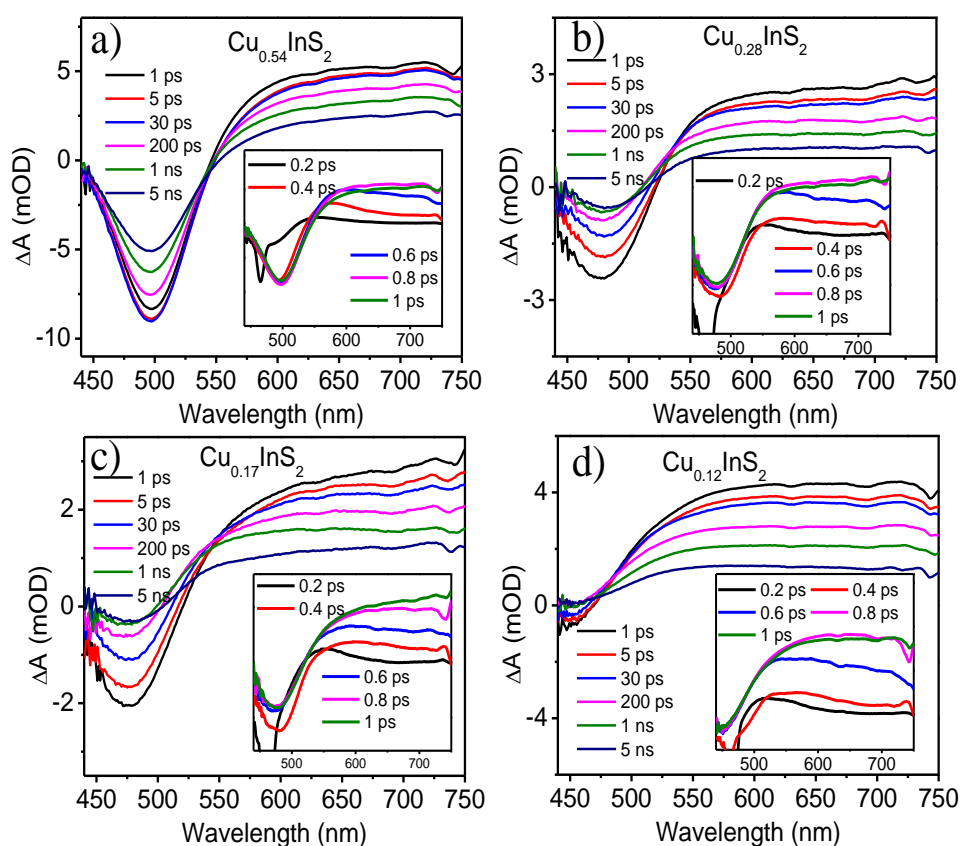


Figure 4-3. Femtosecond transient absorption spectra of CIS/ZnS QDs with different Cu to In ratios: (a)  $\text{Cu}_{0.54}\text{InS}_2$ ; (b)  $\text{Cu}_{0.28}\text{InS}_2$ ; (c)  $\text{Cu}_{0.17}\text{InS}_2$ ; (d)  $\text{Cu}_{0.12}\text{InS}_2$ . The excitation wavelength is at 400 nm.

which is consistent with the UV-vis absorption and emission results above. As shown in the inset of [Figure 4-3](#), the early time spectra (< 1 ps) for all four samples show an ultrafast rising component for the electron absorption signal. This component can be attributed to electron trapping and/or cooling process, which is based on both literature and our own experimental results. Previous data has shown that this rising component can be attributed to electron trapping process,<sup>173, 182-183</sup> while our experiments show that the rising component disappears when 450 nm light was used as excitation wavelength ([Figure 4-4](#)), suggesting that the cooling process contributes to this rising component.

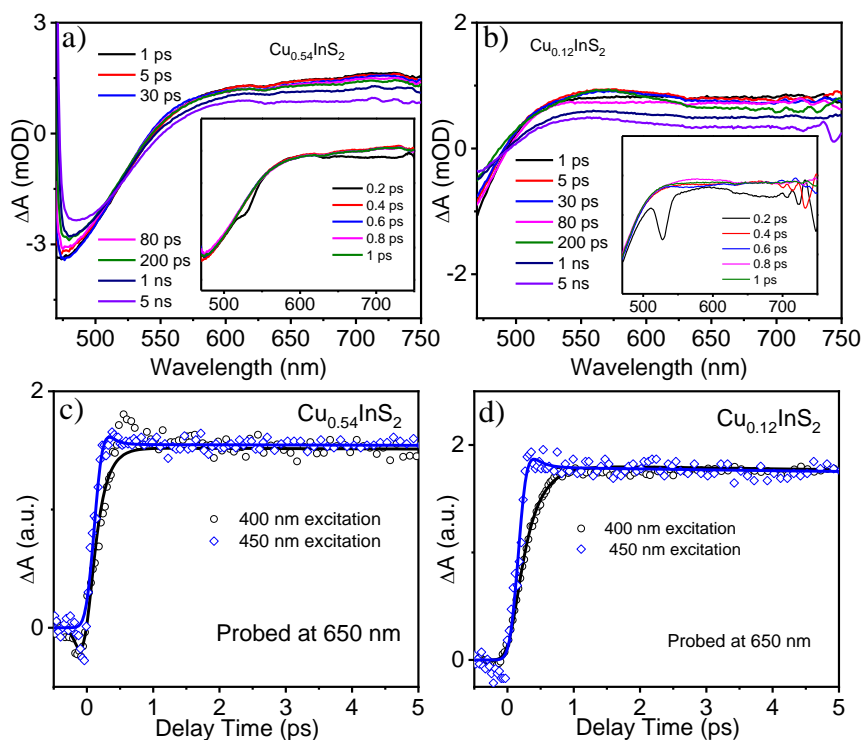


Figure 4-4. The TA spectra of  $\text{Cu}_{0.54}\text{InS}_2$  (a) and  $\text{Cu}_{0.12}\text{InS}_2$  (b) following 450 nm excitation. The inset shows the early time spectra. The comparison of kinetic traces of electron absorption at 650 nm following 400 nm and 450 nm excitation for  $\text{Cu}_{0.54}\text{InS}_2$  (c) and  $\text{Cu}_{0.12}\text{InS}_2$  (d).

To further evaluate the carrier dynamics of these CIS/ZnS QDs, we compared the exciton bleach recovery and the kinetic traces of the electron absorption signals of these samples. The kinetic traces were normalized at later time in order to have a better comparison for the early time kinetics. Due to the small signal of the exciton bleach band as well as the overlap between the exciton bleach and electron absorption signal for  $\text{Cu}_{0.12}\text{InS}_2$ , we are not able to compare its early time spectral evolution for the exciton bleach signal with other samples. Nevertheless, the exciton bleach recovery of  $\text{Cu}_{0.54}\text{InS}_2$ ,  $\text{Cu}_{0.28}\text{InS}_2$  and  $\text{Cu}_{0.17}\text{InS}_2$  becomes faster with increasing Cu deficiency, suggesting that Cu

deficiency can affect the electron-hole recombination process. This appears to conflict with emission lifetime measurement discussed above, where Cu deficiency has negligible impact on the electron-hole recombination time. This discrepancy can be explained by the different time windows those time resolved emission and absorption spectroscopies measure, where the former probes the recombination dynamics at  $> 10$  ns window due to its limited time resolution ( $\sim 10$  ns), while the later measures the early time recombination dynamics at  $< 5$  ns due to the limited time window of our TA spectroscopy. On the other hand, as shown in [Figure 4-5b](#), the kinetic trace of the electron absorption decays slightly faster in the sample with higher Cu deficiency, which is consistent with the exciton bleach recovery. These results can be more clearly seen in the fitting results. As shown in [Figure 4-5](#) and [Table 4-3](#), the kinetic traces of all samples can be fit by a four-exponential decay/rise function. Due to the presence of multiple carrier trapping states and recombination channels in CIS QDs, it is challenging to correlate each time constant with the relaxation pathway. However, according to the time scales of carrier trapping and recombination reported by previous studies,<sup>36, 173, 182</sup> the ultrafast rising/decay component ( $\tau_1$ ) which is close to the instrument resolution limit ( $\sim 0.2$  ps) can be attributed to the electron cooling and/or trapping to the shallow electron trap states;  $\tau_2$  is likely due to the additional carrier trapping by deep-level trap states, and  $\tau_3$  and  $\tau_4$  can be attributed to the recombination of the electrons from these trap states with the holes from the valence band. However, due to the presence of  $\gg 5$  ns

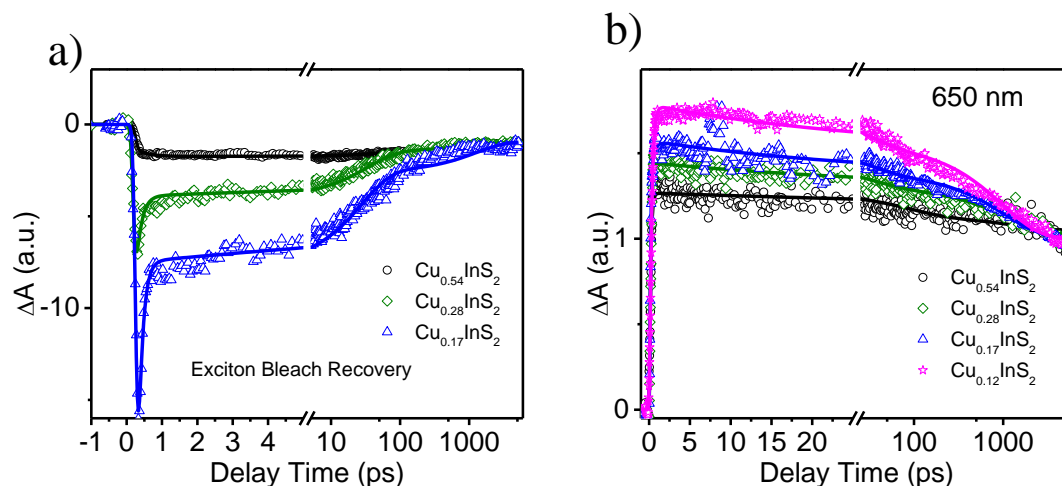


Figure 4-5. (a) The comparison of exciton bleach recovery for  $\text{Cu}_{0.54}\text{InS}_2$ ,  $\text{Cu}_{0.28}\text{InS}_2$ , and (c)  $\text{Cu}_{0.17}\text{InS}_2$ . (b) The comparison of kinetic traces of electron absorption decay of CIS/ZnS QDs at 650 nm with different Cu to In ratios. The excitation wavelength is at 400 nm.

Time constant which is beyond the time window of our TA spectroscopy, we are not able to accurately determine the carrier recombination time. Nevertheless, since  $\tau_2$  and  $\tau_3$  decrease slightly with increasing Cu deficiency, it suggests that recombination process is enhanced slightly in the sample with higher Cu deficiency. To evaluate the correlation of composition of CIS/ZnS QDs with their function for catalysis, we examined the catalytic performance of these samples for  $\text{H}_2$  generation under 405 nm LED irradiation. The sample container is a glass vial with 4 mL reaction solution and 7 mL head space. The reaction solution includes 1 mL ascorbic acid (AA) (pH=5) as the electron donor, 0.1 mL of CIS/ZnS aqueous solution ( $\sim 0.2$  mg CIS/ZnS), and 2.9 mL  $\text{H}_2\text{O}$ . The glass vial was sealed with rubber stopper and purged with  $\text{N}_2$  for at least 10 mins before irradiation. Figure 4-6 shows the amount of  $\text{H}_2$  generated as a function of irradiation time. It can be clearly seen that the  $\text{H}_2$  generation efficiency increases significantly with the increasing Cu deficiency,

Table 4-3. Fitting Parameters for TA kinetics decays of CIS/ZnS with different Cu to In ratios

		$\tau_1$ (ps) (A1)	$\tau_2$ (ps) (A2)	$\tau_3$ (ps) (A3)	$\tau_4$ (ps) (A4)
Bleach signal kinetics	$\text{Cu}_{0.54}\text{InS}_2$	0.35 (18.7) <sup>r</sup>	40.3 (12.54)	1150 (30.13)	> 5000 (58.15)
	$\text{Cu}_{0.28}\text{InS}_2$	0.15 (-66.2)	33.3 (-21.1)	950 (-4.16)	> 5000 (-8.51)
	$\text{Cu}_{0.17}\text{InS}_2$	0.125 (-76.1)	27.3 (-15.3)	851 (-5.21)	> 5000 (-3.34)
650 nm kinetics	$\text{Cu}_{0.54}\text{InS}_2$	0.155 (100) <sup>r</sup>	40.3 (17.53)	1150 (28.64)	> 5000 (53.83)
	$\text{Cu}_{0.28}\text{InS}_2$	0.159 (100) <sup>r</sup>	33.3 (28.29)	950 (31.31)	>5000 (40.4)
	$\text{Cu}_{0.17}\text{InS}_2$	0.21 (100) <sup>r</sup>	27.3 (18.26)	851 (32.52)	> 5000 (49.20)
	$\text{Cu}_{0.12}\text{InS}_2$	0.27 (100) <sup>r</sup>	(21.4)	753 (41.84)	>5000 (36.76)

where the amount of  $\text{H}_2$  generated for  $\text{Cu}_{0.12}\text{InS}_2$  is almost 100 times higher than that of  $\text{Cu}_{0.54}\text{InS}_2$ . In order to have a valid comparison of the  $\text{H}_2$  generation efficiency among different CIS/ZnS QDs to account for the difference of absorbed photons under LED illumination (405 nm), we evaluated the  $\text{H}_2$  generation efficiency in terms of photon-to- $\text{H}_2$  quantum yield according to the method published previously.<sup>22</sup> The obtained photon-to- $\text{H}_2$  quantum yields are  $\ll 1\%$ , 0.7%, 3.8%, and 5.2% for the  $\text{Cu}_{0.54}\text{InS}_2$ ,  $\text{Cu}_{0.28}\text{InS}_2$ ,  $\text{Cu}_{0.17}\text{InS}_2$ , and  $\text{Cu}_{0.12}\text{InS}_2$ , respectively, which increases with increasing Cu deficiency. While higher photon-to- $\text{H}_2$  quantum yields ( $\sim 5 - 20\%$ ) have been reported previously in colloidal photocatalytic systems,<sup>22, 184-187</sup> all of these systems include a cocatalyst that plays a major role in boosting the photocatalytic efficiency. To best of our knowledge, CIS based

photocatalytic systems without cocatalysts show much lower photon-to-H<sub>2</sub> quantum yield ( $\leq 5\%$ ). Indeed, the photon-to-H<sub>2</sub> quantum yield in our system with Cu<sub>0.12</sub>InS<sub>2</sub> (5.2%) is slightly higher than that of previously best-performing system (5%).<sup>188</sup> These results together suggest that the presence of Cu deficiency can significantly enhance the photocatalytic performance of CIS/ZnS QDs and altering the Cu to In ratio is a viable approach to further optimize the photocatalytic performance of CIS/ZnS QDs for HER.

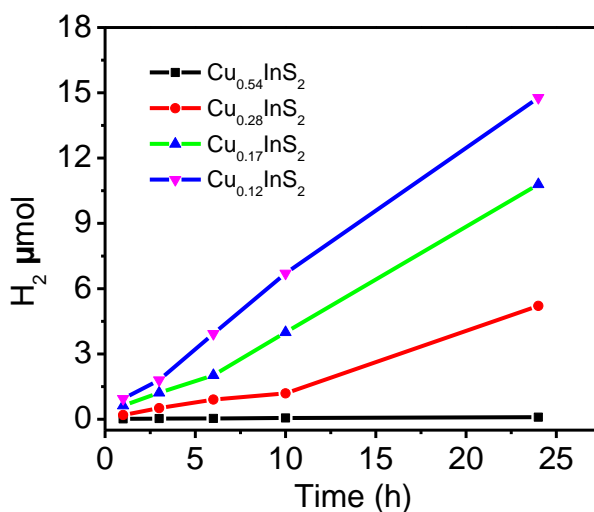


Figure 4-6. H<sub>2</sub> generation time profile of CIS/ZnS QDs with four different Cu to In ratios under 405 nm illumination with 3 mW power. AA is used as the proton source and sacrificial electron donor.

Note that CIS/ZnS QDs with higher Cu deficiency show slightly faster charge recombination but much better photocatalytic activity. This appears to conflict with the commonly accepted model, where elongated electron-hole pair lifetime is beneficial for H<sub>2</sub> generation.<sup>22, 147, 188-189</sup> In order to gain insight into the origin of this conflict, we examined the electron transfer (ET) process from AA to CIS/ZnS QDs, which is another key pathway

that determines the overall efficiency for H<sub>2</sub> generation. Electron transfer from AA to CIS/ZnS QDs was evaluated by measuring the steady state emission quenching of CIS/ZnS QDs as a function of AA concentration followed by Stern-Volmer analysis. As shown in Figure 4-7, we found that the ET rate constants are  $0.58 \times 10^8 \text{ M}^{-1} \text{ S}^{-1}$ ,  $1.02 \times 10^8 \text{ M}^{-1} \text{ S}^{-1}$ ,  $1.77 \times 10^8 \text{ M}^{-1} \text{ S}^{-1}$ , and  $2.74 \times 10^8 \text{ M}^{-1} \text{ S}^{-1}$  for QDs with Cu<sub>0.54</sub>InS<sub>2</sub>, Cu<sub>0.28</sub>InS<sub>2</sub>, Cu<sub>0.17</sub>InS<sub>2</sub>, and Cu<sub>0.12</sub>InS<sub>2</sub>, respectively, which increases considerably with increasing Cu deficiency,

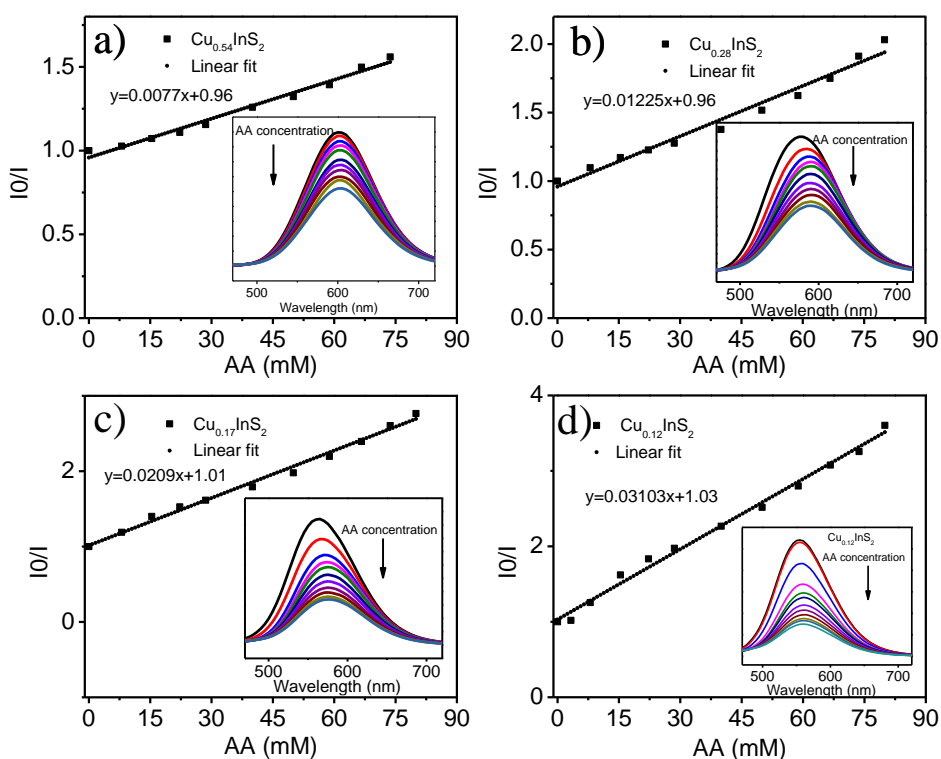


Figure 4-7 Stern-Volmer plots of prepared CIS/ZnS QDs: a) Cu<sub>0.54</sub>InS<sub>2</sub>; b) Cu<sub>0.28</sub>InS<sub>2</sub>; c) Cu<sub>0.17</sub>InS<sub>2</sub> and d) Cu<sub>0.12</sub>InS<sub>2</sub> inset: the emission spectra of prepared CIS/ZnS QDs in the presence of different concentrations of AA.

following the same trend as their photocatalytic performance. Combining the results from the carrier dynamics of CIS/ZnS QDs measured by TA spectroscopy, emission quenching

experiment, and their photocatalytic performance for H<sub>2</sub> generation, we believe that ET from AA to CIS/ZnS QDs plays an important role in overall charge separation and catalytic activity for H<sub>2</sub> generation, where faster ET process in the sample with higher Cu deficiency results in more efficient overall charge separation and thus significantly enhanced photocatalytic performance. The faster ET in CIS/ZnS QDs with higher Cu deficiency may result from their lower valence band, which leads to larger driving force for ET to occur from AA to CIS/ZnS QDs.

### **4.3 Conclusion**

In summary, we report the dependence of carrier and charge separation dynamics of CIS/ZnS QDs and their photocatalytic performance for light driven hydrogen generation on the cation composition (i.e. Cu to In ratio). With increasing Cu deficiency (decreasing Cu to In ratio), we show that the electron-hole pair recombination in CIS/ZnS QDs measured by TA spectroscopy are a little faster while the photocatalytic activities for H<sub>2</sub> generation are significantly improved. This can be explained by the notably enhanced ET from AA to CIS/ZnS QDs resulting from the lower valence band edge of QDs (larger driving force for ET) for samples with higher Cu deficiency, which facilitates overall charge separation. This work suggests that altering the cation composition in CIS/ZnS QDs is a viable approach to further improve their photocatalytic performance for solar to fuel conversion.

## Chapter 5

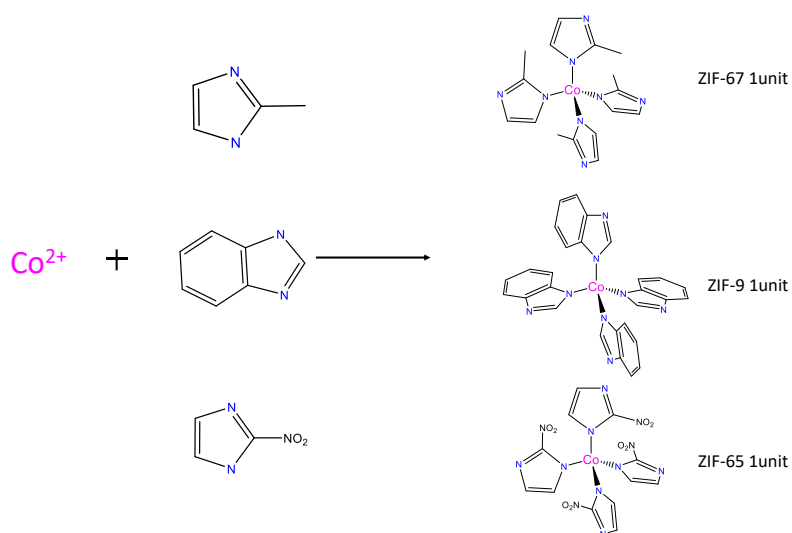
### The Impact of Coordination Ligand on Electronic Structure and Photophysical properties of Zeolitic imidazolate Frameworks (ZIFs)

#### 5.1 Introduction

Zeolitic imidazolate frameworks (ZIFs) are a subclass of metal organic frameworks (MOFs),<sup>190-194</sup> which are composed of divalent transition metal nodes (such as Zn<sup>2+</sup> and Co<sup>2+</sup>) tetrahedrally coordinated by imidazole-based organic linkers.<sup>52-53, 57, 195-196</sup> Owing to their unique properties such as high porosity, large surface area, and structural diversity,<sup>126, 194, 197-199</sup> ZIFs have demonstrated a wide range of applications in gas storage and separation,<sup>199-201</sup> catalysis,<sup>117, 202-204</sup> sensing,<sup>73</sup> as well as being used as template to synthesize mesoporous materials.<sup>205-207</sup> Moreover, our recent efforts on examining ZIF-67 synthesized from Co(NO<sub>3</sub>)<sub>2</sub> and 2-methyl imidazolate showed that ZIF-67 not only possess broad absorption in UV-visible-near IR region but also exhibit a long-lived ES (2.9 us lifetime) with charge separation (CS) character.<sup>95, 113</sup> Subsequent study showed that the electron in this CS state can be extracted and used for photocatalytic reactions in the presence of molecular photosensitizers, demonstrating that ZIFs have intrinsic light harvesting and CS properties that can be used for photocatalytic applications.

While these findings demonstrate the great promise of ZIFs as light harvesting and photocatalytic materials, to further facilitate the optimal design of ZIFs for photocatalytic applications, it is essential to develop an in-depth understanding of the direct correlation of ZIF structure with their photophysical properties that are central to their function for photocatalysis. It has been found that ZIFs with different imidazole linkers not only give rise to different topology but also pore structure and size, which impacts gas storage and

separation.<sup>208-210</sup> In addition, previous experimental and theoretical studies have shown that the inclusion of different functional groups in imidazolate ligands can readily tune the redox potentials,<sup>211-212</sup> conductivity,<sup>108</sup> and optical excitation gaps.<sup>112</sup> Inspired by these prior work, herein I investigated the systematic studies on the impact of the imidazolate structure on the photophysical properties of three Co based ZIFs, i.e. ZIF-67, ZIF-9 and ZIF-65, which are synthesized from  $\text{Co}(\text{NO}_3)_2$  and 2-methylimidazole (2mIm), benzimidazole (bIm) and 2-nitroimidazole (2nIm), respectively (Scheme 1). The UV-Visible-NIR spectra show the difference of Co d-d transition caused by the ligand effect. The CASSCF (complete active space self-consistent field theory) calculation confirms that the Mulliken charge on Co center increased from ZIF-67, ZIF-9 to ZIF-65. The 2nIm also cause the split of Co  $^4\text{T}$  state which results in the shift and broad UV-Visible-NIR spectra of ZIF-65 compared to ZIF-67. Femtosecond transient absorption spectra results exhibit that the electron withdraw ability of the ligand can affect the formation of the intermediate state after excitation.



Scheme 5-1. One unit of Cobalt based Zeolitic imidazolate Frameworks (ZIFs)

## 5.2 Results and discussion

The formation of ZIF-67, ZIF-9 and ZIF-65 is confirmed by X-ray diffraction (XRD), X-ray absorption spectroscopy (XAS), and diffuse reflectance (DR) spectroscopy. As shown in Figure 5-1a, the XRD patterns of ZIF-67, ZIF-9 and ZIF-65 exhibit the typical patterns that belong to SOD topology.<sup>125-126, 213</sup> The scanning electron microscope (SEM) images of ZIF-67, ZIF-9 and ZIF-65 are shown in Figure 5-2, which are consistent with the report results. The local geometry at Co center in ZIFs was measured by X-ray absorption spectroscopy (XAS). As shown in Figure 5-1b, the X-ray absorption near edge structure (XANES) spectra at Co edge of ZIF-67, ZIF-9 and ZIF-65 all exhibit distinct pre-edge feature at  $\sim 7709$  eV which corresponds to the dipole forbidden but quadrupole allowed  $1s$  to  $3d$  transition. This is consistent with the tetrahedral geometry of Co center, where the broken central symmetry of Co results into the wavefunction mixing of  $4p$  and  $3d$  orbitals and effectively facilitates transition from  $1s$  to  $3d$  orbital with  $4p$  character.<sup>214</sup>

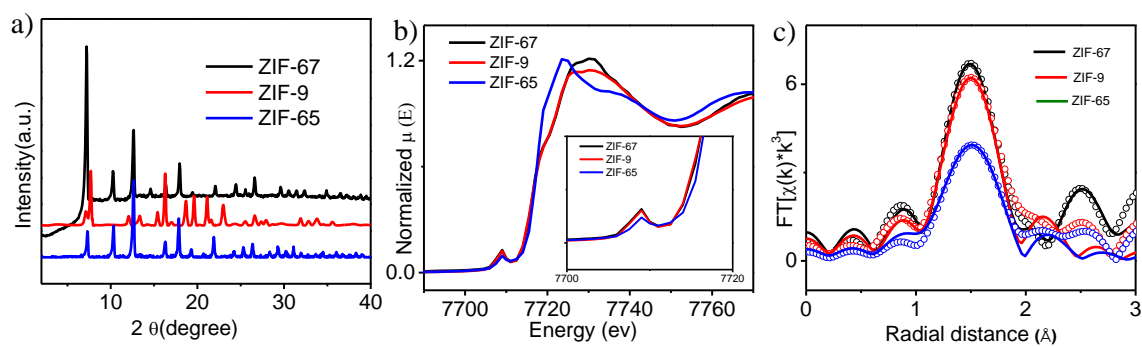


Figure 5-1 XRD (a), X-ray absorption near edge structure spectra (b) and fourier transformed extended X-ray absorption fine structure (EXAFS) spectra (c) of prepared ZIFs

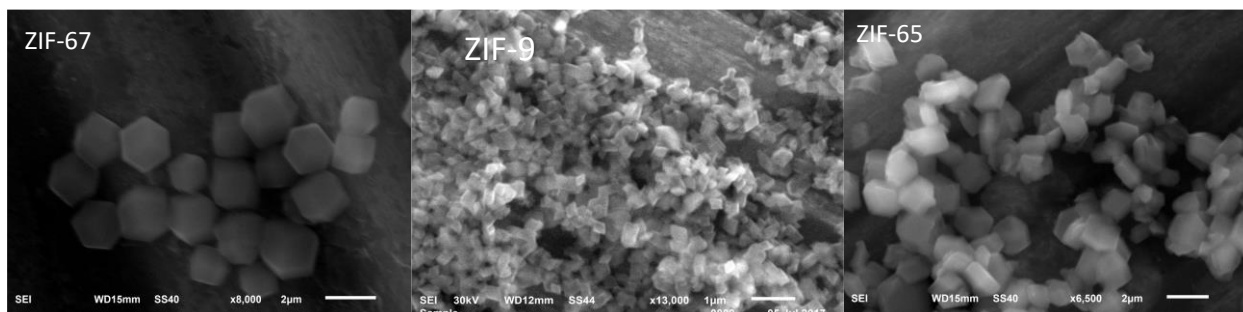


Figure 5-2 SEM images of prepared ZIFs

The intensity of these pre-edge peaks decrease in the order of ZIF-67, ZIF-9, and ZIF-65, i.e. increasing electron withdrawing ability of the ligand ( $2\text{mlm} < \text{blm} < 2\text{nlm}$ ). This suggests that the ligand with stronger withdrawing group may slightly reduce the overlap of 3d and 4p orbitals and thus prohibit the 1s-3d transition of the Co center.<sup>215-216</sup> On the other hand, the XANES spectra of both ZIF-67 and ZIF-9 show the prominent 1s-4p and shakedown transitions while the shakedown transition in ZIF-65 can be rarely observed. As the shakedown transition reflects ligand to metal charge transfer (LMCT), it suggests that the stronger electron withdrawn ability of the ligand may prevent the ligand-to-metal charge transfer (LMCT) transition. Figure 5-1c shows the fourier transformed extended X-ray absorption fine structure (EXAFS) spectra of these ZIF samples. The first shell peak which represents the Co-N bond does not shift among three samples, suggesting similar Co-N distance. The amplitude of this peak decreases with the increase of electron withdrawing ability of the ligands. The smaller amplitude may be attributed to either the decrease of the coordination number or the increase of debye waller factor ( $\sigma^2$ ) resulting from disorder. As the coordination number of Co center in these ZIFs is 4 (discussed later), it suggests that stronger electron withdrawing group results in larger disorder around Co

center. This agrees with the reduced overlap of 3d and 4p orbitals observed in XANES results, which may result from the increased disorder among Co-ligand bonds. To get further information about the local structure of Co center, EXAFS data were fit using Artemis in Demeter software package. The fitting results are shown in Figure 5-1c and the fitting parameters are listed in Table 5-1. All the ZIFs show four coordination, which is consistent with the tetrahedral Co center. ZIF-65 has much larger  $\sigma^2$  compared to ZIF-67 and ZIF-9, indicating that the Co-N bond distance in ZIF-65 is less uniform than that in ZIF-67 and ZIF-9. All of these results together suggest that the electron withdrawing group in the ligands has apparent impact on the electronic structure of ZIFs, where the stronger electron withdrawing ability of the ligands leads to the reduced overlap of 3d and 4p orbitals, less LMCT character, and larger bond disorder.

Figure 5-3a shows the steady state absorption spectra of these different ZIFs. All three ZIFs exhibit the typical Co d-d transition in the visible and near IR region, which have been assigned to  ${}^4A_2(F) \rightarrow {}^4T_1(P)$  and  ${}^4A_2(F) \rightarrow {}^4T_1(F)$ , respectively.<sup>96, 217</sup> In the near IR region, the absorption peak of the ZIFs shows slightly blue shift with increasing electron withdrawing ability of the ligand, i.e.  $2mlm < blm < 2nlm$ . In the visible region, ZIF-65 shows absorption peak at 552 nm while ZIF-67 and ZIF-9 show absorption centered at similar position (588 nm). The impact of the ligands on the absorption properties of ZIFs is further examined using density functional theory (DFT) and CASSCF (complete active space self-consistent field theory), where the former is applied to the ligand molecule and the latter is applied to the single unit ZIF structure. The calculation results are shown in Figure 5-3b, Table 5-2 and Table 5-3. The calculated spin allowed Co d-d transitions of ZIFs with different ligand

are shown in Figure 5-3b. As we can see, the transition in 400 ~600 nm region show blue shift which is consistent with the experimental results. In NIR region, the three transition

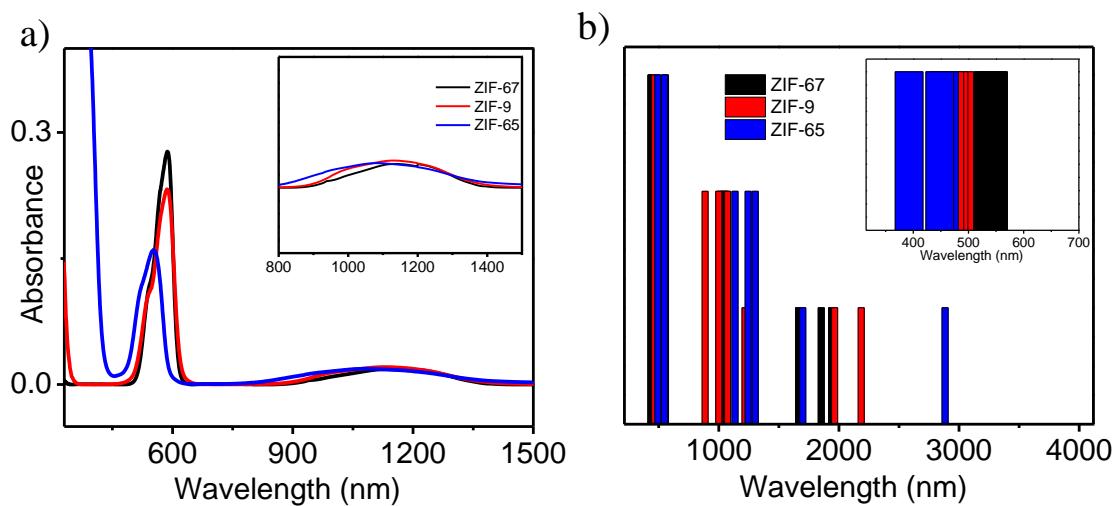


Figure 5-3 (a) UV-vis-NIR diffuse reflectance spectra of ZIFs (b) Calculated transitions in ZIFs.

states of shows similar energy while the states of ZIF-9 and ZIF-65 varies a lot, confirming the broader absorption spectra of ZIF-9 and ZIF-65 in NIR region. Table 5-1 lists the Mulliken charges on N center of each imidazole linker while Table 5-2 lists the Mulliken charges of each ZIF on Co center. The results show that the N atom on 2mIm have much more negative charges than that of bIm and 2nIm while the Co center in ZIF-67 have less positive charges compared to ZIF-9 and ZIF-65, indicating the electron withdrawn group can cause the decrease of electron density around Co center.

Table 5-1 Mulliken charges on N center in different imidazole

	2mIm	bIm	2nIm	Im
N1	-0.025302	-0.020756	-0.114322	-0.043175
N2	-0.163038	-0.128903	-0.081276	-0.165759

Table 5-2 Mulliken charges on Co center in 1 unit of ZIF

	ZIF-67	ZIF-9	ZIF-65
Co	1.26	1.28	1.29

To further understand the impact of ligands on the photophysical properties of ZIFs, we measured the ES dynamics using optical transient absorption (OTA) spectroscopy following 1200 nm excitation which directly excite the lower lying d-d transition. We only collected the OTA spectra of ZIF-67 and ZIF-9 because ZIF-65 results no OTA signal which may be due to the low extinction coefficient at 1200 nm or very fast charge recombination rate which is beyond our laser resolution. As shown in Figure 5-4, both OTA spectra of ZIF-67 and ZIF-9 exhibit the immediately formed ground state bleach (GSB) for Co d-d transition. This is followed by the formation of the positive feature a

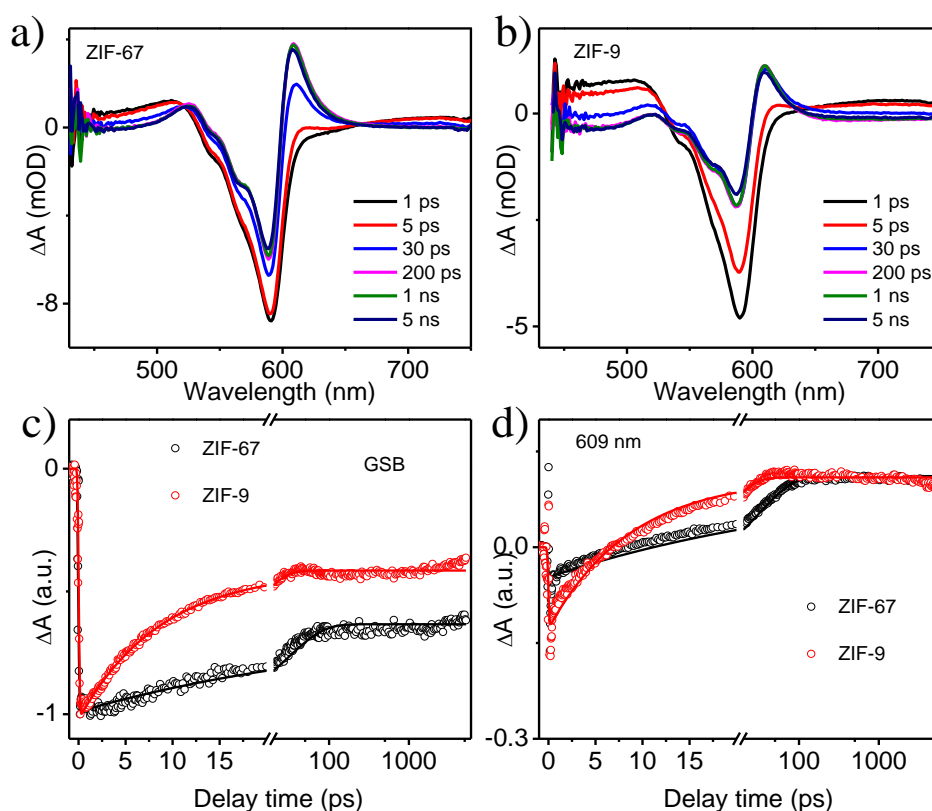


Figure 5-4. Femtosecond transient absorption (TA) spectra of ZIFs under 1200 nm excitation: a) ZIF-67 and b) ZIF-9; Kinetics traces of ground bleach feature recovery (GSB) (c) and charge separation state at 609 nm (d).

606 nm corresponding to the long-lived CS, which is similar to the OTA results of ZIF-67 published earlier. The intensity of the CS feature of ZIF-9 is much lower than that of ZIF-67, which further tells that the electron withdrawing linker can impede the formation of the photogenerated CS even with direct excitation of Co d-d transition. Both bleach recovery kinetics (Figure 5-4c) and CS decay kinetics (Figure 5-4d) show that ZIF-9 shows much faster kinetics, indicating that the ligand can affect the charge recombination rate in ZIFs after photoexcitation. The kinetic traces fitting results were listed in Table 5-3, the rising

time (8.7 ps) ZIF-9 at 609 nm is much shorter than that in ZIF-67 (31.7 ps), also indicating faster charge transfer in ZIF-9.

Table 5-3 Fitting time constants of TA kinetics under 1200 nm excitation.

		$\tau_1$	$\tau_2$
ZIF-67	588 nm	31.7 ps	> 5 ns
	609 nm	31.7 ps	> 5 ns
ZIF-9	588 nm	8.7 ps	> 5 ns
	609 nm	8.7 ps	> 5 ns

To further understand the impact of the ligands on the photophysical properties of these ZIFs, OTA spectra were collected under 350 nm excitation. As shown in XANES results, the different ligands in ZIFs can affect the LMCT transition. As a result, we collected the OTA spectra of ZIFs by selectively exciting the LMCT and Co d-d transitions. Figure 5-5 a-c show the OTA spectra of ZIF-67, ZIF-9 and ZIF-65, respectively, following the excitation of 350 nm corresponding to LMCT transition. Immediately following the excitation, the early time OTA spectra (inset of Figure 4) show broad positive feature which can be assigned to the LMCT excited state (ES) absorption. These TA spectra also show a transient dipped signal at ~ 586 nm. This feature occurs at the same wavelength as the Co  $^4A_2(F) \rightarrow ^4T_1(P)$  transition and can thus be attributed to the ground state bleach (GSB) of Co d-d transition, consistent with our previous results. The whole spectra decay with time to form the negative feature at 586 nm, which further supports our assignment of GSB of Co d-d transition. In addition, in the TA spectra of ZIF-67, a new positive feature at 606 nm,

which has been assigned to the intermediate charge separated (CS) state of ZIF-67, forms simultaneously with the decay of the positive signals in the whole TA spectrum. The presence of two isosbestic points at 598 nm and 626 nm and negligible recovery of these spectral features support that the spectral evolution corresponds to the same relaxation process, i.e. conversion from the initial LMCT ES to form the long-lived CS state. The TA spectra of ZIF-9 and ZIF-65 also show the formation of GSB of Co d-d transition. However, the evolution of GSB and the positive signal at 606 nm is much less prominent compared to that of ZIF-67. Nevertheless, by the delay time of 5 ns, the spectral evolution leads to the formation of the derivative feature that has similar shape as ZIF-67 but much lower intensity. These results together suggest that all three ZIFs show the formation of the long-lived CS state but the relaxation from LMCT to CS is less prominent in ZIF with stronger electron withdrawing ligand.

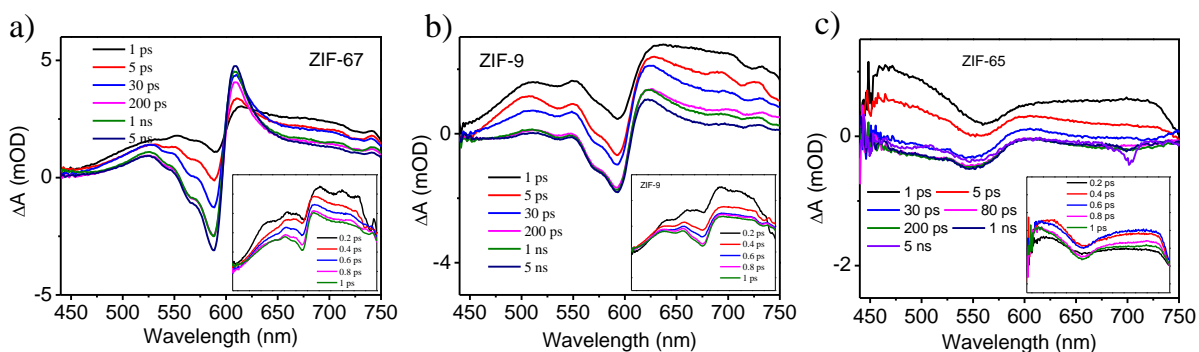


Figure 5-5 Femtosecond transient absorption (TA) spectra of ZIFs under 350 nm excitation: a) ZIF-67; b) ZIF-9 and c) ZIF-65, Inset: early time TA spectra of each sample.

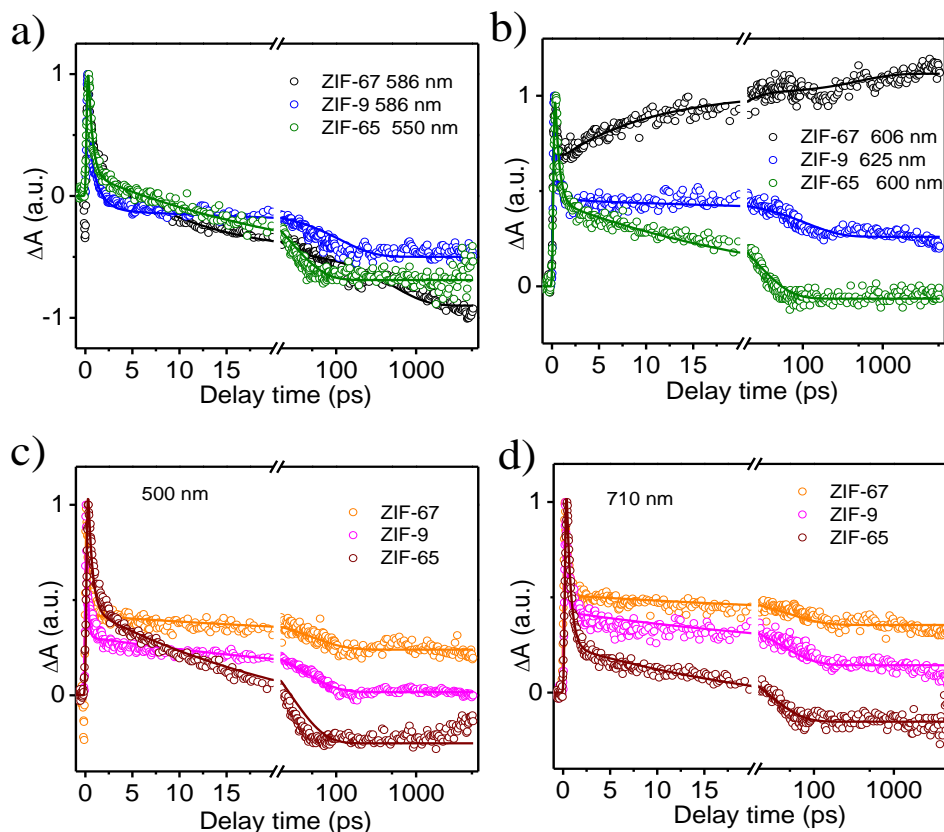


Figure 5-6 Kinetics traces of ZIFs at different wavelength under 350 nm excitation.

In order to understand the photophysical dynamics of ZIFs after being excited at 350 nm light, the kinetics at different wavelength were compared Figure 5-6. Figure 5-6a and Figure 5-6b displayed the GSB and long-lived CS kinetic traces of the obtained ZIFs, respectively. The GSB recovery kinetics show negligible difference among the three ZIFs while the long-lived CS kinetics of ZIF-67 exhibited much slower decay compared to that of ZIF-9 and ZIF-65, which further support that the electron donating ligand is helpful for the formation of long-lived CS. The kinetic traces at 500 nm and 710 nm related to the LMCT ES absorption were shown in Figure 5-6c and Figure 5-6d respectively. The LMCT ES of ZIF-67 showed the slowest while that of ZIF-65 has the fastest decay in our OTA

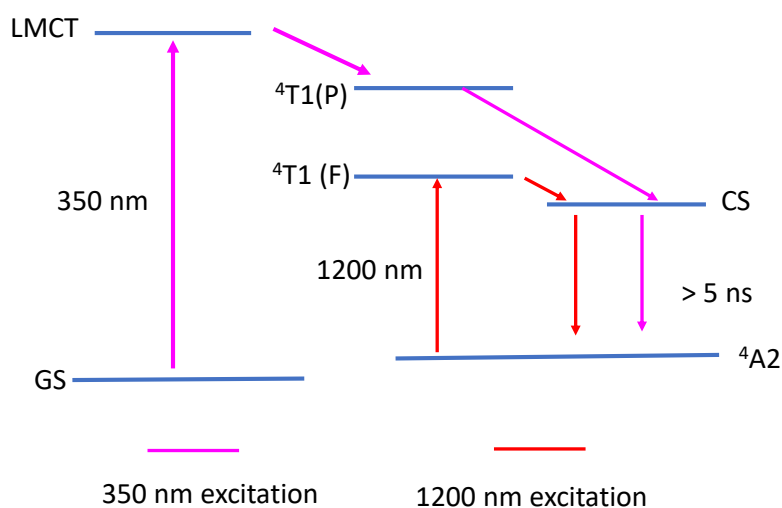
time window. Both long-lived CS and LMCT ES kinetic decays confirmed that the electron withdrawing ability of the ligand can affect the photodynamics of ZIFs. ZIFs based on the ligand with stronger electron withdrawing ability show less prominent CS and faster decay of LMCT ES.

In order to understand the photophysical dynamics in detail, the kinetic traces were fitted with exponential function with the same time constants for each ZIF sample. The fitting results of 350 nm excitation were shown in Figure 5-6 and Table 5-4. As listed in Table 5-4, the Co d-d transition bleach feature and long-lived CS in ZIF-67 and ZIF-9 kinetic traces showed different fitting results compared to the traces at 500 nm and 710 nm while the kinetic traces in ZIF-65 can be fitted with the same time constant for all four wavelengths. In ZIF-67, the kinetics at 586 nm and 606 first exhibited fast decay with 0.27 ps time constant then two rising components with time constant 9.7 ps and 740 ps. As mentioned earlier, the spectral evolution in ZIF-67 consists of the same relaxation process, i.e. the two rising components corresponds to the formation of  $^4T_1(F)$  excited state and long-lived CS. In ZIF-9, the fast decay time constant is 0.15 ps, and the formation of Co  $^4T_1(F)$  excited state and long-lived CS time constants were much shorter than that of ZIF-67. Due to the overlap of the decay of LMCT ES and the formation of Co  $^4T_1(F)$  excited state, the kinetics at 586 nm in ZIF-9 did not show the rising time constant in the fitting results. However, the formation of Co  $^4T_1(F)$  excited state and long-lived CS time was observed, where the time constants are 2.94 ps and 111 ps, respectively, which are much shorter compared to ZIF-67. The LMCT ES decay time constant (39.1 ps) is also shorter. In ZIF-65, all four wavelengths showed similar relaxation process. The missing

components of the formation of Co  $^4T_1(F)$  excited state and long-lived CS may due to the effect of the strong electron withdraw ability of the ligand.

Table 5-4. Kinetics fitting results of ZIFs under 350 nm excitation.

		$\tau_1$ ps (A1)	$\tau_2$ ps (A2)	$\tau_3$ ps (A3)	$\tau_4$ ns (A4)
ZIF-67	586 nm	0.27 (0.413)	10.8 (0.21 r)	740 (0.121 r)	> 5 (- 0.256)
	606 nm	0.27 (0.328)	9.73 (-0.157r)	513 (-0.0428 r)	> 5 (0.47.3)
	500 nm	0.27 (72.9)	49.3 (11.2)		> 5 (15.9)
	710 nm	0.27 (67.1)	49.3 (9.86)		> 5 (23)
ZIF-9	586 nm	0.15 (0.698)	2.94 (0.0958)	111 (0.079)	> 5 (-0.128)
	625 nm	0.15 (0.819)	2.94 (0.0156)	111 (0.0753)	> 5 (0.0901)
	500 nm	0.15 (0.868)	39.1 (0.124)		> 5 (0.007)
	710 nm	0.15 (0.851)	39.1 (0.0986)		> 5 (0.05)
	550 nm	0.442 (0.461)	26.2 (0.301)		> 5 (-0.238)
	600 nm	0.442 (0.605)	26.2 (0.3521)		> 5 (-0.0442)
	500 nm	0.442 (0.506)	26.2 (0.364)		> 5 (-0.13)
	710 nm	0.442 (0.698)	26.2 (0.218)		> 5 (-0.0837)



Scheme 5-1 energy diagram of ZIFs after photoexcitation

As illustrated in scheme 5-1, the LMCT band was excited with 350 nm excitation followed by the quick relaxation to higher-lying Co II tetrahedral excited state, followed by the long-lived charge separation state. The lower-lying excited Co II excited state ( $^4T_1$  (F)) was formed by 1200 nm excitation. After a rising period, 31.7 ps in ZIF-67 and 8.7 ps in ZIF-9, the long-lived charge separation state formed. The results of the OTA spectra under 350 nm excitation and 1200 nm excitation suggest that the imidazole linker with different functional group can affect the photophysical properties of ZIFs. Imidazole with electron donating group like methyl group can help ZIF to form and stabilize the long-lived CS after photoexcitation. In contrast, imidazole with electron withdrawing group like nitro group can block the LMCT transition and hind the formation of CS in ZIF after photoexcitation. The XAS results also showed the missing of shakedown transition in ZIF-9, confirming the block of LMCT transition.

### 5.3 Conclusion

In this project, we synthesized Co-based ZIFs with three different ligands. The XRD results match the reported works. The XAS results confirmed the tetrahedral geometry of Co center in ZIFs and the missing of shakedown transition in ZIF-65 indicating the hard LMCT in ZIF-65. The CASSCF calculation results showed the blue shift of Co d-d transition which is consistent with the experimental results. The OTA results showed that ZIF with electron donating group on imidazole ring can form long-lived CS after photoexcitation. Different imidazole ligand exhibited different photophysical dynamic results. The charge recombination in ZIF-67 is much slower than that of ZIF-9 and ZIF-65.

## Chapter 6

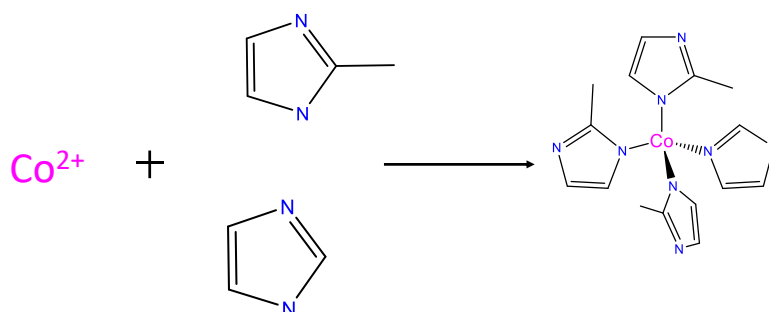
### Enhanced ZIF-67 Photocatalytic Hydrogen Generation Efficiency of ZIF-67 due to Imidazole Doping

#### 6.1 Introduction

As reported in our previous works, ZIF-67 can be used as an efficient photocatalyst for light-driven hydrogen generation using either  $\text{Ru}(\text{bpy})_3\text{Cl}_2$  or  $\text{RuN}_3$  as the photosensitizer.<sup>117, 124</sup> However, in the reported two systems, the hydrogen generation efficiency was increased through the optimization of the photocatalytic condition and showed negligible attention on the modification of ZIF-67 or enhancing the communication between ZIF-67 and photosensitizer. Grau-Crespo and co-workers predicted the HOMO and LUMO of ZIFs based on various imidazolate ligands and pointed out that the mixed ligands in the ZIFs structure have a strong effect on HOMO and LUMO which may affect the driving force of solar-driven hydrogen generation. Imidazole, the simplest imidazole linker in ZIFs family, has been used a lot in the synthesis of mixed-linker ZIFs, which can affect the gas storage and separation properties. Inspired by these works, doping a second imidazole linker into ZIF-67 was designed to study how the doped linker affect the photocatalytic hydrogen generation reaction.

In this project, small amount of parent imidazole (Im) was introduced into ZIF-67 structure to study the effect of imidazole on the photocatalytic hydrogen generation property of ZIF-67. Scheme 6-1 illustrated the synthetic process of introducing imidazole into ZIF-67 structure. The doping amount of Im varied from the molar percentage in total imidazole linker during the synthesis process which has been shown chapter 2. The photocatalytic hydrogen generation efficiency of imidazole doped ZIF-67 was investigated

with  $\text{Ru}(\text{bpy})_3\text{Cl}_2$  as the photosensitizer under the reported optimized condition and turned out that the hydrogen generation efficiency increased when Im was introduced into ZIF-67 structure. The optical transient absorption spectroscopy results showed faster electron from  $\text{Ru}(\text{bpy})_3\text{Cl}_2$  to Im-ZIF-67 which explained the higher hydrogen generation efficiency of Im-ZIF-67.



Scheme 6-1 illustration of introducing imidazole into ZIF-67

## 6.2 Results and discussion

To confirm the structure of imidazole doped ZIF-67, powder X-ray diffraction (XRD) patterns were collected and shown in Figure 6-1a. Compared to ZIF-67, all the imidazole doped ZIF-67 showed the same XRD patterns, which is consistent with the reported result,<sup>213</sup> indicating the doping of Im replaced 2mIm and didn't cause the change of crystalline structure and topology of ZIF-67. The local structure of ZIF-67 and Im doped ZIF-67 was studied by steady state X-ray absorption spectroscopy shown in Figure 6-1b. The ZIF-67 based samples showed almost the same X-ray absorption near edge structure (XANES) spectra, the same pre-edge feature, 1s to 4p transition, indicating the doping of

Im didn't cause changes to Co coordination environment. SEM images (Figure 6-2) showed the same morphology and size of all the ZIF-67 based samples, suggesting that the doping of Im didn't cause changes to morphology. The percentage of Im in final ZIF samples was measurement by NMR with reported method<sup>218</sup> and listed in Table 6-1.

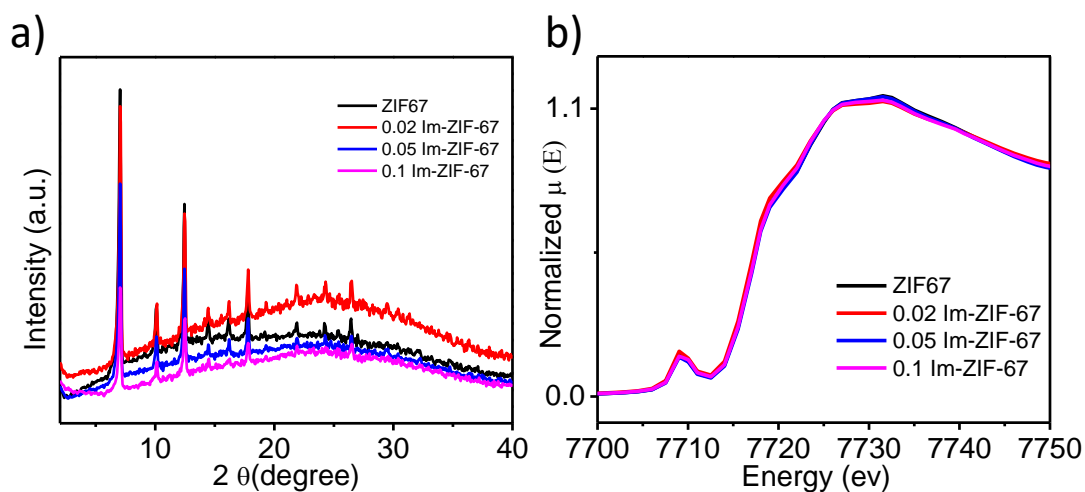


Figure 6-1 a) XRD patterns of ZIF-67 and Im doped ZIF-67; b) X-ray absorption near edge structure of ZIF-67 based samples.

In order to study the optical properties of the Im doped ZIF-67 samples, the UV-visible absorption spectra were collected and shown in Figure 6-3, which were consistent with the reported UV-visible spectrum of ZIF-67.<sup>95, 113</sup> Compared to ZIF-67, the spectra of Im doped ZIF-67 showed almost no difference. To further study the effect of Im on the optical

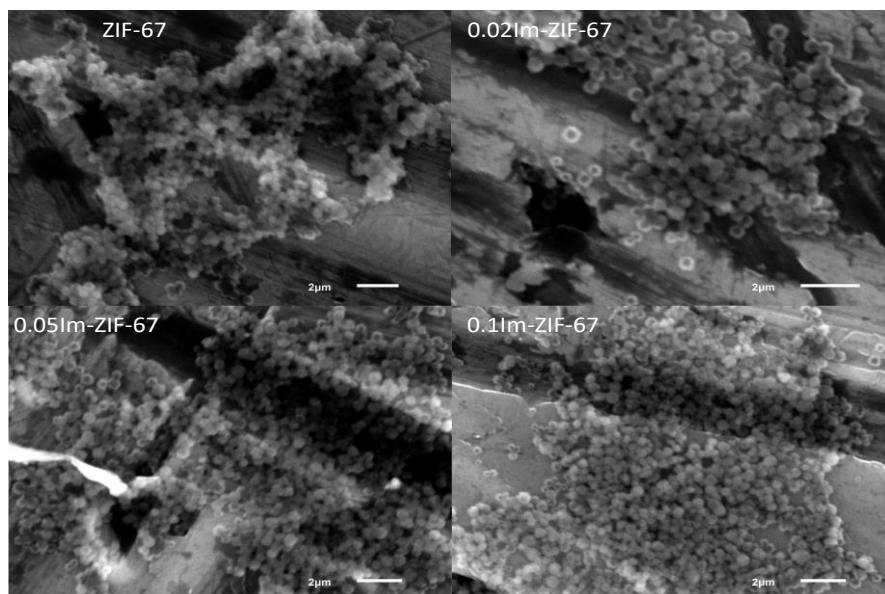


Figure 6-2 SEM images of ZIF-67 and Im doped ZIF-67

Table 6-1. the percentage of Im in starting materials and final products.

Im percentage	Starting	Final
0.02Im-ZIF-67	2%	7%
0.05Im-ZIF-67	5%	15%
0.1Im-ZIF-67	10%	21%

properties of ZIF-67, femtosecond transient absorption spectrum was collected and the results were shown in Figure 6-4. Typically, all the Im doped ZIF-67 samples showed the similar TA features to ZIF-67, ground state bleach (GSB) around 590 nm and charge

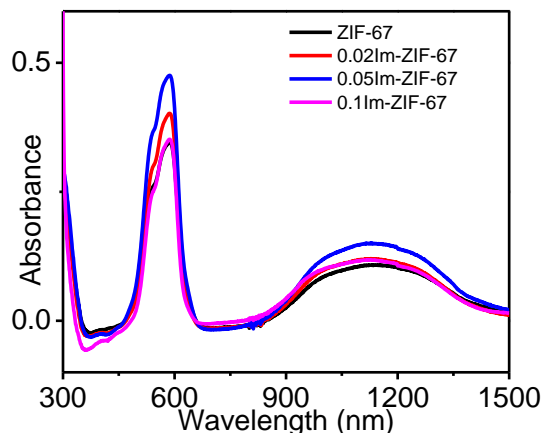


Figure 6-3 UV-visible diffuse reflectance spectra of ZIF-67 based samples.

separation (CS) state around 610 nm, which are consistent with previous reported results,<sup>95</sup> while the only small difference was the rising of the charge separate state. To compare the small difference, the OTA spectra of ZIF-67 based samples at 1 ps and 5 ns are plotted in Figure 6-4e and 6-4f respectively, which were normalized at 590 nm. Both 1 ps and 5 ns spectra showed enhanced CS state intensity in Im doped ZIF-67, especially in 0.05Im-ZIF-67, indicating that the doped Im in ZIF-67 structure can affect the formation of CS state. To further investigate the formation of the CS state, the plotted kinetics traces of all the samples for GSB recovery and CS state decay were shown in Figure 6-5a and Figure 6-5b, respectively. The results showed that the GSB recovery showed almost no difference while the CS state decay showed faster rising in early time of Im doped ZIF-67 with fastest rising in 0.05Im-ZIF-67, indicating the doped Im in ZIF-67 structure can facilitate the formation of CS state.

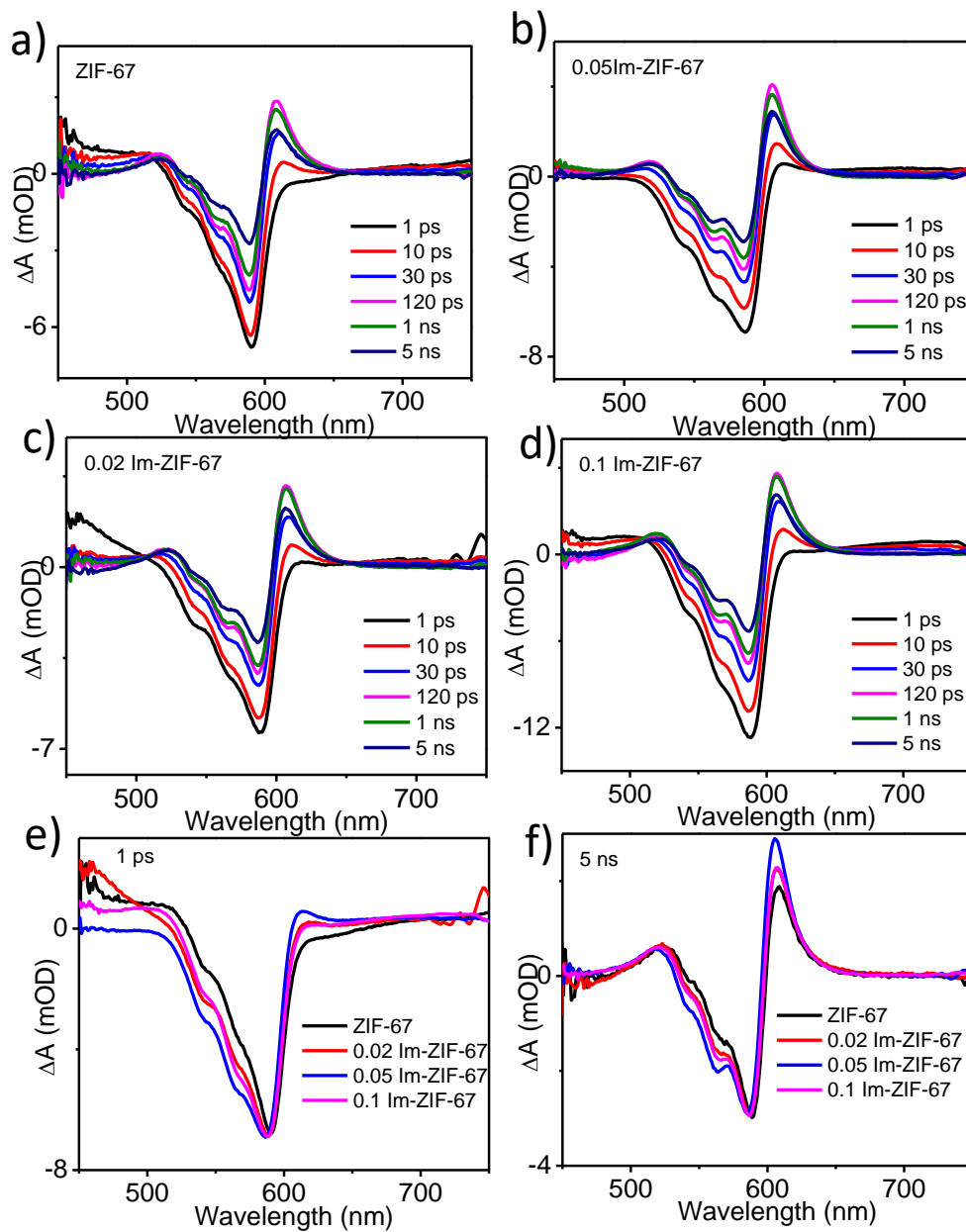


Figure 6-4 Femtosecond transient absorption spectra of ZIF-67 (a), 0.02Im-ZIF-67(b), 0.05Im-ZIF-67 (c) and (d) 0.1Im-ZIF-67 under 1200nm excitation; The comparison of TA spectra at 1 ps (e) and 5 ns (f).

As the TA results showed that the Im can affect the formation of CS state which is related to the photocatalytic performance, thus, the photocatalytic hydrogen generation efficiency

of Im doped ZIF-67 samples were investigated under 450 nm LED illumination. In this photocatalysis system,  $\text{Ru}(\text{bpy})_3^{2+}$  was used as the photosensitizer while TEOA was used as the sacrificial donor.<sup>117</sup> The results of hydrogen generation efficiency with 20 h  $\text{H}_2$  accumulation of ZIF-67 based samples were shown in Figure 6-6. As we can see, the hydrogen generation efficiency increased with the increasing amount of Im in ZIF-67 structure and reached the highest efficiency for 0.05Im-ZIF-67 sample. Compared to ZIF-67, the hydrogen generation efficiency of 0.05Im-ZIF-67 increased almost 50%.

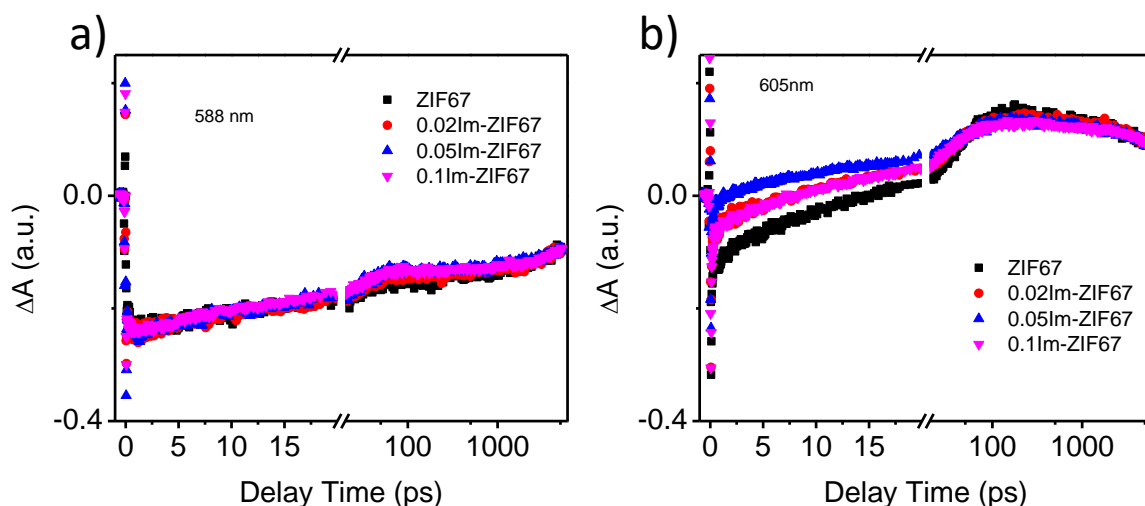
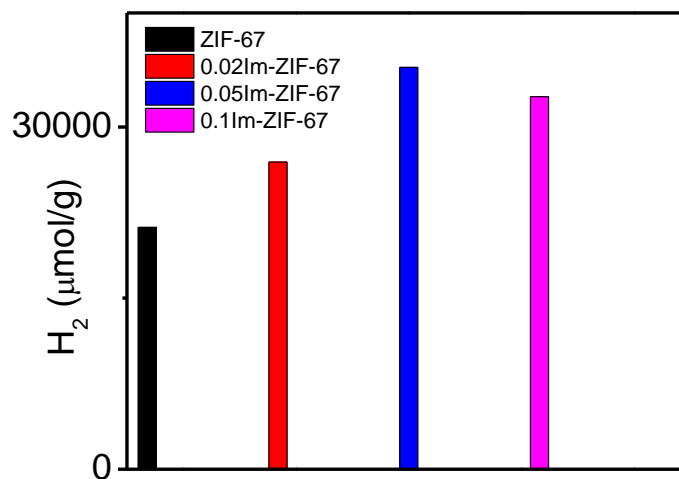


Figure 6-5 kinetic traces of ZIF-67 based samples under 1200 nm excitation.

To figure out the reason why Im doped ZIF-67 have a higher hydrogen generation efficiency, transient absorption of  $\text{Ru}(\text{bpy})_3^{2+}$  on different Im doped ZIF-67 were performed under 430 nm excitation and shown in Figure 6-7. The TA spectra of  $\text{Ru}(\text{bpy})_3^{2+}/\text{Al}_2\text{O}_3$  showed ground state bleach feature around 480 nm and broad excited state (ES) absorption feature after 550 nm, which is similar to the previously reported

results.<sup>219-220</sup> The TA spectra  $\text{Ru}(\text{bpy})_3^{2+}$  on different Im doped ZIF-67 samples showed similar GSB and ES features to that of  $\text{Ru}(\text{bpy})_3^{2+}/\text{Al}_2\text{O}_3$  (Figure 6-8a and Figure 6-8b).



. Figure 6-6 Photocatalysis hydrogen generation efficiency of ZIF-67 based samples under 20h illumination

The difference is ZIF-67 TA feature around 600 nm appeared in later delay time which is consistent to the reported result.<sup>117</sup> Previous works have proven that the communication between  $\text{Ru}(\text{bpy})_3^{2+}$  and ZIF-67 is electron transfer.<sup>117</sup> To compare the electron transfer rate in this work, the ES decay traces and GSB recovery traces of  $\text{Ru}(\text{bpy})_3^{2+}$  on different substrates were plotted in Figure 6-7d and Figure 6-8c, respectively. Compared to ZIF-67, the ES of  $\text{Ru}(\text{bpy})_3^{2+}$  on Im doped ZIF-67 showed a little faster decay, which indicates the faster electron transfer process from  $\text{Ru}(\text{bpy})_3^{2+}$  to Im doped ZIF-67, which may cause the higher hydrogen generation efficiency of Im doped ZIF-67.

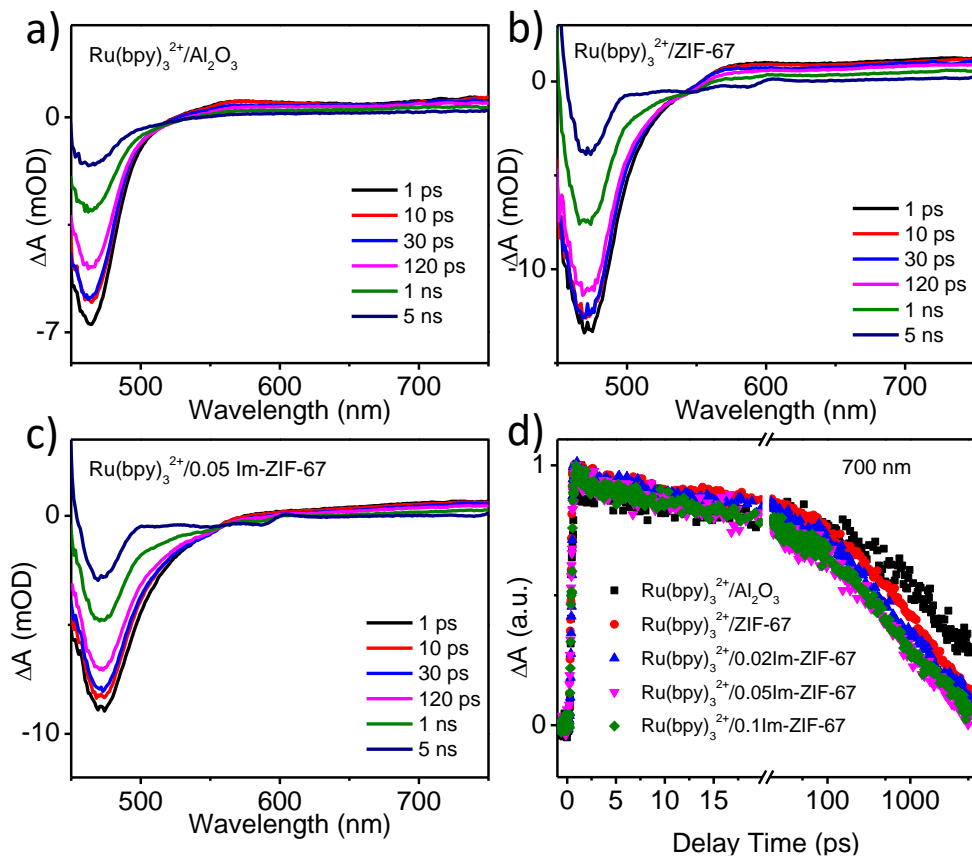


Figure 6-7 TA spectra of  $\text{Ru}(\text{bpy})_3^{2+}/\text{Al}_2\text{O}_3$  (a),  $\text{Ru}(\text{bpy})_3^{2+}/\text{ZIF-67}$  (b) and  $\text{Ru}(\text{bpy})_3^{2+}/0.05\text{Im-ZIF-67}$  (c) under 430 nm excitation. Excited state decay traces of  $\text{Ru}(\text{bpy})_3^{2+}$  on different samples (d).

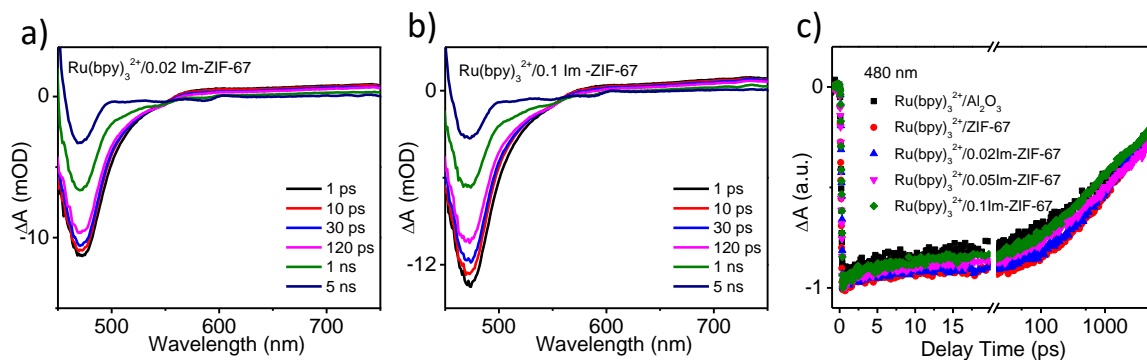


Figure 6-8 TA spectra of  $\text{Ru}(\text{bpy})_3^{2+}/0.02\text{Im-ZIF-67}$  (a) and  $\text{Ru}(\text{bpy})_3^{2+}/0.1\text{Im-ZIF-67}$  (b) under 430 nm excitation. GSB recovery traces of  $\text{Ru}(\text{bpy})_3^{2+}$  on different samples (c).

### 6.3 Conclusion

In summary, the intrinsic photocatalytic property was modified by introducing the second ligand into ZIF-67 structure. The XRD and XAS results confirmed that the introducing of imidazole did not change the crystal structure of ZIF-67 and Co local structure. The results of transient absorption spectra of imidazole doped ZIF-67 showed that the introduced imidazole ligand can facilitate the formation of charge separation state in ZIF-67. When the percentage of imidazole in ZIF-67 reaches 15%, the formation of the charge separation state is fastest after photoexcitation. The communication between imidazole doped ZIF-67 and  $\text{Ru}(\text{bpy})_3\text{Cl}_2$  was also studied by transient absorption spectroscopy. The results showed that the electron transfer rate from  $\text{Ru}(\text{bpy})_3\text{Cl}_2$  to ZIF-67 is much faster in 15% imidazole doping sample, which explains why the 15% imidazole doped ZIF-67 showed the highest hydrogen generation efficiency. This work points out that the intrinsic photocatalytic property can be enhanced by introducing small amount of second imidazole linker, which provides important insight on the future design of ZIFs based photocatalytic system for improving the photocatalytic efficiency.

## Chapter 7

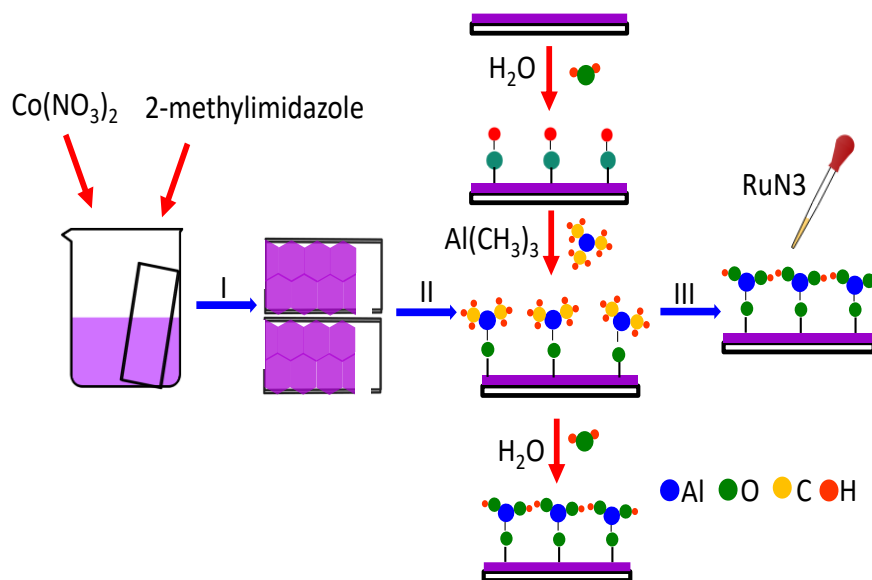
### Distance Dependent Energy Transfer Dynamics from Molecular Donor to Zeolitic Imidazolate Framework Acceptor

#### 7.1 Introduction

While ZIF-67 has broad absorption in both visible and near IR region, the extinction coefficients of these spectral transitions resulting from dipole forbidden d-d transitions of Co nodes are quite low ( $\sim 100\text{-}1000 \text{ mol}\cdot\text{L}^{-1}\cdot\text{cm}^{-1}$ ).<sup>221</sup> In response to this challenge, we encapsulated molecular (RuN3)<sup>124</sup> and semiconductor (CdS)<sup>222</sup> photosensitizers (PS), which have absorption in visible region that compensates the absorption of ZIF-67 and have much larger extinction coefficient, into ZIF-67. We showed that both systems can strengthen the light harvesting ability of ZIF-67 as efficient energy transfer (ENT) can occur from guest PSs to ZIF-67. These results demonstrate that encapsulating a guest unit chromophore that can relay energy to ZIFs through ENT is a promising approach to enhance the light harvesting ability of ZIFs. A natural question that follows these ENT studies is to unravel the key factors that control the dynamics of ENT. It has been shown previously that ENT efficiency is largely dependent on the distance between the donor and acceptor.<sup>223-230</sup> In this project, I investigated the impact of distance between RuN3 and ZIF-67 on the ENT dynamics in RuN3/ZIF-67 hybrid. The distance between RuN3 and ZIF-67 is controlled by tuning the thickness of the Al<sub>2</sub>O<sub>3</sub> layer from 3 nm to 8.5 nm, which is deposited on the surface of ZIF-67 film before sensitization of RuN3 by atomic layer deposition (ALD). We show that the ENT efficiency decreases with the increasing thickness of Al<sub>2</sub>O<sub>3</sub> between RuN3 and ZIF-67, where the theoretical Förster radius estimated according to the reported point to plane resonance energy transfer under 4th-power law<sup>225, 231-232</sup> is 14.4 nm.

## 7.2 Results and discussion

The schematic representation of the synthesis of RuN<sub>3</sub>/Al<sub>2</sub>O<sub>3</sub>/ZIF-67 hybrid films is illustrated in scheme 7-1 (see details in experimental chapter). In the first step, a glass slide pre-treated with Piranha solution was immersed into the mixture of Co(NO<sub>3</sub>)<sub>2</sub>·6H<sub>2</sub>O and 2-methylimidazole (2mIm). After about 1h, transparent and continuous ZIF-67 film was formed on both sides of the glass slide (step I).<sup>95, 124</sup> ZIF-67 crystals on one side of the film is scratched off to make a single-side ZIF-67 film. Al<sub>2</sub>O<sub>3</sub> layer with different thickness was then deposited on the surface of ZIF-67 film using ALD (step II). At temperature of 100-200°C, the deposition of Al<sub>2</sub>O<sub>3</sub> usually has a stable growth rate of 0.1-0.11 nm/cycle on non-porous substrates.<sup>233-235</sup> However, as demonstrated by the transmission electron microscopy (TEM) images, a much thicker layer of Al<sub>2</sub>O<sub>3</sub> was identified (Figure 7-1). This can be explained by the nanoporous structure of ZIF-67, where the Al<sub>2</sub>O<sub>3</sub> not only deposit on the surface but also the subsurface in the nanostructures. As a result, alternatively depositing 10 to 40 cycles of trimethylaluminum and water at 120°C resulted into 3 nm to 8.5 nm Al<sub>2</sub>O<sub>3</sub> thin film on ZIF-67, the thickness of Al<sub>2</sub>O<sub>3</sub> films have been shown in Table 7-1. This is followed by dropping the same amount of RuN<sub>3</sub> in methanol solution onto the Al<sub>2</sub>O<sub>3</sub>/ZIF-67 films to form RuN<sub>3</sub>/ Al<sub>2</sub>O<sub>3</sub>/ZIF-67 hybrid films (step III).



Scheme 7-1. Schematic representation of the synthesis of RuN<sub>3</sub>/Al<sub>2</sub>O<sub>3</sub>/ZIF-67 thin film.

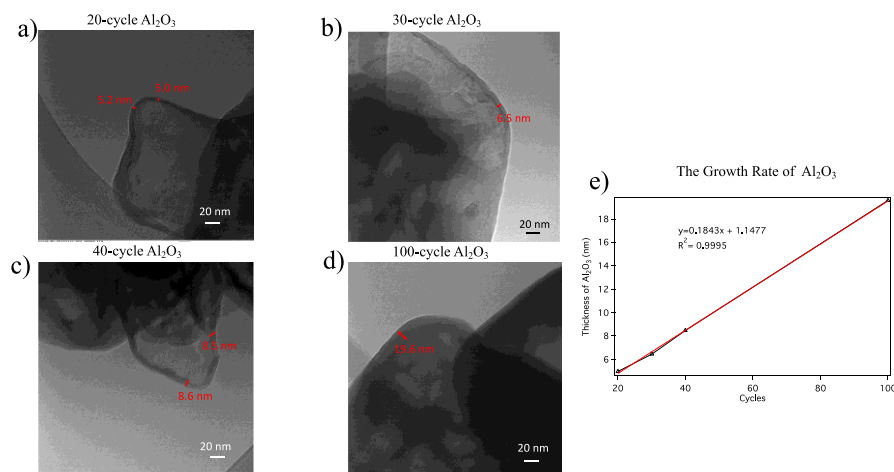


Figure 7-1. TEM images of various cycles of Al<sub>2</sub>O<sub>3</sub> deposited on ZIF 67. (a) 20-cycle (b) 30-cycle (c) 40-cycle (d) 100-cycle (e) cycles and thickness relationship of deposited Al<sub>2</sub>O<sub>3</sub>.

Table 7-1. Al<sub>2</sub>O<sub>3</sub> film thickness at different ALD cycles.

ALD Cycles	Thickness of Al <sub>2</sub> O <sub>3</sub> films (nm)
10	3
20	5
30	6.5
40	8.5

Figure 7-2a shows the XRD patterns of blank glass slides, Al<sub>2</sub>O<sub>3</sub> on glass slides, ZIF-67 on glass slide, Al<sub>2</sub>O<sub>3</sub> (8.5 nm)/ZIF-67, and RuN<sub>3</sub>/ Al<sub>2</sub>O<sub>3</sub> (8.5 nm)/ZIF-67. A broad peak was observed in the range of 20° to 40° among all samples including the naked glass slide, which can be attributed to the diffraction of amorphous glass. Al<sub>2</sub>O<sub>3</sub>/ZIF-67 and RuN<sub>3</sub>/ Al<sub>2</sub>O<sub>3</sub>/ZIF-67 films (Figure 7-2a-c) all show similar XRD patterns to ZIF-67 film on glass, suggesting that ZIF-67 structure retains in the films after ALD deposition of Al<sub>2</sub>O<sub>3</sub> and RuN<sub>3</sub> sensitization. Note that the diffraction patterns of ZIF-67 film on glass seem different from that of ZIF-67 crystals (Figure 7-2d). This can be attributed to the impact of glass slide on the diffraction patterns as the XRD patterns of ZIF-67 crystals scratched off from the glass slide resemble that of ZIF-67 crystals synthesized from the standard growth (Figure 7-2d). The retain of ZIF-67 structure in these hybrid films was further supported by the UV-Visible absorption spectra (Figure 7-3), where Al<sub>2</sub>O<sub>3</sub>/ZIF-67 and RuN<sub>3</sub>/ Al<sub>2</sub>O<sub>3</sub>/ZIF-67 films with different thickness of Al<sub>2</sub>O<sub>3</sub> all show absorption peak centered at 585 nm originating from Td CoII d-d transition, consistent with that of ZIF-67.<sup>95</sup> While RuN<sub>3</sub> has prominent absorption peak around 500 nm corresponding to ligand-to-metal charge transfer band (LMCT) (pink plot in Figure 7-3a), it cannot be easily seen from the UV-visible absorption spectrum of RuN<sub>3</sub>/ZIF-67 due to its overlap with ZIF-67 absorption.

Nevertheless, the transient absorption experiments below confirm the adsorption of RuN3 on the surface of Al<sub>2</sub>O<sub>3</sub>/ZIF-67 film.

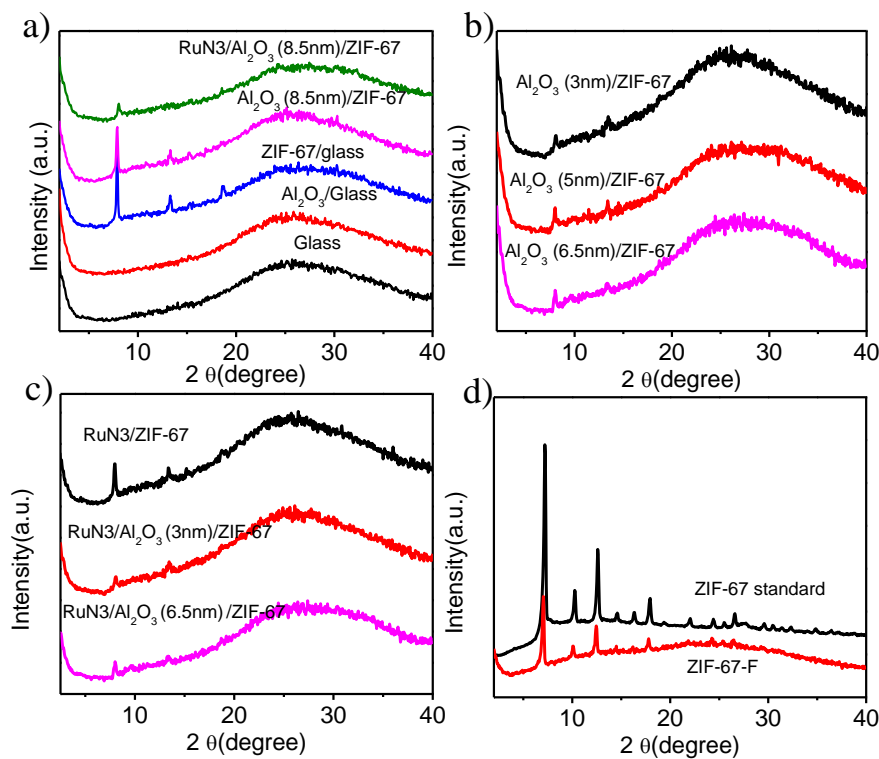


Figure 7-2 a) XRD patterns of glass, Al<sub>2</sub>O<sub>3</sub>/glass, ZIF-67/glass, Al<sub>2</sub>O<sub>3</sub> (8.5nm)/ZIF-67 and RuN3/ Al<sub>2</sub>O<sub>3</sub> (8.5nm)/ZIF-67; XRD patterns of Al<sub>2</sub>O<sub>3</sub> on ZIF-67 films; (b), RuN3 sensitized films (c), ZIF-67 crystals synthesized from standard growth (denoted ZIF-67 standard) and ZIF-67 powder scratched from ZIF-67 film (denoted ZIF-67-F) (d).

Transient absorption (TA) spectroscopy is used to examine the impact of the thickness of Al<sub>2</sub>O<sub>3</sub> layer on the ENT dynamics from RuN3 to ZIF-67. Figure 7-4a shows the TA spectra of RuN3/ZIF-67 following 410 nm excitation which selectively excites RuN3 as ZIF-67 has negligible absorption at 410 nm. Consistent with previous literature result,<sup>124</sup>

immediately following the excitation, the TA spectra of RuN3/ZIF-67 show a negative ground state bleach (GSB) centered at  $\sim 530$  nm and a broad positive excited state

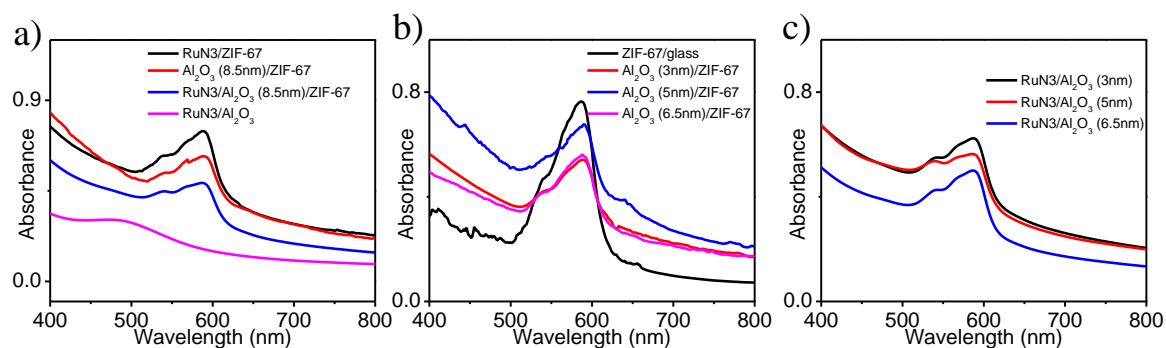


Figure 7-3 UV-visible absorption spectra of RuN3/ZIF-67, Al<sub>2</sub>O<sub>3</sub>(8.5nm)/ZIF-67, RuN3/Al<sub>2</sub>O<sub>3</sub> (8.5nm)/ZIF-67 and RuN3/ Al<sub>2</sub>O<sub>3</sub> (a). UV-visible absorption spectra of Al<sub>2</sub>O<sub>3</sub> on ZIF-67 film (b) and RuN3 sensitized films (c) with different thickness of Al<sub>2</sub>O<sub>3</sub>

absorption (ESA) feature at  $> 570$  nm, which is due to the excitation of RuN3, resulting in the depopulation of RuN3 ground state and population of RuN3 excited state. As the lifetime of excited singlet state of LMCT (<sup>1</sup>LMCT) is  $< 100$  fs,<sup>236-237</sup> which is much faster than our instrument response time ( $\sim 200$  fs), the ESA absorption of RuN3 can be attributed to <sup>3</sup>LMCT. The GSB of RuN3 recovers and ESA decays with time simultaneously (Figure 7-4b), which is accompanied by the formation of a derivative feature consisting of a negative feature centered at 585 nm and absorption at 605 nm at later time ( $> 200$  ps), consistent with the typical spectral features of the excited state of ZIF-67 corresponding to <sup>4</sup>A<sub>2</sub>(F)-<sup>4</sup>T<sub>1</sub>(P) Co d-d transition,<sup>95, 117</sup> suggesting that the excitation of RuN3 leads to the formation of excited ZIF-67.<sup>124</sup> Moreover, the GSB recovery and ESA decay in RuN3/ZIF-67 are much faster than that of RuN3/ Al<sub>2</sub>O<sub>3</sub> (Figure 7-4b), where the latter is used as a

model system for intrinsic ES dynamics of RuN3 on a solid surface as ENT from RuN3 to  $\text{Al}_2\text{O}_3$  is not expected due to significantly larger band gap of  $\text{Al}_2\text{O}_3$  than RuN3.<sup>238-240</sup> These results together support that ENT occurs from RuN3 ( $^3\text{LMCT}$ ) to ZIF-67 ( $^4\text{A}_2$ ) following

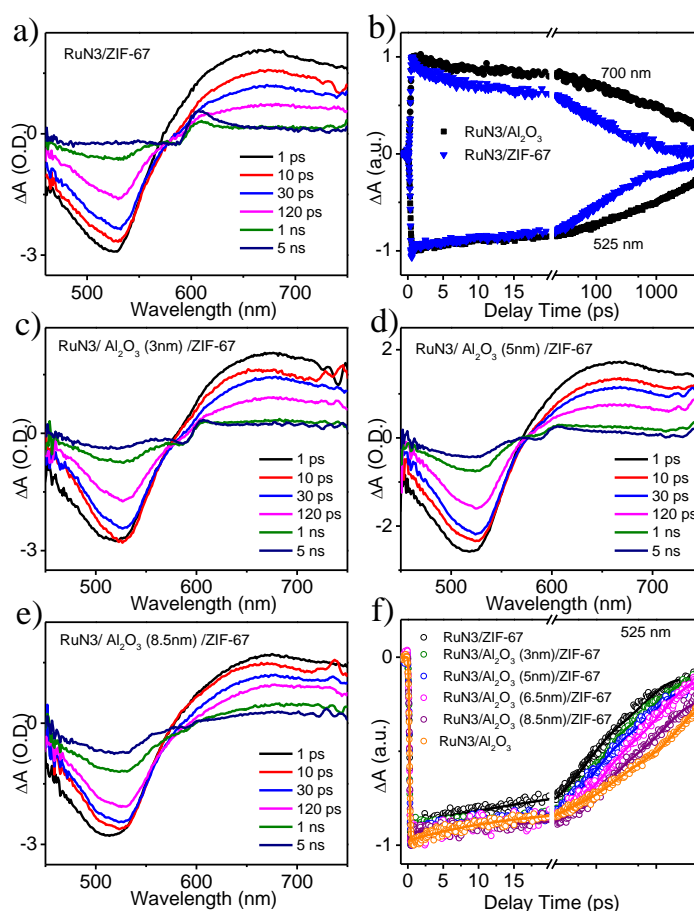


Figure 7-4. Transient absorption spectra of RuN3/ZIF-67 (a), RuN3/ $\text{Al}_2\text{O}_3$ (3nm)/ZIF-67 (c), RuN3/ $\text{Al}_2\text{O}_3$ (5nm)/ZIF-67 (d), and RuN3/ $\text{Al}_2\text{O}_3$ (8.5nm)/ZIF-67 (e); b) the comparison of GSB recovery and ESA decay kinetics of RuN3 on ZIF-67 and  $\text{Al}_2\text{O}_3$ ; f) The comparison of GSB recovery kinetics of RuN3 on different substrate.

the excitation of RuN3, which quenches the ES of RuN3 and results in the formation ZIF-67 ES, consistent with the previous report.<sup>124</sup> With the presence of  $\text{Al}_2\text{O}_3$  layer (3 nm thickness) between RuN3 and ZIF-67 (Figure 7-4c), the TA spectra of RuN3/ $\text{Al}_2\text{O}_3$  (3

nm)/ZIF-67 resemble that of RuN3/ZIF-67. However, with increasing thickness of Al<sub>2</sub>O<sub>3</sub>, the derivative feature corresponding to ES of ZIF-67 in RuN3/Al<sub>2</sub>O<sub>3</sub>/ZIF-67 becomes weaker and weaker (Figure 7-4 d-e and Figure 7-5) and can be barely seen when the thickness of Al<sub>2</sub>O<sub>3</sub> is 8.5 nm (Figure 7-4e). These results suggest that ENT process is partially blocked by Al<sub>2</sub>O<sub>3</sub> due to its inert nature, which results in decreasing ENT rate with increasing thickness of Al<sub>2</sub>O<sub>3</sub>.

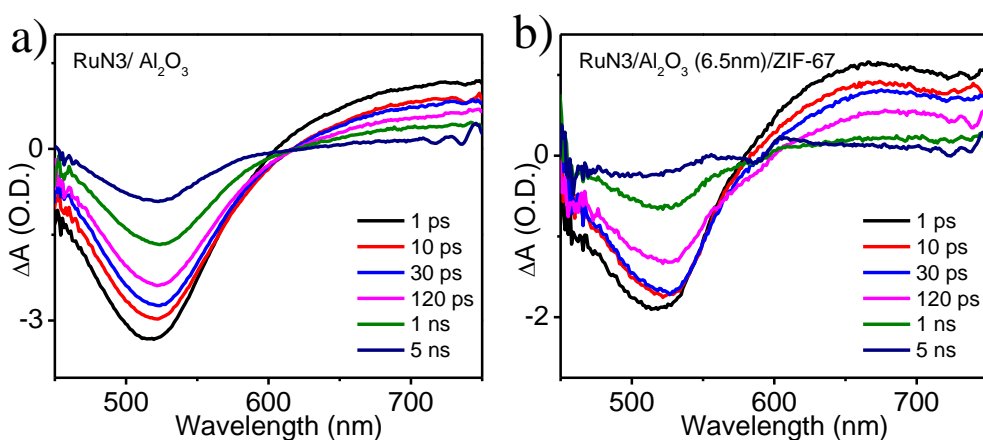


Figure 7-5. Transient absorption spectra of RuN3/Al<sub>2</sub>O<sub>3</sub> (a) and RuN3/Al<sub>2</sub>O<sub>3</sub>(6.5nm)/ZIF-67 (b).

The dependence of ENT process on Al<sub>2</sub>O<sub>3</sub> thickness can be more clearly seen from the comparison of the GSB kinetics of RuN3 at 525 nm (Figure 7-4f) among RuN3/ Al<sub>2</sub>O<sub>3</sub>/ZIF-67 samples with different thickness of Al<sub>2</sub>O<sub>3</sub>. As shown in Figure 7-4f, the GSB recovery kinetics of RuN3/ Al<sub>2</sub>O<sub>3</sub>/ZIF-67 becomes slower with the increasing thickness of Al<sub>2</sub>O<sub>3</sub>, consistent with the assignment above. Since the recovery lifetime of GSB of these RuN3/ Al<sub>2</sub>O<sub>3</sub>/ZIF-67 samples is much longer than 5 ns, which is beyond our TA time window, the

ENT time was calculated based on the half lifetime ( $\tau_{1/2}$ ), which is the time that the kinetic trace decays to half of its maximum amplitude. As listed in Table 7-2,  $\tau_{1/2}$  for RuN3/Al<sub>2</sub>O<sub>3</sub>/ZIF-67 with 0 nm, 3 nm, 5 nm, 6.5 nm, and 8.5 nm is 96 ps, 158 ps, 182 ps, 287 ps, 528 ps, respectively. According to these half lifetimes, we estimated the ENT time according to equation 1.

$$1/\tau_{1/2} = 1/\tau_0 + 1/\tau_{\text{ENT}} \quad (1)$$

$$\eta = \tau_{1/2}/\tau_{\text{ENT}} \quad (2)$$

where  $\tau_{\text{ENT}}$  is the ENT time from RuN3 to ZIF-67 and  $\tau_0$  is the intrinsic ES decay time of RuN3. ENT efficiency ( $\eta$ ) can then be calculated according to equation 2. The calculated ENT efficiency is also listed in Table 7-2. The ENT efficiency decreased almost half (from 90.6% to 46.0%) when the thickness of Al<sub>2</sub>O<sub>3</sub> thin film increased to 8.5 nm, indicating that ENT efficiency in RuN3/ZIF-67 system is sensitive to the distance between RuN3 and ZIF-67.

Table 7-2. The half lifetime of RuN3 GSB on different films and estimated ENT time and efficiency of RuN3/Al<sub>2</sub>O<sub>3</sub>/ZIF-67.

	$\tau_{1/2}$ (ps)	$\tau_{\text{ENT}}$ (ps)	$\eta_{\text{ENT}}$ (100%)
RuN3/ZIF-67	96	106	90.6
RuN3/Al <sub>2</sub> O <sub>3</sub> (3nm)/ZIF-67	158	188	84.0
RuN3/Al <sub>2</sub> O <sub>3</sub> (5nm)/ZIF-67	182	223	81.6
RuN3/Al <sub>2</sub> O <sub>3</sub> (6.5nm)/ZIF-67	287	406	70.7
RuN3/Al <sub>2</sub> O <sub>3</sub> (8.5nm)/ZIF-67	528	1147	46.0
RuN3/Al <sub>2</sub> O <sub>3</sub> ( $\tau_0$ )	978	-	-

The theoretical Förster radius of this system was estimated by fitting the experimental data using equation 3:<sup>225, 231-232</sup>

$$\eta = 1/[1+(R/R_0)^4] \quad (3)$$

where  $R_0$  and  $R$  are the Förster radius and distance between the donor and acceptor, respectively.  $R_0$  equals to  $R$  when the ENT efficiency reaches 50%. In the fitting process, the distance between ZIF-67 and RuN3 without  $\text{Al}_2\text{O}_3$  ( $r$ ) and the Förster radius ( $R_0$ ) were used as fitting parameters, where  $R$  is the sum of  $r$  and the thickness of  $\text{Al}_2\text{O}_3$  layer. As shown in Figure 7-6, the experimental results can be adequately fit by the proposed model. From the best fitting, we obtained  $r$  value of 5.7 nm and  $R_0$  of 14.4 nm. The  $R_0$  value in this system is much higher than the previously reported molecular donor/acceptor system ( $< 5$  nm).<sup>124, 241-242</sup> Given that larger  $R_0$  value results in higher FRET efficiency (equation 3),<sup>242-243</sup> the much higher value in current RuN3/ZIF-67 than the molecular systems suggests that the framework of ZIF might be beneficial for ENT process. In addition, a larger  $R_0$  value can typically facilitate long-range energy transfer,<sup>244</sup> which suggests the potential of further enhancing the light absorption ability of ZIF systems through controlling ENT process.

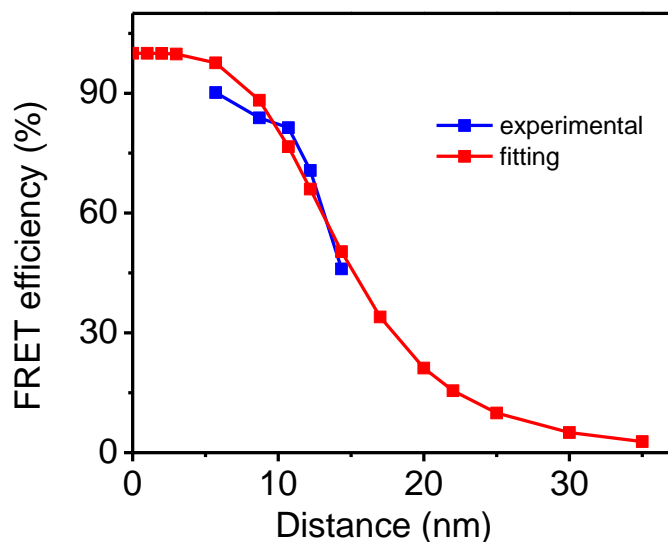


Figure 7-6. The ENT efficiency as a function of distance between ZIF-67 and RuN3.

### 7.3 Conclusion

In summary, we report the ENT dynamics from RuN3 to ZIF-67 and the impact of distance between RuN3 (donor) and ZIF-67 (acceptor) on ENT efficiency, where the distance between donor and acceptor was controlled by tuning the thickness of  $\text{Al}_2\text{O}_3$  film deposited on the surface of ZIF-67 using atomic layer deposition (ALD). Using transient absorption spectroscopy, we show that ENT efficiency decreases with increasing thickness of the  $\text{Al}_2\text{O}_3$  layer between RuN3 and ZIF-67. According to these experimental results, the Förster radius for this system was estimated to be 14.4 nm, which is much larger than many molecular donor/acceptor systems, suggesting the promise of enhancing light harvesting capability of ZIFs through ENT process. This work not only demonstrates the capability to tuning the distance of donor and acceptor by depositing different-thickness  $\text{Al}_2\text{O}_3$  layers using ALD but also provides new insight on controlling ENT dynamics in RuN3/ZIF-67.

## Chapter 8

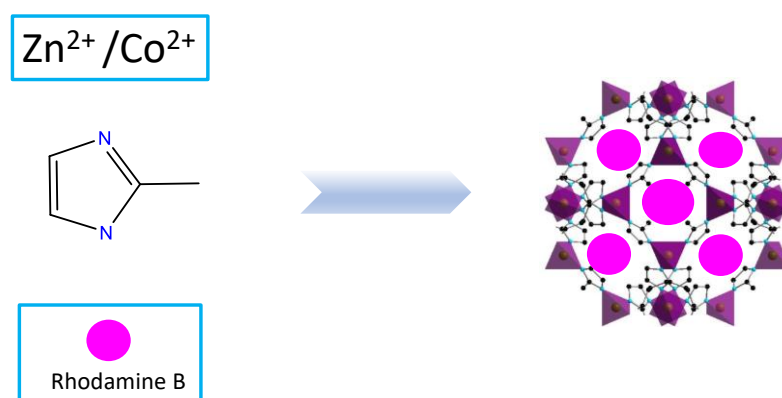
### Energy Transfer Dynamics of Rhodamine B encapsulated Zeolitic imidazolate Frameworks

#### 8.1 Introduction

As discussed in our previous works,<sup>117, 124</sup> the communication between the photosensitizer and the photocatalyst plays a key role during photocatalytic process, which may limit the utilization efficiency of solar energy. Based on the reported works,<sup>5, 116-117, 245-246</sup> the communication between the photosensitizer and the photocatalyst in heterogenous photocatalytic system is either through electron transfer or energy transfer, which are related to the distance between the photosensitizer and photocatalyst, while the photocatalyst and the photosensitizer are separated in most of the heterogenous photocatalysis systems, indicating the possibility of enhancing communication between the photocatalytic active center and the photosensitizer by assembling the two species together. In ZIFs photocatalytic systems, the reported CO<sub>2</sub> photocatalytic reduction and hydrogen generation systems are separated.<sup>115, 117, 119, 124</sup> Since ZIFs is bulky compared to molecular systems, the photosensitizer was only attached to the surface of the ZIFs, which hindered the utilization of either photocatalyst or photosensitizer.

As reported, the pore in MOFs structure can be used as a host to support the introduced nanoparticles, catalysts or dye molecules, which can help to increase the recycling or photocatalytic efficiency.<sup>54, 219, 247-249</sup> Inspired by the reported works, encapsulation the photosensitizer into the ZIFs structure is one strategy to increase the communication between the photosensitizer and ZIFs, which will decrease the distance between the photocatalytic center and the photosensitizer as well as disperse the photosensitizer

uniformly into ZIFs structure. In this project, the organic dye Rhodamine B (RB) was encapsulated into Co doped ZIF-8 structure. The communication between RB and Co center has been studied by transient absorption spectra. The concentration of Co center effect on the communication between RB and Co center has also been studied. Scheme 8-1 illustrated the encapsulation of RB into ZIFs structure.



Scheme 8-1 illustration of encapsulating dye into ZIFs structure

## 8.2 Results and Discussion

As shown in Figure 8-1a, the XRD patterns of RB-ZIF-8 are similar to that of ZIF-8,<sup>195</sup> which suggests that ZIF-8 structure retains due to encapsulation of RB. The UV-visible diffuse reflectance spectra (Figure 8-1b) showed the absorption feature centered at 545 nm while the steady state emission spectra (Figure 8-1c) showed similar spectra centered at 575 nm of RB methanol solution and RB/ZIF-8, which confirmed the existence of RB in ZIF-8 structure. After confirming the successful encapsulation of RB into ZIF-8 structure, Co center was introduced into RB-ZIF-8 structure. As shown in Figure 8-2a, the Co doped RB-ZIF-8 showed similar XRD structure to RB-ZIF-8, indicating the introducing of Co

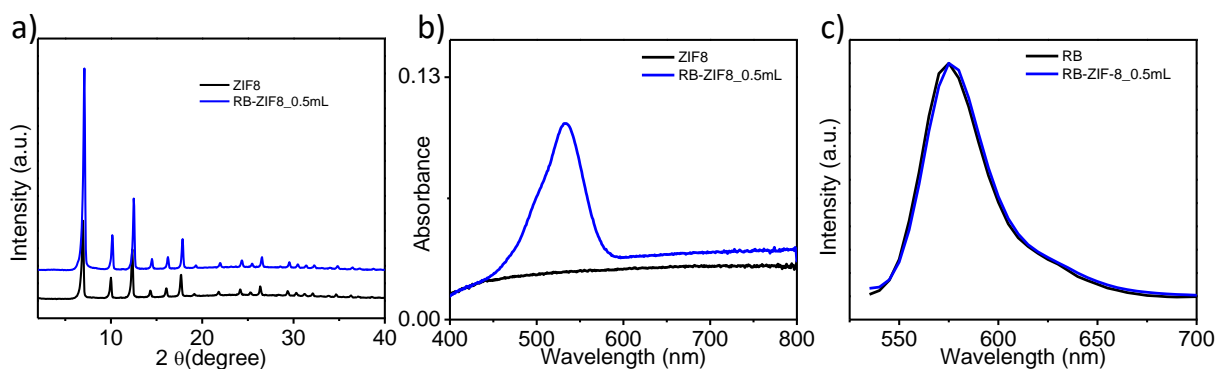


Figure 8-1 XRD (a), UV-Visible diffuse reflectance spectra(b) and emission spectra (c) of prepared ZIF-8 and RB-ZIF-8

did not change the ordered structure of RB-ZIF-8. UV-Vis diffuse reflectance spectra were used to detect the introducing of Co based on the unique tetrahedral  $\text{Co}^{2+}$  d-d transition band in the visible region.<sup>95, 113</sup> As shown in Figure 8-2b, there were two main absorption features in the range of 470 nm to 620 nm. The first absorption feature centered at 520 nm was assigned to the absorption feature of RB and the second absorption feature centered at 585 nm was assigned to tetrahedral Co d-d transition absorption feature. With increasing concentration of Co, the absorption intensity increased, indicating the successful doping of Co.

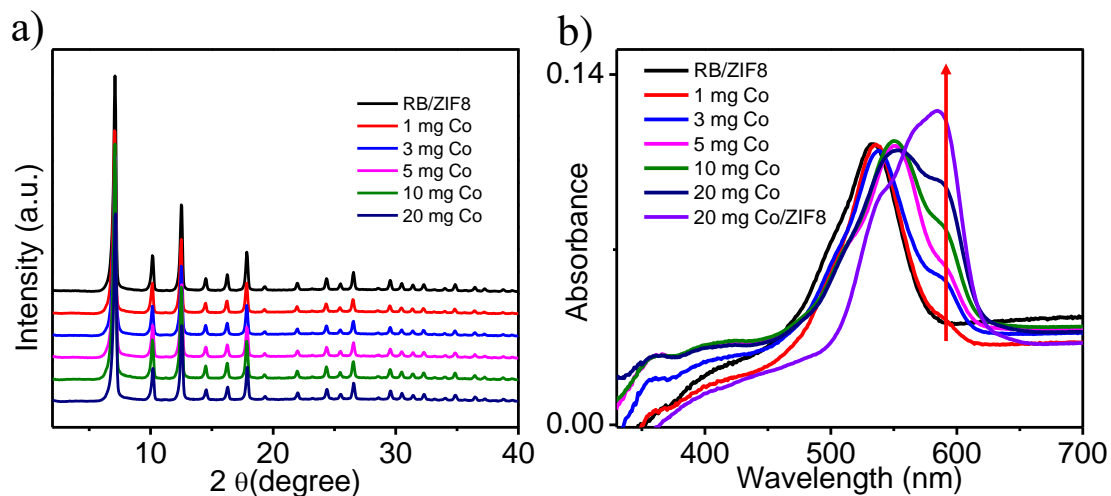


Figure 8-2 XRD (a) and UV-Vis diffuse reflectance spectra (b) of different amount of Co doped RB-ZIF-8.

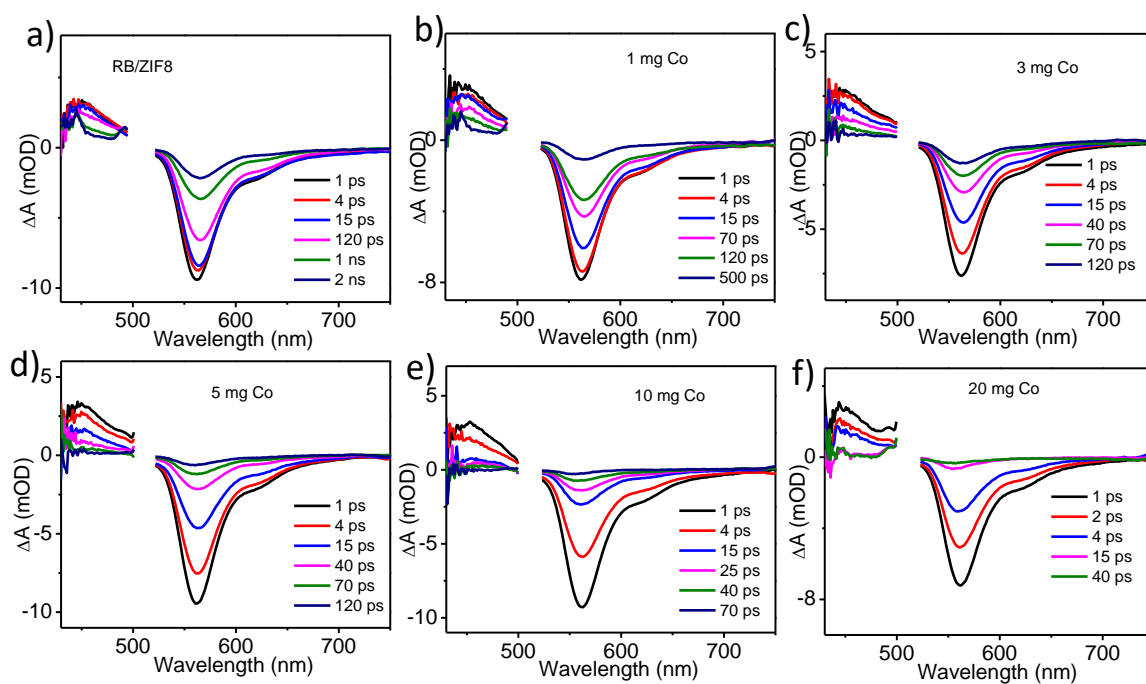


Figure 8-3 OTA spectra of the obtained RB-ZIF-8 (a), 1 mg Co (b), 3 mg (c), 5 mg (d), 10 mg (e) and 20 mg Co (f) samples under 510 nm excitation.

To study the communication between RB and Co center, transient absorption spectra were performed under 510 nm excitation which selectively excite RB. The TA results were shown in Figure 8-3. The TA spectra showed the standard transient absorption features of RB, i.e. the positive feature before 500 nm and the obvious ground state bleach (GSB) feature centered at 560 nm. which are consistent with the reported results<sup>250-251</sup>. As shown in Figure 8-3a-f, the GSB signal recovered much faster with the increasing concentration of Co center.

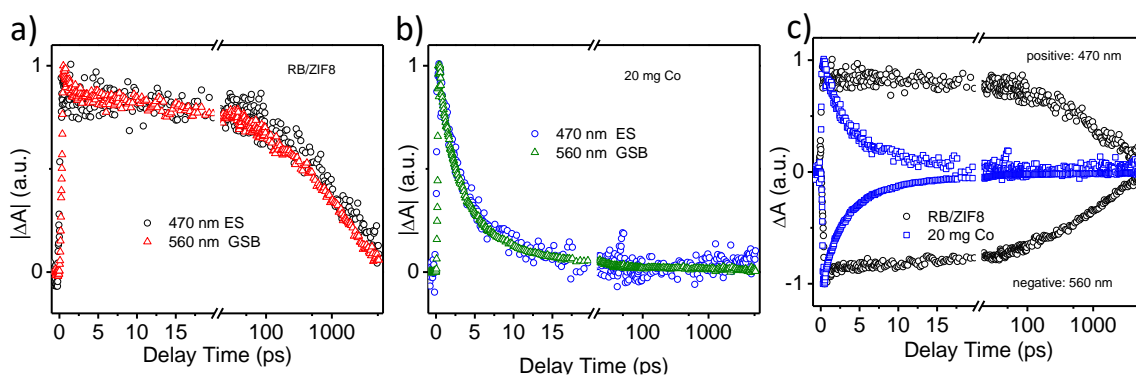


Figure 8-4 Kinetic traces of RB/ZIF-8 (a), (b) 20 mg Co (b) and kinetics comparison between RB-ZIF-8 and 20 mg Co sample (c).

To figure out the communication between RB and Co center, the kinetics comparison between RB-ZIF-8 and 20 mg Co sample was performed and shown in Figure 8-4. In both RB-ZIF-8 and 20 mg Co sample, the RB excited state decay and GSB recovery showed similar rate, while 20 mg Co sample showed faster excited state decay and GSB recovery, suggesting that energy transfer occurred from RB to Co center.<sup>124</sup> To study the energy transfer efficiency between RB and Co center, the kinetics traces of RB excited state and GSB have been plot in Figure 8-5. Since the lifetime of RB-ZIF-8 sample is larger than 5

ns which is beyond our instrument time scale, we use the half lifetime of each sample to calculate the energy transfer efficiency. The calculation followed the previously reported method<sup>252</sup> and the calculation results were listed in Table 8-1. As listed in Table 8-1, the  $\tau_{1/2}$  decreased from 297 ps in RB/ZIF-8 to 2.5 ps in 20 mg Co sample, indicating fast charge recombination in Co doped samples. With the increasing concentration of Co center, the energy transfer efficiency increased from 75.75% to 99.58%, indicating that the energy transfer efficiency increased while increasing the acceptor concentration when the amount of donor was the same.

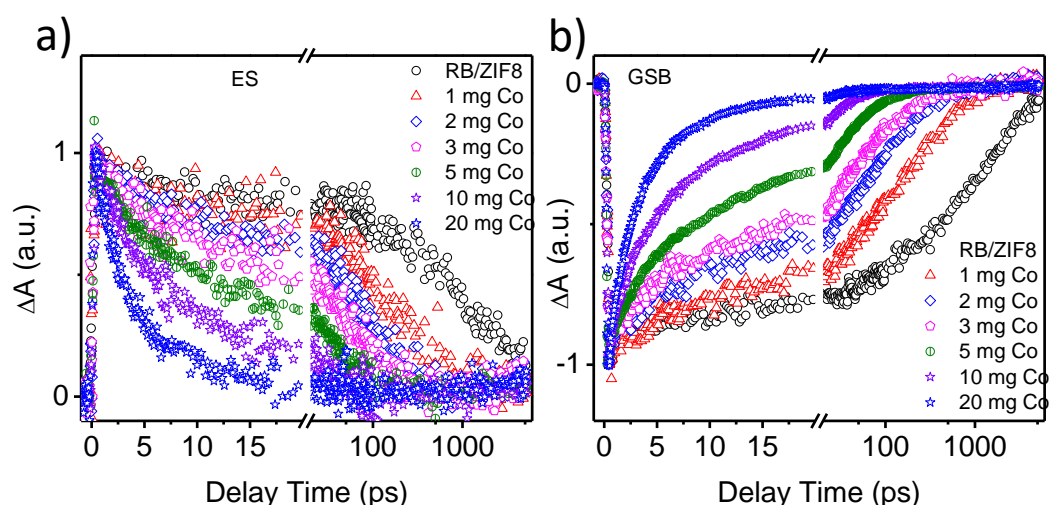


Figure 8-5 Kinetics comparison of RB-CoZIF-8 system: (a) excited state decay; (b) ground state bleach recovery.

Table 8-1. Energy transfer parameter of RB-CoZIF-8 system.

sample	$\tau_{1/2}$ (ps)	$\tau_{ENT}$ (ps)	$\eta_{ENT}$ (100%)
RB/ZIF-8	297	-	-
1 mg Co	76	95.4	75.75
2 mg Co	26	28.5	91.25
3 mg Co	17	18	94.27
5 mg Co	8	8.22	97.3
10 mg Co	4.5	4.52	98.48
20 mg Co	2.5	2.52	99.58

The amount of RB in Co-ZIF-8 structure was measured based on the reported method.<sup>69</sup> First, the emission spectra of RB methanol solution with different concentration were collected and shown in Figure 8-6a to plot the concentration-intensity curve (Figure 8-6b). Then, the RB/ZIF-8 based samples with a certain amount was dispersed in 2 mL methanol containing 1 drop of diluted HCl which was used to measure the emission spectra (Figure 8-6c) and record the fluorescent intensity. The amount of RB in the samples was calculated based on the concentration-intensity curve and the results were listed in Table-8-2. The amount of Co in the RB/ZIF-8 based samples was measured by Inductively coupled plasma mass spectrometry (ICP-MS) and the results were listed in Table 8-3.

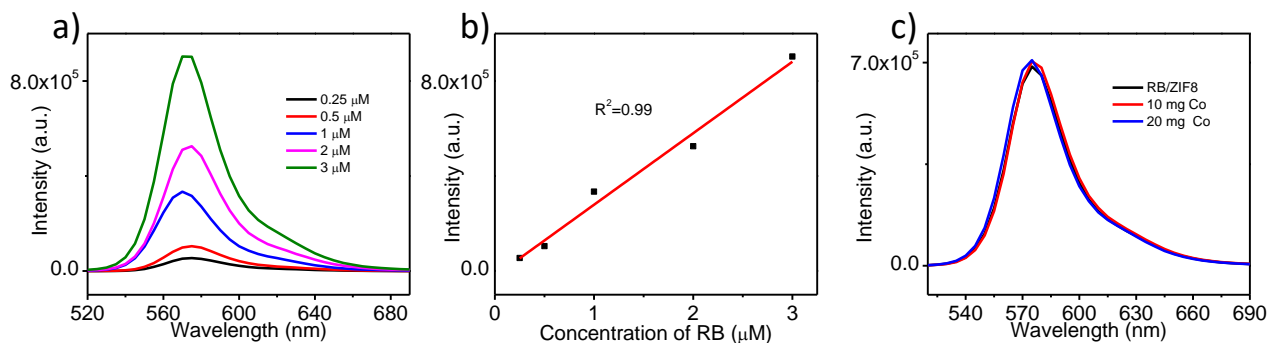


Figure 8-6 (a) emission of RB MeOH solution with different concentration; (b) emission intensity vs. RB concentration plot; (c) emission of three digested samples.

Table 8-2. RB concentration in different samples.

sample	concentration	RB wt %
RB/ZIF-8	2.39 μM	0.115
10 mg Co	2.41 μM	0.116
20 mg Co	2.42 μM	0.116

To study the relationship between the energy transfer efficiency and the concentration of Co center, the results were plotted and shown in Figure 8-7. As we can see from Figure 8-7, Table 8-1 and Table 8-3, when the Co concentration in the hybrid samples increased from 0.21% to 0.42%, the energy transfer efficiency increased from 75.75% to 91.25% while the energy transfer efficiency only increased 3% to 94.27% when the Co concentration increased to 0.59%, indicating that the Co concentration almost reached the saturated level to increase the energy transfer. This concentration study can help to guide design a system with using less acceptor with high energy transfer efficiency

Table 8-3. ICP results of Co concentration in different samples.

Sample	wt % Co	Co/RB
1 mg Co	0.21	14.8
2 mg Co	0.42	29.4
3 mg Co	0.59	41.7
5 mg Co	0.92	64.6
10 mg Co	1.77	123.9
20 mg Co	3.44	244.4

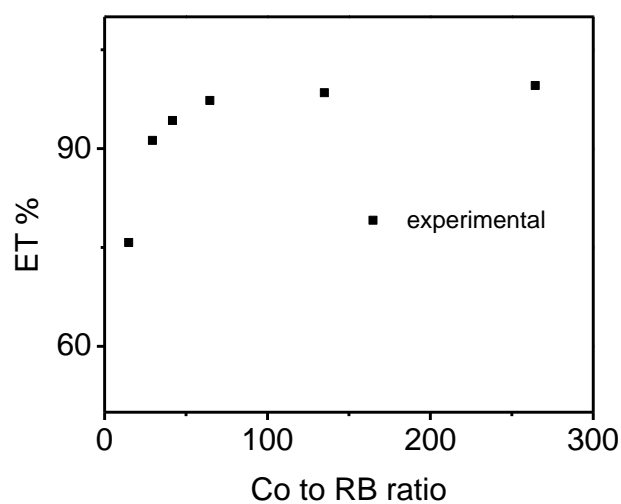


Figure 8-7 the plot of energy transfer vs. Co to RB ratio

### 8.3 Conclusion

In this work, RB was successfully encapsulated into ZIFs structure. The encapsulation amount of RB was kept the same when the same amount of RB solution was used. The

XRD results confirmed that the encapsulation of the dye did not change the structure of ZIFs. The UV-Vis spectra showed the existence of RB and tetrahedral Co in RB-CoZIF-8 system. Energy transfer from RB to Co center was confirmed by optical transient absorption spectra and the energy transfer efficiency increased with the increasing concentration of Co center. Energy transfer efficiency reaches 91.25% with only 0.42% Co, then almost reaches the saturated level when the amount of Co increases to 0.92%, indicating we can design a energy transfer system with energy transfer just reaches the saturated level which can help to low the cost by using less amount of acceptor.

## Chapter 9 Conclusion and Future work

In this dissertation, we have investigated the intrinsic photophysical and photocatalytic properties of CuInS<sub>2</sub> quantum dots and zeolitic imidazolate frameworks, aiming at understanding the fundamental mechanism of these materials during the photoinduced catalytic reaction. To achieve the research goal, the synthesis and design of these materials were combined with the fundamental spectroscopic studies using a suit of steady state and time resolved spectroscopic methods to gain insight into the correlation of material structure with their photophysical and photocatalytic properties. The knowledge gained from these studies will provide important guidance to further optimize these materials for their future applications in solar to fuel conversion. Conclusions drawn from this work are presented in this final section.

### **9.1 Conclusion and future work of CuInS<sub>2</sub>**

CuInS<sub>2</sub> quantum dots were first investigated as an efficient light harvesting material in order to understand the carrier dynamics during the photoexcitation process using the combination of multiple spectroscopic techniques which has been discussed in chapter 3. By changing the nucleation time during synthesis process, CuInS<sub>2</sub> quantum dots with different particle size were confirmed by small angle X-ray scattering technology. X-ray absorption spectroscopic studies showed that there are large amount of surface Cu atoms without tetrahedral structure, and that tetrahedral Cu center is more developed in CuInS<sub>2</sub> quantum dots with longer nucleation time. The results from the time resolved absorption spectroscopic studies showed that the surface Cu atoms without tetrahedral structure served as the hole trapping sites during the photoinduced trapping process. The longer nucleation

time (larger size) CuInS<sub>2</sub> quantum dots exhibited longer electron-hole recombination time, which suggests the possibility to control the carrier dynamics by controlling the surface structure of CuInS<sub>2</sub> quantum dots.

After the carrier dynamics studies of CuInS<sub>2</sub>, another experiment was designed to investigate the catalytic performance of CuInS<sub>2</sub>/ZnS (CIS/ZnS) quantum dots for photocatalytic hydrogen generation (Chapter 4). The ratio of Cu to In was varied by keeping the amount of Cu precursor the same while increasing the amount of In precursor during the synthesis process (. With increasing Cu deficiency (smaller Cu to In ratio), both UV-visible absorption and emission spectra showed blue shift, while the conduction band edge of CIS/ZnS quantum dots showed negligible difference, indicating that the valence band edge changes. The photocatalytic hydrogen generation results showed higher hydrogen generation efficiency of CIS/ZnS with more Cu deficiency and the photon-to H<sub>2</sub> quantum yield in this system with Cu<sub>0.12</sub>InS<sub>2</sub>/ZnS reached 5.2% which is slightly higher than the previously best-performing system (5%), suggesting that the presence of Cu deficiency can significantly enhance the photocatalytic performance of CIS/ZnS quantum dots with ascorbic acid (AA) as the electron donor. The electron transfer (ET) process from AA to CIS/ZnS quantum dots, which is a key pathway that determines the overall efficiency for H<sub>2</sub> generation, was examined by measuring the steady state emission quenching of CIS/ZnS as a function of AA concentration. The results showed the ET rate increased considerably with increasing Cu deficiency, resulting from the lower valence band edge in higher Cu deficiency CIS/ZnS quantum dots, which leads to a larger driving force for the ET to occur from AA to CIS/ZnS quantum dots.

Inspired from the progress of CuInS<sub>2</sub> quantum dots made in this work, future work can aim at increasing photon-to-fuel quantum yield and exploring new photocatalytic reaction with CuInS<sub>2</sub>, such as photocatalytic CO<sub>2</sub> reduction and small molecule organic transformation, possible projects include:

1. Decorating CuInS<sub>2</sub> QDs with homogenous catalysts such as Co or Ni complexes to increase the quantum efficiency or encapsulating CuInS<sub>2</sub> QDs into porous materials to increase the recycling ability.
2. Investigating the photocatalytic condition of CO<sub>2</sub> reduction or small molecule transformation and understanding the fundamental mechanism during the photocatalytic process.

## **9.2 Conclusion and future work of zeolitic imidazolate frameworks (ZIFs)**

In this dissertation, the structural parameters that can affect the photophysical and photocatalytic properties of ZIFs have been studied in chapter 5 and chapter 6 while the communication between ZIFs and chromophore have been studied in chapter 7 and chapter 8.

In chapter 5, three imidazole-based linkers (2-methylimidazole, benzimidazole and 2-nitroimidazole) with different functional group on imidazole ring were used to synthesize Co-based ZIFs with SOD topology, i.e. ZIF-67, ZIF-9, and ZIF-65, respectively. ZIF-65 which has the strongest electron withdrawn group showed negligible ligand to metal charge transfer (LMCT) as confirmed by X-ray absorption spectroscopy and optical transient absorption spectroscopy (OTA) following 1200 nm excitation. In contrast, ZIF-65 have negligible OTA signal, which may be due to the low extinction coefficient at 1200 nm or very fast charge recombination rate which is beyond our laser resolution. ZIF-9 showed

much shorter charge separation (CS) state formation time (8.7 ps) than that in ZIF-67 (31.7 ps), suggesting faster charge transfer in ZIF-9. Under 350 nm excitation which excites LMCT band, the OTA results showed that the relaxation from LMCT to CS is less prominent in ZIF with stronger electron withdrawing ligand. Overall, the experimental results showed that the imidazole linker functionalized with different electron withdrawn group can affect the photophysical properties of Co-based ZIFs.

Inspired by the work in chapter 5, second imidazole linker (imidazole, Im) with different amount was introduced into ZIF-67 structure and the photocatalytic hydrogen generation reaction was investigated. The introduced Im has negligible impact on the crystal structure and Co local center which has been confirmed by the X-ray diffraction patterns and X-ray absorption spectra. The NMR and OTA results showed that the formation of the charge separation state is fastest after photoexcitation when the percentage of imidazole in ZIF-67 reaches 15%. The photocatalytic hydrogen generation activity of Im-ZIF-67 with Ru(bpy)<sub>3</sub>Cl<sub>2</sub> as the photosensitizer rshowed that the 15% imidazole doped ZIF-67 showed the highest hydrogen generation efficiency with almost 50% increase compared to that of ZIF-67 only. The study of the communication between Ru(bpy)<sub>3</sub>Cl<sub>2</sub> and ZIF-67 showed fastest electron transfer rate in 15% imidazole doping sample, which explains the highest hydrogen generation efficiency.

Chapter 7 and chapter 8 mainly discussed the energy transfer between ZIFs and chromophore. In chapter 7, atomic layer deposition (ALD) method was used to separate ZIF-67 and RuN<sub>3</sub> to study the distance effect on energy transfer efficiency. The distance between ZIF-67 and RuN<sub>3</sub> was controlled by tuning the thickness of the Al<sub>2</sub>O<sub>3</sub> layer which was controlled by the ALD cycles and deposited on the ZIF-67 film before sensitization of

RuN3. The Förster radius for this system was estimated to be 14.4 nm, which is much larger than many molecular donor/acceptor systems, suggesting the promise of enhancing light harvesting capability of ZIFs through ENT process. In order to enhance the energy transfer efficiency between ZIFs and chromophore, one strategy is to encapsulate chromophore in to ZIFs structures. Considering the pore size of ZIF-8, Rhodamine B (RB) was used as the organic dye and encapsulated into Co doped ZIF-8. Energy transfer was confirmed from RB to tetrahedral Co center by OTA and the energy transfer efficiency increased with the increasing concentration of Co center.

Despite these findings and progress made in the understanding of the photophysical and photocatalytic properties of ZIFs, this research area is still in its infancy particularly compared to the extensive ZIF research focusing on the molecular design and application in gas adsorption and separation. Further investigation on the photophysical and photocatalytic properties of ZIFs is certainly required and anticipated to address a few important questions:

- (1) What are the structural factors (e.g., metal nodes, ligands, topology, defect, and dimension) that control the formation and lifetime of the long-lived excited charge separated state?
- (2) How can the band structure and gap be tuned to facilitate charge separation and photocatalysis?
- (3) What strategies can be used to improve the carrier mobility in ZIFs?

To address these questions, the design and synthesis of ZIFs with a new structure, systematic photophysical characterization, and extensive theoretical support will have to

work together to develop an in-depth understanding of the structure–function relationships for photocatalysis. Given the critical advantage of ZIFs with structural and compositional diversity, one desirable research direction is to examine the dependence of photophysical and photocatalytic properties on the structure of bridging imidazolate linkers and the metal nodes. For example, in addition to the most commonly used nodes (e.g., Zn, Co, and Cu), ZIFs based on nickel, cadmium, and indium have been reported.<sup>253-256</sup> Owing to the different node-imidazolate and node-to-node interaction, ZIFs based on different metal nodes are expected to diverse the pore structure, surface area, topology, and coordination geometry, which are the important structural parameters that determine their photophysical properties and catalytic applications. On the other hand, a variety of imidazolate linkers are either commercially available or accessible by routine synthetic methods.<sup>195, 257</sup> It was found that substituents on the imidazolate linkers can not only impact the topology, the pore, and the aperture size but also the bandgap and position. We therefore expect such changes in ZIF frameworks to lead to vastly differing photophysical and photochemical properties. Consequently, future fundamental studies focusing on unraveling structural parameters that control photophysical properties of ZIFs would be essential to facilitate the optimal design of ZIF based materials for their photocatalytic applications.

## Reference

1. Gratzel, M., Artificial photosynthesis: water cleavage into hydrogen and oxygen by visible light. *Acc. Chem. Res.* **1981**, *14* (12), 376-384.
2. Fujita, E., Photochemical carbon dioxide reduction with metal complexes. *Coord. Chem. Rev.* **1999**, *185-6*, 373-384.
3. Yamazaki, Y.; Takeda, H.; Ishitani, O., Photocatalytic reduction of CO<sub>2</sub> using metal complexes. *Journal of Photochemistry and Photobiology C-Photochemistry Reviews* **2015**, *25*, 106-137.
4. Kamat, P. V., Meeting the clean energy demand: Nanostructure architectures for solar energy conversion. *J. Phys. Chem. C* **2007**, *111* (7), 2834-2860.
5. Liu, X.; Inagaki, S.; Gong, J. L., Heterogeneous Molecular Systems for Photocatalytic CO<sub>2</sub> Reduction with Water Oxidation. *Angew. Chem. Int. Ed.* **2016**, *55* (48), 14924-14950.
6. Gust, D.; Moore, T. A., Mimicking photosynthesis. *Science* **1989**, *244* (4900), 35-41.
7. Gust, D.; Moore, T. A.; Moore, A. L., Mimicking photosynthetic solar energy transduction. *Acc. Chem. Res.* **2001**, *34* (1), 40-48.
8. Bard, A. J.; Fox, M. A., ARTIFICIAL PHOTOSYNTHESIS - SOLAR SPLITTING OF WATER TO HYDROGEN AND OXYGEN. *Acc. Chem. Res.* **1995**, *28* (3), 141-145.
9. Yadav, R. K.; Baeg, J. O.; Oh, G. H.; Park, N. J.; Kong, K. J.; Kim, J.; Hwang, D. W.; Biswas, S. K., A Photocatalyst-Enzyme Coupled Artificial Photosynthesis System for Solar Energy in Production of Formic Acid from CO<sub>2</sub>. *J. Am. Chem. Soc.* **2012**, *134* (28), 11455-11461.
10. Tachibana, Y.; Vayssieres, L.; Durrant, J. R., Artificial photosynthesis for solar water-splitting. *Nat. Photonics* **2012**, *6* (8), 511-518.
11. Fujishima, A.; Honda, K., ELECTROCHEMICAL PHOTOLYSIS OF WATER AT A SEMICONDUCTOR ELECTRODE. *Nature* **1972**, *238* (5358), 37-38.
12. LaRoche, J.; vanderStaay, G. W. M.; Partensky, F.; Ducret, A.; Aebersold, R.; Li, R.; Golden, S. S.; Hiller, R. G.; Wrench, P. M.; Larkum, A. W. D.; Green, B. R., Independent evolution of the prochlorophyte and green plant chlorophyll a/b light-harvesting proteins. *Proc. Natl. Acad. Sci. U.S.A* **1996**, *93* (26), 15244-15248.

13. Dubinsky, Z.; Falkowski, P. G.; Wyman, K., LIGHT HARVESTING AND UTILIZATION BY PHYTOPLANKTON. *Plant and Cell Physiology* **1986**, *27* (7), 1335-1349.
14. Nazeeruddin, M. K.; Klein, C.; Liska, P.; Gratzel, M., Synthesis of novel ruthenium sensitizers and their application in dye-sensitized solar cells. *Coord. Chem. Rev.* **2005**, *249* (13-14), 1460-1467.
15. Hara, M.; Waraksa, C. C.; Lean, J. T.; Lewis, B. A.; Mallouk, T. E., Photocatalytic water oxidation in a buffered tris(2,2'-bipyridyl)ruthenium complex-colloidal IrO<sub>2</sub> system. *Journal of Physical Chemistry A* **2000**, *104* (22), 5275-5280.
16. Hoffmann, M. R.; Martin, S. T.; Choi, W. Y.; Bahnemann, D. W., ENVIRONMENTAL APPLICATIONS OF SEMICONDUCTOR PHOTOCATALYSIS. *Chem. Rev* **1995**, *95* (1), 69-96.
17. Alivisatos, A. P., Semiconductor clusters, nanocrystals, and quantum dots. *Science* **1996**, *271* (5251), 933-937.
18. El-Sayed, M. A., Small is different: Shape-, size-, and composition-dependent properties of some colloidal semiconductor nanocrystals. *Acc. Chem. Res.* **2004**, *37* (5), 326-333.
19. Wu, H. L.; Li, X. B.; Tung, C. H.; Wu, L. Z., Recent Advances in Sensitized Photocathodes: From Molecular Dyes to Semiconducting Quantum Dots. *Advanced Science* **2018**, *5* (4).
20. Ruberu, T. P. A.; Dong, Y. M.; Das, A.; Eisenberg, R., Photoelectrochemical Generation of Hydrogen from Water Using a CdSe Quantum Dot-Sensitized Photocathode. *ACS Catal.* **2015**, *5* (4), 2255-2259.
21. Kuehnel, M. F.; Orchard, K. L.; Dalle, K. E.; Reisner, E., Selective Photocatalytic CO<sub>2</sub> Reduction in Water through Anchoring of a Molecular Ni Catalyst on CdS Nanocrystals. *J. Am. Chem. Soc.* **2017**, *139* (21), 7217-7223.
22. Zhou, Y.; Yang, S.; Huang, J., Light-driven hydrogen production from aqueous solutions based on a new Dubois-type nickel catalyst. *Phys. Chem. Chem. Phys* **2017**, *19* (11), 7471-7475.
23. Kuehnel, M. F.; Sahm, C. D.; Neri, G.; Lee, J. R.; Orchard, K. L.; Cowan, A. J.; Reisner, E., ZnSe quantum dots modified with a Ni(cyclam) catalyst for efficient visible-light driven CO<sub>2</sub> reduction in water. *Chemical Science* **2018**, *9* (9), 2501-2509.
24. Allen, P. M.; Bawendi, M. G., Ternary I-III-VI quantum dots luminescent in the red to near-infrared. *J. Am. Chem. Soc.* **2008**, *130* (29), 9240-9241.

25. Xie, R. G.; Rutherford, M.; Peng, X. G., Formation of High-Quality I-III-VI Semiconductor Nanocrystals by Tuning Relative Reactivity of Cationic Precursors. *J. Am. Chem. Soc.* **2009**, *131* (15), 5691-5697.
26. Omata, T.; Nose, K.; Otsuka-Yao-Matsuo, S., Size dependent optical band gap of ternary I-III-VI<sub>2</sub> semiconductor nanocrystals. *Journal of Applied Physics* **2009**, *105* (7).
27. Kolny-Olesiak, J.; Weller, H., Synthesis and Application of Colloidal CuInS<sub>2</sub> Semiconductor Nanocrystals. *ACS Appl. Mater. Interfaces* **2013**, *5* (23), 12221-12237.
28. Chen, B. K.; Zhong, H. Z.; Wang, M. X.; Liu, R. B.; Zou, B. S., Integration of CuInS<sub>2</sub>-based nanocrystals for high efficiency and high colour rendering white light-emitting diodes. *Nanoscale* **2013**, *5* (8), 3514-3519.
29. Siemer, K.; Klaer, J.; Luck, I.; Bruns, J.; Klenk, R.; Braunig, D., Efficient CuInS<sub>2</sub> solar cells from a rapid thermal process (RTP). *Solar Energy Materials and Solar Cells* **2001**, *67* (1-4), 159-166.
30. Castro, S. L.; Bailey, S. G.; Raffaele, R. P.; Banger, K. K.; Hepp, A. F., Nanocrystalline chalcopyrite materials (CuInS<sub>2</sub> and CuInSe<sub>2</sub>) via low-temperature pyrolysis of molecular single-source precursors. *Chem. Mater.* **2003**, *15* (16), 3142-3147.
31. Regulacio, M. D.; Han, M. Y., Multinary I-III-VI<sub>2</sub> and I-2-II-IV-VI<sub>4</sub> Semiconductor Nanostructures for Photocatalytic Applications. *Acc. Chem. Res.* **2016**, *49* (3), 511-519.
32. Zheng, L.; Xu, Y.; Song, Y.; Wu, C. Z.; Zhang, M.; Xie, Y., Nearly Monodisperse CuInS<sub>2</sub> Hierarchical Microarchitectures for Photocatalytic H<sub>2</sub> Evolution under Visible Light. *Inorg. Chem.* **2009**, *48* (9), 4003-4009.
33. Scheer, R.; Walter, T.; Schock, H. W.; Fearheiley, M. L.; Lewerenz, H. J., CuInS<sub>2</sub> based thin film solar cell with 10.2% efficiency. *Appl. Phys. Lett.* **1993**, *63* (24), 3294-3296.
34. Soni, A.; Gupta, V.; Arora, C. M.; Dashora, A.; Ahuja, B. L., Electronic structure and optical properties of CuGaS<sub>2</sub> and CuInS<sub>2</sub> solar cell materials. *Solar Energy* **2010**, *84* (8), 1481-1489.
35. Zhong, H. Z.; Bai, Z. L.; Zou, B. S., Tuning the Luminescence Properties of Colloidal I-III-VI Semiconductor Nanocrystals for Optoelectronics and Biotechnology Applications. *J. Phys. Chem. Lett.* **2012**, *3* (21), 3167-3175.
36. Jara, D. H.; Stamplecoskie, K. G.; Kamat, P. V., Two Distinct Transitions in Cu<sub>x</sub>InS<sub>2</sub> Quantum Dots. Bandgap versus Sub-Bandgap Excitations in Copper-Deficient Structures. *J. Phys. Chem. Lett.* **2016**, *7* (8), 1452-1459.
37. Li, L. A.; Pandey, A.; Werder, D. J.; Khanal, B. P.; Pietryga, J. M.; Klimov, V. I., Efficient Synthesis of Highly Luminescent Copper Indium Sulfide-Based Core/Shell

Nanocrystals with Surprisingly Long-Lived Emission. *J. Am. Chem. Soc.* **2011**, *133* (5), 1176-1179.

38. Rincon, C.; Marquez, R., Defect physics of the CuInSe<sub>2</sub> chalcopyrite semiconductor. *J. Phys. Chem. Solids* **1999**, *60* (11), 1865-1873.

39. Chen, B. K.; Zhong, H. Z.; Zhang, W. Q.; Tan, Z. A.; Li, Y. F.; Yu, C. R.; Zhai, T. Y.; Bando, Y. S.; Yang, S. Y.; Zou, B. S., Highly Emissive and Color-Tunable CuInS<sub>2</sub>-Based Colloidal Semiconductor Nanocrystals: Off-Stoichiometry Effects and Improved Electroluminescence Performance. *Advanced Functional Materials* **2012**, *22* (10), 2081-2088.

40. Binsma, J. J. M.; Giling, L. J.; Bloem, J., LUMINESCENCE OF CUINS<sub>2</sub> .1. THE BROAD-BAND EMISSION AND ITS DEPENDENCE ON THE DEFECT CHEMISTRY. *Journal of Luminescence* **1982**, *27* (1), 35-53.

41. Chen, X. B.; Shen, S. H.; Guo, L. J.; Mao, S. S., Semiconductor-based Photocatalytic Hydrogen Generation. *Chem. Rev* **2010**, *110* (11), 6503-6570.

42. Lehn, J. M.; Sauvage, J. P., CHEMICAL STORAGE OF LIGHT ENERGY - CATALYTIC GENERATION OF HYDROGEN BY VISIBLE-LIGHT OR SUNLIGHT - IRRADIATION OF NEUTRAL AQUEOUS-SOLUTIONS. *Nouveau Journal De Chimie-New Journal of Chemistry* **1977**, *1* (6), 449-451.

43. Han, Z. J.; Qiu, F.; Eisenberg, R.; Holland, P. L.; Krauss, T. D., Robust Photogeneration of H<sub>2</sub> in Water Using Semiconductor Nanocrystals and a Nickel Catalyst. *Science* **2012**, *338* (6112), 1321-1324.

44. Qiu, F.; Han, Z. J.; Peterson, J. J.; Odoi, M. Y.; Sowers, K. L.; Krauss, T. D., Photocatalytic Hydrogen Generation by CdSe/CdS Nanoparticles. *Nano Lett.* **2016**, *16* (9), 5347-5352.

45. Wu, K. F.; Zhu, H. M.; Liu, Z.; Rodriguez-Cordoba, W.; Lian, T. Q., Ultrafast Charge Separation and Long-Lived Charge Separated State in Photocatalytic CdS-Pt Nanorod Heterostructures. *J. Am. Chem. Soc.* **2012**, *134* (25), 10337-10340.

46. Huang, J.; Mulfort, K. L.; Du, P. W.; Chen, L. X., Photodriven Charge Separation Dynamics in CdSe/ZnS Core/Shell Quantum Dot/Cobaloxime Hybrid for Efficient Hydrogen Production. *J. Am. Chem. Soc.* **2012**, *134* (40), 16472-16475.

47. Sasan, K.; Lin, Q. P.; Mao, C. Y.; Feng, P. Y., Incorporation of iron hydrogenase active sites into a highly stable metal-organic framework for photocatalytic hydrogen generation. *ChemComm* **2014**, *50* (72), 10390-10393.

48. Yu, J. G.; Qi, L. F.; Jaroniec, M., Hydrogen Production by Photocatalytic Water Splitting over Pt/TiO<sub>2</sub> Nanosheets with Exposed (001) Facets. *J. Phys. Chem. C* **2010**, *114* (30), 13118-13125.

49. Hardman, R., A toxicologic review of quantum dots: Toxicity depends on physicochemical and environmental factors. *Environmental Health Perspectives* **2006**, *114* (2), 165-172.
50. Yuan, J. L.; Hao, C. J., Solar-driven photoelectrochemical reduction of carbon dioxide to methanol at CuInS<sub>2</sub> thin film photocathode. *Solar Energy Materials and Solar Cells* **2013**, *108*, 170-174.
51. Cherfouh, H.; Fellahi, O.; Hadjersi, T.; Marsan, B., CuInS<sub>2</sub>/SiNWs/Si composite material for application as potential photoelectrode for photoelectrochemical hydrogen generation. *International Journal of Hydrogen Energy* **2018**, *43* (6), 3431-3440.
52. Phan, A.; Doonan, C. J.; Uribe-Romo, F. J.; Knobler, C. B.; O'Keeffe, M.; Yaghi, O. M., Synthesis, Structure, and Carbon Dioxide Capture Properties of Zeolitic Imidazolate Frameworks. *Acc. Chem. Res.* **2010**, *43* (1), 58-67.
53. Pimentel, B. R.; Parulkar, A.; Zhou, E. K.; Brunelli, N. A.; Lively, R. P., Zeolitic Imidazolate Frameworks: Next-Generation Materials for Energy-Efficient Gas Separations. *ChemSusChem* **2014**, *7* (12), 3202-3240.
54. Chen, B. L.; Yang, Z. X.; Zhu, Y. Q.; Xia, Y. D., Zeolitic imidazolate framework materials: recent progress in synthesis and applications. *J. Mater. Chem. A* **2014**, *2* (40), 16811-16831.
55. Hayashi, H.; Cote, A. P.; Furukawa, H.; O'Keeffe, M.; Yaghi, O. M., Zeolite a imidazolate frameworks. *Nat. Mater.* **2007**, *6* (7), 501-506.
56. Beldon, P. J.; Fabian, L.; Stein, R. S.; Thirumurugan, A.; Cheetham, A. K.; Friscic, T., Rapid Room-Temperature Synthesis of Zeolitic Imidazolate Frameworks by Using Mechanochemistry. *Angew. Chem. Int. Ed.* **2010**, *49* (50), 9640-9643.
57. Tian, Y. Q.; Chen, Z. X.; Weng, L. H.; Guo, H. B.; Gao, S.; Zhao, D. Y., Two polymorphs of cobalt(II) imidazolate polymers synthesized solvothermally by using one organic template N,N-dimethylacetamide. *Inorg. Chem.* **2004**, *43* (15), 4631-4635.
58. Wang, X.; Yu, L.; Guan, B. Y.; Song, S. Y.; Lou, X. W., Metal-Organic Framework Hybrid-Assisted Formation of Co<sub>3</sub>O<sub>4</sub>/Co-Fe Oxide Double-Shelled Nanoboxes for Enhanced Oxygen Evolution. *Adv. Mater.* **2018**, *30* (29).
59. Zheng, G.; Chen, Z.; Sentosun, K.; Perez-Juste, I.; Bals, S.; Liz-Marzan, L. M.; Pastoriza-Santos, I.; Perez-Juste, J.; Hong, M., Shape control in ZIF-8 nanocrystals and metal nanoparticles@ZIF-8 heterostructures. *Nanoscale* **2017**, *9* (43), 16645-16651.
60. Khay, I.; Chaplais, G.; Nouali, H.; Marichal, C.; Patarin, J., Water intrusion-extrusion experiments in ZIF-8: impacts of the shape and particle size on the energetic performances. *RSC Adv.* **2015**, *5* (40), 31514-31518.

61. Tanaka, S.; Kida, K.; Okita, M.; Ito, Y.; Miyake, Y., Size-controlled Synthesis of Zeolitic Imidazolate Framework-8 (ZIF-8) Crystals in an Aqueous System at Room Temperature. *Chem. Lett.* **2012**, *41* (10), 1337-1339.
62. Banerjee, R.; Furukawa, H.; Britt, D.; Knobler, C.; O'Keeffe, M.; Yaghi, O. M., Control of Pore Size and Functionality in Isoreticular Zeolitic Imidazolate Frameworks and their Carbon Dioxide Selective Capture Properties. *J. Am. Chem. Soc.* **2009**, *131* (11), 3875-3877.
63. Zhang, J. C.; Zhang, T. C.; Xiao, K. S.; Cheng, S.; Qian, G.; Wang, Y.; Feng, Y., Novel and Facile Strategy for Controllable Synthesis of Multilayered Core-Shell Zeolitic Imidazolate Frameworks. *Cryst. Growth Des.* **2016**, *16* (11), 6494-6498.
64. Hillman, F.; Zimmerman, J. M.; Paek, S. M.; Hamid, M. R. A.; Lim, W. T.; Jeong, H. K., Rapid microwave-assisted synthesis of hybrid zeolitic-imidazolate frameworks with mixed metals and mixed linkers. *J. Mater. Chem. A* **2017**, *5* (13), 6090-6099.
65. Thompson, J. A.; Brunelli, N. A.; Lively, R. P.; Johnson, J. R.; Jones, C. W.; Nair, S., Tunable CO<sub>2</sub> Adsorbents by Mixed-Linker Synthesis and Postsynthetic Modification of Zeolitic Imidazolate Frameworks. *J. Phys. Chem. C* **2013**, *117* (16), 8198-8207.
66. Yang, J. J.; Zhang, Y. B.; Liu, Q.; Trickett, C. A.; Gutierrez-Puebla, E.; Monge, M. A.; Cong, H. J.; Aldossary, A.; Deng, H. X.; Yaghi, O. M., Principles of Designing Extra-Large Pore Openings and Cages in Zeolitic Imidazolate Frameworks. *J. Am. Chem. Soc.* **2017**, *139* (18), 6448-6455.
67. Moggach, S. A.; Bennett, T. D.; Cheetham, A. K., The Effect of Pressure on ZIF-8: Increasing Pore Size with Pressure and the Formation of a High-Pressure Phase at 1.47 GPa. *Angew. Chem. Int. Ed.* **2009**, *48* (38), 7087-7089.
68. Liu, X. Y.; Li, Y.; Tsung, C. K.; Li, J., Encapsulation of yellow phosphors into nanocrystalline metal-organic frameworks for blue-excitable white light emission. *ChemComm* **2019**, *55* (72), 10669-10672.
69. Liu, X. Y.; Xing, K.; Li, Y.; Tsung, C. K.; Li, J., Three Models To Encapsulate Multicomponent Dyes into Nanocrystal Pores: A New Strategy for Generating High-Quality White Light. *J. Am. Chem. Soc.* **2019**, *141* (37), 14807-14813.
70. Chen, Y. F.; Yu, B.; Cui, Y. D.; Xu, S. J.; Gong, J. B., Core-Shell Structured Cyclodextrin Metal-Organic Frameworks with Hierarchical Dye Encapsulation for Tunable Light Emission. *Chem. Mater.* **2019**, *31* (4), 1289-1295.
71. Luo, Y. C.; Chu, K. L.; Shi, J. Y.; Wu, D. J.; Wang, X. D.; Mayor, M.; Su, C. Y., Heterogenization of Photochemical Molecular Devices: Embedding a Metal-Organic Cage into a ZIF-8-Derived Matrix To Promote Proton and Electron Transfer. *J. Am. Chem. Soc.* **2019**, *141* (33), 13057-13065.

72. Mukhopadhyay, S.; Basu, O.; Das, S. K., ZIF-8 MOF Encapsulated Co-porphyrin, an Efficient Electrocatalyst for Water Oxidation in a Wide pH Range: Works Better at Neutral pH. *ChemCatChem* **2020**, *12* (21), 5430-5438.
73. Ye, J. W.; Zhou, H. L.; Liu, S. Y.; Cheng, X. N.; Lin, R. B.; Qj, X. L.; Zhang, J. P.; Chen, X. M., Encapsulating Pyrene in a Metal-Organic Zeolite for Optical Sensing of Molecular Oxygen. *Chem. Mater.* **2015**, *27* (24), 8255-8260.
74. Rong, H. Q.; Zhan, T. R.; Sun, Y.; Wen, Y. H.; Liu, X. E.; Teng, H. N., ZIF-8 derived nitrogen, phosphorus and sulfur tri-doped mesoporous carbon for boosting electrocatalysis to oxygen reduction in universal pH range. *Electrochim. Acta* **2019**, *318*, 783-793.
75. Gu, J. X.; Zhao, X.; Sun, Y.; Zhou, J.; Sun, C. Y.; Wang, X. L.; Kang, Z. H.; Su, Z. M., A photo-activated process cascaded electrocatalysis for the highly efficient CO(2)reduction over a core-shell ZIF-8@Co/C. *J. Mater. Chem. A* **2020**, *8* (32), 16616-16623.
76. Cheng, N. Y.; Ren, L.; Xu, X.; Du, Y.; Dou, S. X., Recent Development of Zeolitic Imidazolate Frameworks (ZIFs) Derived Porous Carbon Based Materials as Electrocatalysts. *Adv. Energy Mater.* **2018**, *8* (25).
77. Dou, S.; Li, X. Y.; Tao, L.; Huo, J.; Wang, S. Y., Cobalt nanoparticle-embedded carbon nanotube/porous carbon hybrid derived from MOF-encapsulated Co<sub>3</sub>O<sub>4</sub> for oxygen electrocatalysis. *ChemComm* **2016**, *52* (62), 9727-9730.
78. Lan, M.; Guo, R. M.; Dou, Y. B.; Zhou, J.; Zhou, A.; Li, J. R., Fabrication of porous Pt-doping heterojunctions by using bimetallic MOF template for photocatalytic hydrogen generation. *Nano Energy* **2017**, *33*, 238-246.
79. Feng, Y.; Lu, H. G.; Gu, X. L.; Qiu, J. H.; Jia, M. M.; Huang, C. B.; Yao, J. F., ZIF-8 derived porous N-doped ZnO with enhanced visible light-driven photo catalytic activity. *J. Phys. Chem. Solids* **2017**, *102*, 110-114.
80. Liu, D. N.; Chen, D. Y.; Li, N. J.; Xu, Q. F.; Li, H.; He, J. H.; Lu, J. M., ZIF-67-Derived 3D Hollow Mesoporous Crystalline Co<sub>3</sub>O<sub>4</sub> Wrapped by 2D g-C<sub>3</sub>N<sub>4</sub> Nanosheets for Photocatalytic Removal of Nitric Oxide. *Small* **2019**, *15* (31), 1902291.
81. Zhou, X. J.; Tian, J.; Hu, J. L.; Li, C. L., High Rate Magnesium-Sulfur Battery with Improved Cyclability Based on Metal-Organic Framework Derivative Carbon Host. *Adv. Mater.* **2018**, *30* (7).
82. Li, J.; Lu, S. Q.; Huang, H. L.; Liu, D. H.; Zhuang, Z. B.; Zhong, C. L., ZIF-67 as Continuous Self-Sacrifice Template Derived NiCo<sub>2</sub>O<sub>4</sub>/Co,N-CNTs Nanocages as Efficient Bifunctional Electrocatalysts for Rechargeable Zn-Air Batteries. *ACS Sustain. Chem. Eng.* **2018**, *6* (8), 10021-10029.

83. Guan, J.; Zhong, X. W.; Chen, X.; Zhu, X. J.; Li, P. L.; Wu, J. H.; Lu, Y. L.; Yu, Y.; Yang, S. F., Expanding pore sizes of ZIF-8-derived nitrogen-doped microporous carbon via C-60 embedding: toward improved anode performance for the lithium-ion battery. *Nanoscale* **2018**, *10* (5), 2473-2480.
84. Zhou, J. J.; Han, X.; Tao, K.; Li, Q.; Li, Y. L.; Chen, C.; Han, L., Shish-kebab type MnCo<sub>2</sub>O<sub>4</sub>@Co<sub>3</sub>O<sub>4</sub> nanoneedle arrays derived from MnCo-LDH@ZIF-67 for high-performance supercapacitors and efficient oxygen evolution reaction. *Chem. Eng. J.* **2018**, *354*, 875-884.
85. Jian, S. L.; Hsiao, L. Y.; Yeh, M. H.; Ho, K. C., Designing a carbon nanotubes-interconnected ZIF-derived cobalt sulfide hybrid nanocage for supercapacitors. *J. Mater. Chem. A* **2019**, *7* (4), 1479-1490.
86. Wan, L.; Shamsaei, E.; Easton, C. D.; Yu, D. B.; Liang, Y.; Chen, X. F.; Abbasi, Z.; Akbari, A.; Zhang, X. W.; Wang, H. T., ZIF-8 derived nitrogen-doped porous carbon/carbon nanotube composite for high-performance supercapacitor. *Carbon* **2017**, *121*, 330-336.
87. Cao, J.; Yang, Z. H.; Xiong, W. P.; Zhou, Y. Y.; Peng, Y. R.; Li, X.; Zhou, C. Y.; Xu, R.; Zhang, Y. R., One-step synthesis of Co-doped UiO-66 nanoparticle with enhanced removal efficiency of tetracycline: Simultaneous adsorption and photocatalysis. *Chem. Eng. J.* **2018**, *353*, 126-137.
88. He, J.; Wang, J. Q.; Chen, Y. J.; Zhang, J. P.; Duan, D. L.; Wang, Y.; Yan, Z. Y., A dye-sensitized Pt@UiO-66(Zr) metal-organic framework for visible-light photocatalytic hydrogen production. *ChemComm* **2014**, *50* (53), 7063-7066.
89. Voskuilen, T. G.; Pourpoint, T. L.; Dailly, A. M., Hydrogen adsorption on microporous materials at ambient temperatures and pressures up to 50 MPa. *Adsorption* **2012**, *18* (3-4), 239-249.
90. Lin, R. B.; Li, S. M.; Wang, J. Y.; Xu, J. P.; Xu, C. H.; Wang, J.; Li, C. X.; Li, Z. Q., Facile generation of carbon quantum dots in MIL-53(Fe) particles as localized electron acceptors for enhancing their photocatalytic Cr(vi) reduction. *Inorg. Chem. Front.* **2018**, *5* (12), 3170-3177.
91. Zhang, F. Y.; Zhang, B. X.; Feng, J. Q.; Tan, X. N.; Liu, L.; Liu, L. F.; Han, B. X.; Zheng, L. R.; Zhang, J.; Tai, J.; Zhang, J. L., Highly Mesoporous Ru-MIL-125-NH<sub>2</sub> Produced by Supercritical Fluid for Efficient Photocatalytic Hydrogen Production. *ACS Appl. Energy Mater.* **2019**, *2* (7), 4964-4970.
92. Li, R.; Zhang, W.; Zhou, K., Metal-Organic-Framework-Based Catalysts for Photoreduction of CO<sub>2</sub>. *Adv. Mater.* **2018**, *30* (35).
93. Hu, P.; Zhuang, J.; Chou, L. Y.; Lee, H. K.; Ling, X. Y.; Chuang, Y. C.; Tsung, C. K., Surfactant-Directed Atomic to Mesoscale Alignment: Metal Nanocrystals Encased

Individually in Single-Crystalline Porous Nanostructures. *J. Am. Chem. Soc.* **2014**, *136* (30), 10561-10564.

94. Corma, A.; Garcia, H., Zeolite-based photocatalysts. *ChemComm* **2004**, (13), 1443-1459.

95. Pattengale, B.; Yang, S. Z.; Ludwig, J.; Huang, Z. Q.; Zhang, X. Y.; Huang, J., Exceptionally Long-Lived Charge Separated State in Zeolitic Imidazolate Framework: Implication for Photocatalytic Applications. *J. Am. Chem. Soc.* **2016**, *138* (26), 8072-8075.

96. Yumashev, K. V.; Denisov, I. A.; Posnov, N. N.; Kuleshov, N. V.; Moncorge, R., Excited state absorption and passive Q-switch performance of Co<sup>2+</sup> doped oxide crystals. *J. Alloys Compd.* **2002**, *341* (1-2), 366-370.

97. Trujillano, R.; Lambert, J. F.; Louis, C., Chemistry of Silica-Supported Cobalt Catalysts Prepared by Cation Adsorption. 2. Neof ormation of Cobalt Phyllosilicate. *J. Phys. Chem. C* **2008**, *112* (47), 18551-18558.

98. Zhu, H. M.; Song, N. H.; Lian, T. Q., Wave Function Engineering for Ultrafast Charge Separation and Slow Charge Recombination in Type II Core/Shell Quantum Dots. *J. Am. Chem. Soc.* **2011**, *133* (22), 8762-8771.

99. Hewa-Kasakarage, N. N.; El-Khoury, P. Z.; Schmall, N.; Kirsanova, M.; Nemchinov, A.; Tarnovsky, A. N.; Bezryadin, A.; Zamkov, M., The effect of dielectric friction on the rate of charge separation in type II ZnSe/CdS semiconductor nanorods. *Appl. Phys. Lett.* **2009**, *94* (13).

100. Kumar, S.; Jones, M.; Lo, S. S.; Scholes, G. D., Nanorod heterostructures showing photoinduced charge separation. *Small* **2007**, *3* (9), 1633-1639.

101. She, C. X.; Demortiere, A.; Shevchenko, E. V.; Pelton, M., Using Shape to Control Photoluminescence from CdSe/CdS Core/Shell Nanorods. *J. Phys. Chem. Lett.* **2011**, *2* (12), 1469-1475.

102. Zhu, H. M.; Song, N. H.; Lian, T. Q., Controlling Charge Separation and Recombination Rates in CdSe/ZnS Type I Core-Shell Quantum Dots by Shell Thicknesses. *J. Am. Chem. Soc.* **2010**, *132* (42), 15038-15045.

103. Dooley, C. J.; Dimitrov, S. D.; Fiebig, T., Ultrafast electron transfer dynamics in CdSe/CdTe donor-acceptor nanorods. *J. Phys. Chem. C* **2008**, *112* (32), 12074-12076.

104. Bakulin, A. A.; Rao, A.; Pavelyev, V. G.; van Loosdrecht, P. H. M.; Pshenichnikov, M. S.; Niedzialek, D.; Cornil, J.; Beljonne, D.; Friend, R. H., The Role of Driving Energy and Delocalized States for Charge Separation in Organic Semiconductors. *Science* **2012**, *335* (6074), 1340-1344.

105. Caruso, D.; Troisi, A., Long-range exciton dissociation in organic solar cells. *Proc. Natl. Acad. Sci. U.S.A* **2012**, *109* (34), 13498-13502.

106. Coffey, D. C.; Ferguson, A. J.; Kopidakis, N.; Rumbles, G., Photovoltaic Charge Generation in Organic Semiconductors Based on Long-Range Energy Transfer. *ACS Nano* **2010**, *4* (9), 5437-5445.
107. Li, W.; Li, Y.; Zhang, W.; Yin, D.; Cheng, Y.; Chu, W.; Hu, M., Size-controlled flow synthesis of metal-organic frameworks crystals monitored by in-situ ultraviolet-visible absorption spectroscopy. *Chin. Chem. Lett.* **2020**, <https://doi.org/10.1016/j.ccl.2020.09.039>.
108. Butler, K. T.; Worrall, S. D.; Molloy, C. D.; Hendon, C. H.; Attfield, M. P.; Dryfe, R. A. W.; Walsh, A., Electronic structure design for nanoporous, electrically conductive zeolitic imidazolate frameworks. *J. Mater. Chem. C* **2017**, *5* (31), 7726-7731.
109. Butler, K. T.; Hendon, C. H.; Walsh, A., Electronic Structure Modulation of Metal-Organic Frameworks for Hybrid Devices. *ACS Appl. Mater. Interfaces* **2014**, *6* (24), 22044-22050.
110. Butler, K. T.; Hendon, C. H.; Walsh, A., Electronic Chemical Potentials of Porous Metal-Organic Frameworks. *J. Am. Chem. Soc.* **2014**, *136* (7), 2703-2706.
111. Sun, L.; Campbell, M. G.; Dinca, M., Electrically Conductive Porous Metal-Organic Frameworks. *Angew. Chem. Int. Ed.* **2016**, *55* (11), 3566-3579.
112. Grau-Crespo, R.; Aziz, A.; Collins, A. W.; Crespo-Otero, R.; Hernandez, N. C.; Rodriguez-Albelo, L. M.; Ruiz-Salvador, A. R.; Calero, S.; Hamad, S., Modelling a Linker Mix-and-Match Approach for Controlling the Optical Excitation Gaps and Band Alignment of Zeolitic Imidazolate Frameworks. *Angew. Chem. Int. Ed.* **2016**, *55* (52), 16012-16016.
113. Pattengale, B.; SantaLucia, D. J.; Yang, S. Z.; Hu, W. H.; Liu, C. M.; Zhang, X. Y.; Berry, J. F.; Huang, J., Direct Observation of Node-to-Node Communication in Zeolitic Imidazolate Frameworks. *J. Am. Chem. Soc.* **2018**, *140* (37), 11573-11576.
114. Carlin, R., Magnetochemistry. Springer-Verlag, Berlin, New York: 1986.
115. Wang, S. B.; Yao, W. S.; Lin, J. L.; Ding, Z. X.; Wang, X. C., Cobalt Imidazolate Metal-Organic Frameworks Photosplit CO<sub>2</sub> under Mild Reaction Conditions. *Angew. Chem. Int. Ed.* **2014**, *53* (4), 1034-1038.
116. Qin, J. N.; Wang, S. B.; Wang, X. C., Visible-light reduction CO<sub>2</sub> with dodecahedral zeolitic imidazolate framework ZIF-67 as an efficient co-catalyst. *Appl. Catal. B-Environ.* **2017**, *209*, 476-482.
117. Pattengale, B.; Yang, S. Z.; Lee, S.; Huang, J., Mechanistic Probes of Zeolitic Imidazolate Framework for Photocatalytic Application. *ACS Catal.* **2017**, *7* (12), 8446-8453.

118. Wang, M.; Liu, J. X.; Guo, C. M.; Gao, X. S.; Gong, C. H.; Wang, Y.; Liu, B.; Li, X. X.; Gurzadyan, G. G.; Sun, L. C., Metal-organic frameworks (ZIF-67) as efficient cocatalysts for photocatalytic reduction of CO<sub>2</sub>: the role of the morphology effect. *J. Mater. Chem. A* **2018**, *6* (11), 4768-4775.
119. Wang, S. B.; Wang, X. C., Photocatalytic CO<sub>2</sub> reduction by CdS promoted with a zeolitic imidazolate framework. *Appl. Catal. B-Environ.* **2015**, *162*, 494-500.
120. Kong, Z. C.; Liao, J. F.; Dong, Y. J.; Xu, Y. F.; Chen, H. Y.; Kuang, D. B.; Su, C. Y., Core@Shell CsPbBr<sub>3</sub>@Zeolitic Imidazolate Framework Nanocomposite for Efficient Photocatalytic CO<sub>2</sub> Reduction. *ACS Energy Lett.* **2018**, *3* (11), 2656-2662.
121. Shen, D. L.; Pang, A. Y.; Li, Y. F.; Dou, J.; Wei, M. D., Metal-organic frameworks at interfaces of hybrid perovskite solar cells for enhanced photovoltaic properties. *ChemComm* **2018**, *54* (10), 1253-1256.
122. Ahmadian-Yazdi, M. R.; Gholampour, N.; Eslamian, M., Interface Engineering by Employing Zeolitic Imidazolate Framework-8 (ZIF-8) as the Only Scaffold in the Architecture of Perovskite Solar Cells. *ACS Appl. Energy Mater.* **2020**, *3* (4), 3134-3143.
123. Murray, C. B.; Norris, D. J.; Bawendi, M. G., SYNTHESIS AND CHARACTERIZATION OF NEARLY MONODISPERSE CDE (E = S, SE, TE) SEMICONDUCTOR NANOCRYSTALLITES. *J. Am. Chem. Soc.* **1993**, *115* (19), 8706-8715.
124. Yang, S. Z.; Pattengale, B.; Kovrigin, E. L.; Huang, J., Photoactive Zeolitic Imidazolate Framework as Intrinsic Heterogeneous Catalysts for Light-Driven Hydrogen Generation. *ACS Energy Lett.* **2017**, *2* (1), 75-80.
125. Ozturk, Z.; Hofmann, J. P.; Lutz, M.; Mazaj, M.; Logar, N. Z.; Weckhuysen, B. M., Controlled Synthesis of Phase-Pure Zeolitic Imidazolate Framework Co-ZIF-9. *Eur. J. Inorg. Chem.* **2015**, (9), 1625-1630.
126. Orsi, A.; Price, D. J.; Kahr, J.; Pillai, R. S.; Sneddon, S.; Cao, S.; Benoit, V.; Lozinska, M. M.; Cordes, D. B.; Slawin, A. M. Z.; Llewellyn, P. L.; Casely, I.; Ashbrook, S. E.; Maurin, G.; Wright, P. A., Porous zinc and cobalt 2-nitroimidazolate frameworks with six-membered ring windows and a layered cobalt 2-nitroimidazolate polymorph. *CrystEngComm* **2017**, *19* (10), 1377-1388.
127. Talapin, D. V.; Lee, J. S.; Kovalenko, M. V.; Shevchenko, E. V., Prospects of Colloidal Nanocrystals for Electronic and Optoelectronic Applications. *Chem. Rev* **2010**, *110* (1), 389-458.
128. Kamat, P. V., Quantum Dot Solar Cells. Semiconductor Nanocrystals as Light Harvesters. *J. Phys. Chem. C* **2008**, *112* (48), 18737-18753.
129. Scholes, G. D., Controlling the optical properties of inorganic nanoparticles. *Advanced Functional Materials* **2008**, *18* (8), 1157-1172.

130. Bruchez, M.; Moronne, M.; Gin, P.; Weiss, S.; Alivisatos, A. P., Semiconductor nanocrystals as fluorescent biological labels. *Science* **1998**, *281* (5385), 2013-2016.
131. Klimov, V. I.; Ivanov, S. A.; Nanda, J.; Achermann, M.; Bezel, I.; McGuire, J. A.; Piryatinski, A., Single-exciton optical gain in semiconductor nanocrystals. *Nature* **2007**, *447* (7143), 441-446.
132. Zhu, H. M.; Song, N. H.; Rodriguez-Cordoba, W.; Lian, T. Q., Wave Function Engineering for Efficient Extraction of up to Nineteen Electrons from One CdSe/CdS Quasi-Type II Quantum Dot. *J. Am. Chem. Soc.* **2012**, *134* (9), 4250-4257.
133. Chirila, A.; Reinhard, P.; Pianezzi, F.; Bloesch, P.; Uhl, A. R.; Fella, C.; Kranz, L.; Keller, D.; Gretener, C.; Hagendorfer, H.; Jaeger, D.; Erni, R.; Nishiwaki, S.; Buecheler, S.; Tiwari, A. N., Potassium-induced surface modification of Cu(In,Ga)Se-2 thin films for high-efficiency solar cells. *Nat. Mater.* **2013**, *12* (12), 1107-1111.
134. Weil, B. D.; Connor, S. T.; Cui, Y., CuInS<sub>2</sub> Solar Cells by Air-Stable Ink Rolling. *J. Am. Chem. Soc.* **2010**, *132* (19), 6642-6643.
135. Li, T. L.; Teng, H. S., Solution synthesis of high-quality CuInS<sub>2</sub> quantum dots as sensitizers for TiO<sub>2</sub> photoelectrodes. *J. Mater. Chem* **2010**, *20* (18), 3656-3664.
136. Zhong, H. Z.; Lo, S. S.; Mirkovic, T.; Li, Y. C.; Ding, Y. Q.; Li, Y. F.; Scholes, G. D., Noninjection Gram-Scale Synthesis of Monodisperse Pyramidal CuInS<sub>2</sub> Nanocrystals and Their Size-Dependent Properties. *ACS Nano* **2010**, *4* (9), 5253-5262.
137. Sandroni, M.; Wegner, K. D.; Aldakov, D.; Reiss, P., Prospects of Chalcopyrite-Type Nanocrystals for Energy Applications. *ACS Energy Lett.* **2017**, *2* (5), 1076-1088.
138. Castro, S. L.; Bailey, S. G.; Raffaele, R. P.; Banger, K. K.; Hepp, A. F., Synthesis and characterization of colloidal CuInS<sub>2</sub> nanoparticles from a molecular single-source precursor. *J. Phys. Chem. B* **2004**, *108* (33), 12429-12435.
139. Wang, X.; Liang, Z. R.; Xu, X. Q.; Wang, N.; Fang, J.; Wang, J. X.; Xu, G., A high efficient photoluminescence Zn-Cu-In-S/ZnS quantum dots with long lifetime. *J. Alloys Compd.* **2015**, *640*, 134-140.
140. Leach, A. D. P.; Macdonald, J. E., Optoelectronic Properties of CuInS<sub>2</sub> Nanocrystals and Their Origin. *J. Phys. Chem. Lett.* **2016**, *7* (3), 572-583.
141. Bose, R.; Ahmed, G. H.; Alarousu, E.; Parida, M. R.; Abdelhady, A. L.; Bakr, O. M.; Mohammed, O. F., Direct Femtosecond Observation of Charge Carrier Recombination in Ternary Semiconductor Nanocrystals: The Effect of Composition and Shelling. *J. Phys. Chem. C* **2015**, *119* (6), 3439-3446.
142. Nam, D. E.; Song, W. S.; Yang, H., Facile, air-insensitive solvothermal synthesis of emission-tunable CuInS<sub>2</sub>/ZnS quantum dots with high quantum yields. *J. Mater. Chem* **2011**, *21* (45), 18220-18226.

143. Zhong, H. Z.; Zhou, Y.; Ye, M. F.; He, Y. J.; Ye, J. P.; He, C.; Yang, C. H.; Li, Y. F., Controlled Synthesis and Optical Properties of Colloidal Ternary Chalcogenide CuInS<sub>2</sub> Nanocrystals. *Chem. Mater.* **2008**, *20* (20), 6434-6443.
144. Debnath, T.; Maiti, S.; Maity, P.; Ghosh, H. N., Subpicosecond Exciton Dynamics and Biexcitonic Feature in Colloidal CuInS<sub>2</sub> Nanocrystals: Role of In-Cu Antisite Defects. *J. Phys. Chem. Lett.* **2015**, *6* (17), 3458-3465.
145. Halpert, J. E.; Morgenstern, F. S. F.; Ehrler, B.; Vaynzof, Y.; Credgington, D.; Greenham, N. C., Charge Dynamics in Solution-Processed Nanocrystalline CuInS<sub>2</sub> Solar Cells. *ACS Nano* **2015**, *9* (6), 5857-5867.
146. Panthani, M. G.; Akhavan, V.; Goodfellow, B.; Schmidtke, J. P.; Dunn, L.; Dodabalapur, A.; Barbara, P. F.; Korgel, B. A., Synthesis of CuInS<sub>2</sub>, CuInSe<sub>2</sub>, and Cu(In<sub>x</sub>Ga<sub>1-x</sub>)Se<sub>2</sub> (CIGS) Nanocrystal "Inks" for Printable Photovoltaics. *J. Am. Chem. Soc.* **2008**, *130* (49), 16770-16777.
147. Zhou, Y. L.; Hu, W. H.; Ludwig, J.; Huang, J., Exceptionally Robust CuInS<sub>2</sub>/ZnS Nanoparticles as Single Component Photocatalysts for H<sub>2</sub> Evolution. *J. Phys. Chem. C* **2017**, *121* (35), 19031-19035.
148. Jara, D. H.; Yoon, S. J.; Stamplecoskie, K. G.; Kamat, P. V., Size-Dependent Photovoltaic Performance of CuInS<sub>2</sub> Quantum Dot-Sensitized Solar Cells. *Chem. Mater.* **2014**, *26* (24), 7221-7228.
149. Tang, Y.; Pattengale, B.; Ludwig, J.; Atifi, A.; Zinovev, A. V.; Dong, B.; Kong, Q. Y.; Zuo, X. B.; Zhang, X. Y.; Huang, J., Direct Observation of Photoinduced Charge Separation in Ruthenium Complex/Ni(OH)<sub>2</sub> Nanoparticle Hybrid. *Sci. Rep.* **2015**, *5*.
150. Ho, C. H., Temperature Dependent Crystal-Field Splitting and Band-Edge Characteristic in Cu(Al<sub>x</sub>In<sub>1-x</sub>)S<sub>2</sub> (0 ≤ x ≤ 1) Series Solar Energy Materials. *Journal of the Electrochemical Society* **2011**, *158* (5), H554-H560.
151. Venkatram, N.; Batabyal, S. K.; Tian, L.; Vittal, J. J.; Ji, W., Shape-dependent nonlinear absorption and relaxation in CuInS<sub>2</sub> nanocrystals. *Appl. Phys. Lett.* **2009**, *95* (20).
152. Ludwig, J.; An, L.; Pattengale, B.; Kong, Q. Y.; Zhang, X. Y.; Xi, P. X.; Huang, J. E., Ultrafast Hole Trapping and Relaxation Dynamics in p-Type CuS Nanodisks. *J. Phys. Chem. Lett.* **2015**, *6* (14), 2671-2675.
153. Patrick, R. A. D.; Mosselmans, J. F. W.; Charnock, J. M.; England, K. E. R.; Helz, G. R.; Garner, C. D.; Vaughan, D. J., The structure of amorphous copper sulfide precipitates: An X-ray absorption study. *Geochimica Et Cosmochimica Acta* **1997**, *61* (10), 2023-2036.
154. Kau, L. S.; Spirasolomon, D. J.; Pennerhahn, J. E.; Hodgson, K. O.; Solomon, E. I., X-RAY ABSORPTION-EDGE DETERMINATION OF THE OXIDATION-STATE AND COORDINATION-NUMBER OF COPPER - APPLICATION TO THE TYPE-3

SITE IN RHUS-VERNICIFERA LACCASE AND ITS REACTION WITH OXYGEN. *J. Am. Chem. Soc.* **1987**, *109* (21), 6433-6442.

155. Pattengale, B.; Ludwig, J.; Huang, J., Atomic Insight into the W-Doping Effect on Carrier Dynamics and Photoelectrochemical Properties of BiVO<sub>4</sub> Photoanodes. *J. Phys. Chem. C* **2016**, *120* (3), 1421-1427.

156. Rao, M. J.; Shibata, T.; Chattopadhyay, S.; Nag, A., Origin of Photoluminescence and XAFS Study of (ZnS)<sub>(1-x)</sub>(AgInS<sub>2</sub>)<sub>x</sub> Nanocrystals. *J. Phys. Chem. Lett.* **2014**, *5* (1), 167-173.

157. Nag, A.; Chung, D. S.; Dolzhenkov, D. S.; Dimitrijevic, N. M.; Chattopadhyay, S.; Shibata, T.; Talpin, D. V., Effect of Metal Ions on Photoluminescence, Charge Transport, Magnetic and Catalytic Properties of All-Inorganic Colloidal Nanocrystals and Nanocrystal Solids. *J. Am. Chem. Soc.* **2012**, *134* (33), 13604-13615.

158. Aiga, N.; Jia, Q. X.; Watanabe, K.; Kudo, A.; Sugimoto, T.; Matsumoto, Y., Electron-Phonon Coupling Dynamics at Oxygen Evolution Sites of Visible-Light-Driven Photocatalyst: Bismuth Vanadate. *J. Phys. Chem. C* **2013**, *117* (19), 9881-9886.

159. Huang, Z. Q.; Lin, Y. J.; Xiang, X.; Rodriguez-Cordoba, W.; McDonald, K. J.; Hagen, K. S.; Choi, K. S.; Brunschwig, B. S.; Musaev, D. G.; Hill, C. L.; Wang, D. W.; Lian, T. Q., In situ probe of photocarrier dynamics in water-splitting hematite (alpha-Fe<sub>2</sub>O<sub>3</sub>) electrodes. *Energy Environ. Sci* **2012**, *5* (10), 8923-8926.

160. Hassan, A.; Zhang, X. Y.; Liu, X. H.; Rowland, C. E.; Jawaid, A. M.; Chattopadhyay, S.; Gulec, A.; Shamirian, A.; Zuo, X. B.; Klie, R. F.; Schaller, R. D.; Snee, P. T., Charge Carriers Modulate the Bonding of Semiconductor Nanoparticle Dopants As Revealed by Time-Resolved X-ray Spectroscopy. *ACS Nano* **2017**, *11* (10), 10070-10076.

161. Tsuji, I.; Kato, H.; Kudo, A., Visible-light-induced H<sub>2</sub> evolution from an aqueous solution containing sulfide and sulfite over a ZnS-CuInS<sub>2</sub>-AgInS<sub>2</sub> solid-solution photocatalyst. *Angew. Chem. Int. Ed.* **2005**, *44* (23), 3565-3568.

162. Mills, A.; Davies, R. H.; Worsley, D., Water purification by semiconductor photocatalysis. *Chem. Soc. Rev* **1993**, *22* (6), 417-425.

163. Oregan, B.; Gratzel, M., A low-cost, high-efficiency solar cell based on dye-sensitized colloidal TiO<sub>2</sub> films. *Nature* **1991**, *353* (6346), 737-740.

164. Lian, S. C.; Kodaimati, M. S.; Dolzhenkov, D. S.; Calzada, R.; Weiss, E. A., Powering a CO<sub>2</sub> Reduction Catalyst with Visible Light through Multiple Sub-picosecond Electron Transfers from a Quantum Dot. *J. Am. Chem. Soc.* **2017**, *139* (26), 8931-8938.

165. Li, X. X.; Xie, K. Y.; Song, L.; Zhao, M. J.; Zhang, Z. P., Enhanced Photocarrier Separation in Hierarchical Graphitic-C<sub>3</sub>N<sub>4</sub>-Supported CuInS<sub>2</sub> for Noble-Metal-Free Z-Scheme Photocatalytic Water Splitting. *ACS Appl. Mater. Interfaces* **2017**, *9* (29), 24577-24583.

166. Zhang, B. T.; Wang, Y. C.; Yang, C. B.; Hu, S. Y.; Gao, Y.; Zhang, Y. P.; Wang, Y.; Demir, H. V.; Liub, L. W.; Yong, K. T., The composition effect on the optical properties of aqueous synthesized Cu-In-S and Zn-Cu-In-S quantum dot nanocrystals. *Phys. Chem. Chem. Phys* **2015**, *17* (38), 25133-25141.
167. Kuo, K. T.; Liu, D. M.; Chen, S. Y.; Lin, C. C., Core-shell CuInS<sub>2</sub>/ZnS quantum dots assembled on short ZnO nanowires with enhanced photo-conversion efficiency. *J. Mater. Chem* **2009**, *19* (37), 6780-6788.
168. Tsuji, I.; Kato, H.; Kobayashi, H.; Kudo, A., Photocatalytic H<sub>2</sub> evolution under visible-light irradiation over band-structure-controlled (CuIn)<sub>x</sub>Zn<sub>2(1-x)</sub>S<sub>2</sub> solid solutions. *J. Phys. Chem. B* **2005**, *109* (15), 7323-7329.
169. Yuan, Y. J.; Chen, D. Q.; Huang, Y. W.; Yu, Z. T.; Zhong, J. S.; Chen, T. T.; Tu, W. G.; Guan, Z. J.; Cao, D. P.; Zou, Z. G., MoS<sub>2</sub> Nanosheet-Modified CuInS<sub>2</sub> Photocatalyst for Visible Light-Driven Hydrogen Production from Water. *ChemSusChem* **2016**, *9* (9), 1003-1009.
170. Iwase, A.; Yoshino, S.; Takayama, T.; Ng, Y. H.; Amal, R.; Kudo, A., Water Splitting and CO<sub>2</sub> Reduction under Visible Light Irradiation Using Z-Scheme Systems Consisting of Metal Sulfides, CoO<sub>x</sub>-Loaded BiVO<sub>4</sub>, and a Reduced Graphene Oxide Electron Mediator. *J. Am. Chem. Soc.* **2016**, *138* (32), 10260-10264.
171. Iwashina, K.; Iwase, A.; Ng, Y. H.; Amal, R.; Kudo, A., Z-Schematic Water Splitting into H<sub>2</sub> and O<sub>2</sub> Using Metal Sulfide as a Hydrogen-Evolving Photocatalyst and Reduced Graphene Oxide as a Solid-State Electron Mediator. *J. Am. Chem. Soc.* **2015**, *137* (2), 604-607.
172. Kaneko, H.; Minegishi, T.; Nakabayashi, M.; Shibata, N.; Kuang, Y. B.; Yamada, T.; Domen, K., A Novel Photocathode Material for Sunlight-Driven Overall Water Splitting: Solid Solution of ZnSe and Cu(In,Ga)Se<sub>2</sub>. *Advanced Functional Materials* **2016**, *26* (25), 4570-4577.
173. Chuang, P. H.; Lin, C. C.; Liu, R. S., Emission-Tunable CuInS<sub>2</sub>/ZnS Quantum Dots: Structure, Optical Properties, and Application in White Light-Emitting Diodes with High Color Rendering Index. *ACS Appl. Mater. Interfaces* **2014**, *6* (17), 15379-15387.
174. Ueng, H. Y.; Hwang, H. L., The defect structure of CuInS<sub>2</sub>. part I: Intrinsic defects. *J. Phys. Chem. Solids* **1989**, *50* (12), 1297-1305.
175. Omata, T.; Nose, K.; Kurimoto, K.; Kita, M., Electronic transition responsible for size-dependent photoluminescence of colloidal CuInS<sub>2</sub> quantum dots. *J. Mater. Chem. C* **2014**, *2* (33), 6867-6872.
176. Nose, K.; Omata, T.; Otsuka-Yao-Matsuo, S., Colloidal Synthesis of Ternary Copper Indium Diselenide Quantum Dots and Their Optical Properties. *J. Phys. Chem. C* **2009**, *113* (9), 3455-3460.

177. Liu, W. Y.; Zhang, Y.; Zhao, J.; Feng, Y.; Wang, D.; Zhang, T. Q.; Gao, W. Z.; Chu, H. R.; Yin, J. Z.; Wang, Y. D.; Zhao, J.; Yu, W. W., Photoluminescence of indium-rich copper indium sulfide quantum dots. *Journal of Luminescence* **2015**, *162*, 191-196.
178. Gelderman, K.; Lee, L.; Donne, S. W., Flat-band potential of a semiconductor: using the Mott-Schottky equation. *Journal of Chemical Education* **2007**, *84* (4), 685-688.
179. Kim, Y. K.; Ahn, S. H.; Chung, K.; Cho, Y. S.; Choi, C. J., The photoluminescence of CuInS<sub>2</sub> nanocrystals: effect of non-stoichiometry and surface modification. *J. Mater. Chem* **2012**, *22* (4), 1516-1520.
180. Uehara, M.; Watanabe, K.; Tajiri, Y.; Nakamura, H.; Maeda, H., Synthesis of CuInS<sub>2</sub> fluorescent nanocrystals and enhancement of fluorescence by controlling crystal defect. *J. Chem. Phys.* **2008**, *129* (13).
181. Hu, W. H.; Ludwig, J.; Pattengale, B.; Yang, S. Z.; Liu, C. M.; Zuo, X. B.; Zhang, X. Y.; Huang, J., Unravelling the Correlation of Electronic Structure and Carrier Dynamics in CuInS<sub>2</sub> Nanoparticles. *J. Phys. Chem. C* **2018**, *122* (1), 974-980.
182. Sakamoto, M.; Chen, L. H.; Okano, M.; Tex, D. M.; Kanemitsu, Y.; Teranishi, T., Photoinduced Carrier Dynamics of Nearly Stoichiometric Oleylamine-Protected Copper Indium Sulfide Nanoparticles and Nanodisks. *J. Phys. Chem. C* **2015**, *119* (20), 11100-11105.
183. Stolle, C. J.; Schaller, R. D.; Korgel, B. A., Efficient Carrier Multiplication in Colloidal CuInSe<sub>2</sub> Nanocrystals. *J. Phys. Chem. Lett.* **2014**, *5* (18), 3169-3174.
184. Li, T. L.; Cai, C. D.; Yeh, T. F.; Teng, H. S., Capped CuInS<sub>2</sub> quantum dots for H<sub>2</sub> evolution from water under visible light illumination. *J. Alloys Compd.* **2013**, *550*, 326-330.
185. Fan, X. B.; Yu, S.; Zhan, F.; Li, Z. J.; Gao, Y. J.; Li, X. B.; Zhang, L. P.; Tao, Y.; Tung, C. H.; Wu, L. Z., Nonstoichiometric Cu<sub>x</sub>In<sub>y</sub>S Quantum Dots for Efficient Photocatalytic Hydrogen Evolution. *ChemSusChem* **2017**, *10* (24), 4833-4838.
186. Han, K.; Wang, M.; Zhang, S.; Wu, S. L.; Yang, Y.; Sun, L. C., Photochemical hydrogen production from water catalyzed by CdTe quantum dots/molecular cobalt catalyst hybrid systems. *ChemComm* **2015**, *51* (32), 7008-7011.
187. Wang, P.; Li, C. P.; Wang, M. M.; Jin, Y. D., Controlled Decoration of Divalent Nickel onto CdS/CdSe Core/Shell Quantum Dots to Boost Visible-Light-Induced Hydrogen Generation in Water. *ChemPlusChem* **2018**, *83* (12), 1088-1096.
188. Liu, X. Y.; Zhang, G. Z.; Chen, H.; Li, H. W.; Jiang, J.; Long, Y. T.; Ning, Z. J., Efficient defect-controlled photocatalytic hydrogen generation based on near-infrared Cu-In-Zn-S quantum dots. *Nano Res.* **2018**, *11* (3), 1379-1388.

189. Peterson, M. D.; Cass, L. C.; Harris, R. D.; Edme, K.; Sung, K.; Weiss, E. A., The Role of Ligands in Determining the Exciton Relaxation Dynamics in Semiconductor Quantum Dots. In *Annual Review of Physical Chemistry, Vol 65*, Johnson, M. A.; Martinez, T. J., Eds. 2014; Vol. 65, pp 317-339.
190. Zhou, H. C.; Long, J. R.; Yaghi, O. M., Introduction to Metal-Organic Frameworks. *Chem. Rev* **2012**, *112* (2), 673-674.
191. James, S. L., Metal-organic frameworks. *Chem. Soc. Rev* **2003**, *32* (5), 276-288.
192. Mueller, U.; Schubert, M.; Teich, F.; Puetter, H.; Schierle-Arndt, K.; Pastre, J., Metal-organic frameworks - prospective industrial applications. *J. Mater. Chem* **2006**, *16* (7), 626-636.
193. Furukawa, H.; Cordova, K. E.; O'Keeffe, M.; Yaghi, O. M., The Chemistry and Applications of Metal-Organic Frameworks. *Science* **2013**, *341* , 1230444.
194. Rowsell, J. L. C.; Yaghi, O. M., Metal-organic frameworks: a new class of porous materials. *Micropor. Mesopor. Mat.* **2004**, *73* (1-2), 3-14.
195. Banerjee, R.; Phan, A.; Wang, B.; Knobler, C.; Furukawa, H.; O'Keeffe, M.; Yaghi, O. M., High-throughput synthesis of zeolitic imidazolate frameworks and application to CO<sub>2</sub> capture. *Science* **2008**, *319* (5865), 939-943.
196. Wang, B.; Cote, A. P.; Furukawa, H.; O'Keeffe, M.; Yaghi, O. M., Colossal cages in zeolitic imidazolate frameworks as selective carbon dioxide reservoirs. *Nature* **2008**, *453* (7192), 207-U6.
197. Shi, Q.; Chen, Z. F.; Song, Z. W.; Li, J. P.; Dong, J. X., Synthesis of ZIF-8 and ZIF-67 by Steam-Assisted Conversion and an Investigation of Their Tribological Behaviors. *Angew. Chem. Int. Ed.* **2011**, *50* (3), 672-675.
198. Chaikittisilp, W.; Torad, N. L.; Li, C. L.; Imura, M.; Suzuki, N.; Ishihara, S.; Ariga, K.; Yamauchi, Y., Synthesis of Nanoporous Carbon- Cobalt- Oxide Hybrid Electrocatalysts by Thermal Conversion of Metal- Organic Frameworks. *Chem. Eur. J.* **2014**, *20* (15), 4217-4221.
199. Hu, Y.; Liu, Z. X.; Xu, J.; Huang, Y. N.; Song, Y., Evidence of Pressure Enhanced CO<sub>2</sub> Storage in ZIF-8 Probed by FTIR Spectroscopy. *J. Am. Chem. Soc.* **2013**, *135* (25), 9287-9290.
200. Zhong, G. H.; Liu, D. X.; Zhang, J. Y., The application of ZIF-67 and its derivatives: adsorption, separation, electrochemistry and catalysts. *J. Mater. Chem. A* **2018**, *6* (5), 1887-1899.
201. Koyuturk, B.; Altintas, C.; Kinik, F. P.; Keskin, S.; Uzun, A., Improving Gas Separation Performance of ZIF-8 by BMIM BF<sub>4</sub> Incorporation: Interactions and Their Consequences on Performance. *J. Phys. Chem. C* **2017**, *121* (19), 10370-10381.

202. Zhu, M. Q.; Srinivas, D.; Bhogeswararao, S.; Ratnasamy, P.; Carreon, M. A., Catalytic activity of ZIF-8 in the synthesis of styrene carbonate from CO<sub>2</sub> and styrene oxide. *Catal. Commun.* **2013**, *32*, 36-40.
203. Lin, K. Y. A.; Chang, H. A., Zeolitic Imidazole Framework-67 (ZIF-67) as a heterogeneous catalyst to activate peroxymonosulfate for degradation of Rhodamine B in water. *J Taiwan Inst Chem Eng.* **2015**, *53*, 40-45.
204. Kuo, C. H.; Tang, Y.; Chou, L. Y.; Sneed, B. T.; Brodsky, C. N.; Zhao, Z. P.; Tsung, C. K., Yolk-Shell Nanocrystal@ZIF-8 Nanostructures for Gas-Phase Heterogeneous Catalysis with Selectivity Control. *J. Am. Chem. Soc.* **2012**, *134* (35), 14345-14348.
205. Jiang, Z.; Li, Z. P.; Qin, Z. H.; Sun, H. Y.; Jiao, X. L.; Chen, D. R., LDH nanocages synthesized with MOF templates and their high performance as supercapacitors. *Nanoscale* **2013**, *5* (23), 11770-11775.
206. Yang, H.; Kruger, P. E.; Telfer, S. G., Metal-Organic Framework Nanocrystals as Sacrificial Templates for Hollow and Exceptionally Porous Titania and Composite Materials. *Inorg. Chem.* **2015**, *54* (19), 9483-9490.
207. Li, J. J.; Xia, W.; Tang, J.; Tan, H. B.; Wang, J. Y.; Kaneti, Y. V.; Bando, Y.; Wang, T.; He, J. P.; Yamauchi, Y., MOF nanoleaves as new sacrificial templates for the fabrication of nanoporous Co-N-x/C electrocatalysts for oxygen reduction. *Nanoscale Horiz* **2019**, *4* (4), 1006-1013.
208. Thompson, J. A.; Blad, C. R.; Brunelli, N. A.; Lydon, M. E.; Lively, R. P.; Jones, C. W.; Nair, S., Hybrid Zeolitic Imidazolate Frameworks: Controlling Framework Porosity and Functionality by Mixed-Linker Synthesis. *Chem. Mater.* **2012**, *24* (10), 1930-1936.
209. Thompson, J. A.; Vaughn, J. T.; Brunelli, N. A.; Koros, W. J.; Jones, C. W.; Nair, S., Mixed-linker zeolitic imidazolate framework mixed-matrix membranes for aggressive CO<sub>2</sub> separation from natural gas. *Micropor. Mesopor. Mat.* **2014**, *192*, 43-51.
210. Jayachandrababu, K. C.; Sholl, D. S.; Nair, S., Structural and Mechanistic Differences in Mixed-Linker Zeolitic Imidazolate Framework Synthesis by Solvent Assisted Linker Exchange and de Novo Routes. *J. Am. Chem. Soc.* **2017**, *139* (16), 5906-5915.
211. Niyazymbetov, M. E.; Evans, D. H., OXIDATION POTENTIAL AS A MEASURE OF THE EFFECT OF ENVIRONMENT ON THE REACTIVITY OF ANIONIC NUCLEOPHILES. *Journal of the Chemical Society-Perkin Transactions 2* **1993**, (7), 1333-1338.
212. Niyazymbetov, M. E.; Zhou, R. F.; Evans, D. H., Oxidation potential as a measure of the reactivity of anionic nucleophiles. Behaviour of different classes of nucleophiles. *Journal of the Chemical Society-Perkin Transactions 2* **1996**, (9), 1957-1961.

213. Xia, W.; Zhu, J. H.; Guo, W. H.; An, L.; Xia, D. G.; Zou, R. Q., Well-defined carbon polyhedrons prepared from nano metal-organic frameworks for oxygen reduction. *J. Mater. Chem. A* **2014**, *2* (30), 11606-11613.
214. Simmance, K.; Sankar, G.; Bell, R. G.; Prestipino, C.; van Beek, W., Tracking the formation of cobalt substituted ALPO-5 using simultaneous in situ X-ray diffraction and X-ray absorption spectroscopy techniques. *Phys. Chem. Chem. Phys* **2010**, *12* (3), 559-562.
215. George, S. D.; Brant, P.; Solomon, E. I., Metal and ligand K-Edge XAS of organotitanium complexes: Metal 4p and 3d contributions to pre-edge intensity and their contributions to bonding. *J. Am. Chem. Soc.* **2005**, *127* (2), 667-674.
216. Yi, J.; Nakatani, N.; Nomura, K.; Hada, M., Time-dependent DFT study of the K-edge spectra of vanadium and titanium complexes: effects of chloride ligands on pre-edge features. *Phys. Chem. Chem. Phys* **2020**, *22* (2), 674-682.
217. Trujillano, R.; Villain, F.; Louis, C.; Lambert, J. F., Chemistry of silica-supported cobalt catalysts prepared by cation adsorption. 1. Initial localized adsorption of cobalt precursors. *J. Phys. Chem. C* **2007**, *111* (19), 7152-7164.
218. Frenzel-Beyme, L.; Kloss, M.; Kolodzeiski, P.; Pallach, R.; Henke, S., Melttable Mixed-Linker Zeolitic Imidazolate Frameworks and Their Microporous Glasses: From Melting Point Engineering to Selective Hydrocarbon Sorption. *J. Am. Chem. Soc.* **2019**, *141* (31), 12362-12371.
219. Wang, C.; deKrafft, K. E.; Lin, W. B., Pt Nanoparticles@Photoactive Metal-Organic Frameworks: Efficient Hydrogen Evolution via Synergistic Photoexcitation and Electron Injection. *J. Am. Chem. Soc.* **2012**, *134* (17), 7211-7214.
220. Shen, L. J.; Luo, M. B.; Huang, L. J.; Feng, P. Y.; Wu, L., A Clean and General Strategy To Decorate a Titanium Metal Organic Framework with Noble-Metal Nanoparticles for Versatile Photocatalytic Applications. *Inorg. Chem.* **2015**, *54* (4), 1191-1193.
221. Kato, H.; Akimoto, K., MAGNETIC CIRCULAR-DICHROISM SPECTRA OF SOME TETRAHEDRAL COBALT(II) COMPLEXES. *J. Am. Chem. Soc.* **1974**, *96* (5), 1351-1357.
222. Zhou, Y. X.; Hu, W. H.; Yang, S. Z.; Huang, J., Enhanced light harvesting ability in zeolitic imidazolate frameworks through energy transfer from CdS nanowires. *Phys. Chem. Chem. Phys* **2020**, *22* (7), 3849-3854.
223. Swathi, R. S.; Sebastian, K. L., Distance dependence of fluorescence resonance energy transfer. *J. Chem. Sci* **2009**, *121* (5), 777-787.
224. Narayanan, R.; Deepa, M.; Srivastava, A. K., Forster resonance energy transfer and carbon dots enhance light harvesting in a solid-state quantum dot solar cell. *J. Mater. Chem. A* **2013**, *1* (12), 3907-3918.

225. Zhou, H. T.; Qin, C. B.; Chen, R. Y.; Zhou, W. J.; Zhang, G. F.; Gao, Y.; Xiao, L. T.; Jia, S. T., Accurate Investigation on the Fluorescence Resonance Energy Transfer between Single Organic Molecules and Monolayer WSe<sub>2</sub> by Quantum Coherent Modulation-Enhanced Single-Molecule Imaging Microscopy. *J. Phys. Chem. Lett.* **2019**, *10* (11), 2849-2856.
226. Dale, R. E.; Eisinger, J., Intramolecular distances determined by energy transfer. Dependence on orientational freedom of donor and acceptor. *Biopolymers* **1974**, *13* (8), 1573-1605.
227. Albinsson, B.; Eng, M. P.; Pettersson, K.; Winters, M. U., Electron and energy transfer in donor-acceptor systems with conjugated molecular bridges. *Phys. Chem. Chem. Phys.* **2007**, *9* (44), 5847-5864.
228. Sabanayagam, C. R.; Eid, J. S.; Meller, A., Using fluorescence resonance energy transfer to measure distances along individual DNA molecules: Corrections due to nonideal transfer. *J. Chem. Phys.* **2005**, *122* (6).
229. Deniz, A. A.; Dahan, M.; Grunwell, J. R.; Ha, T. J.; Faulhaber, A. E.; Chemla, D. S.; Weiss, S.; Schultz, P. G., Single-pair fluorescence resonance energy transfer on freely diffusing molecules: Observation of Forster distance dependence and subpopulations. *Proc. Natl. Acad. Sci. U.S.A* **1999**, *96* (7), 3670-3675.
230. Sekar, R. B.; Periasamy, A., Fluorescence resonance energy transfer (FRET) microscopy imaging of live cell protein localizations. *J. Cell Biol.* **2003**, *160* (5), 629-633.
231. Federspiel, F.; Froehlicher, G.; Nasilowski, M.; Pedetti, S.; Mahmood, A.; Doudin, B.; Park, S.; Lee, J. O.; Halley, D.; Dubertret, B.; Gilliot, P.; Berciaud, S., Distance Dependence of the Energy Transfer Rate from a Single Semiconductor Nanostructure to Graphene. *Nano Lett.* **2015**, *15* (2), 1252-1258.
232. Swathi, R. S.; Sebastian, K. L., Long range resonance energy transfer from a dye molecule to graphene has (distance)<sup>-4</sup> dependence. *J. Chem. Phys.* **2009**, *130* (8), 086101.
233. Park, T.; Kim, H.; Leem, M.; Ahn, W.; Choi, S.; Kim, J.; Uh, J.; Kwon, K.; Jeong, S. J.; Park, S.; Kim, Y.; Kim, H., Atomic layer deposition of Al<sub>2</sub>O<sub>3</sub> on MoS<sub>2</sub>, WS<sub>2</sub>, WSe<sub>2</sub>, and h-BN: surface coverage and adsorption energy. *RSC Adv.* **2017**, *7* (2), 884-889.
234. Vandalon, V.; Kessels, W., Initial Growth Study of Atomic-Layer Deposition of Al<sub>2</sub>O<sub>3</sub> by Vibrational Sum-Frequency Generation. *Langmuir* **2019**, *35* (32), 10374-10382.
235. Ylivaara, O. M. E.; Liu, X. W.; Kilpi, L.; Lyytinen, J.; Schneider, D.; Laitinen, M.; Julin, J.; Ali, S.; Sintonen, S.; Berdova, M.; Haimi, E.; Sajavaara, T.; Ronkainen, H.; Lipsanen, H.; Koskinen, J.; Hannula, S. P.; Puurunen, R. L., Aluminum oxide from trimethylaluminum and water by atomic layer deposition: The temperature dependence of residual stress, elastic modulus, hardness and adhesion. *Thin Solid Films* **2014**, *552*, 124-135.

236. Kallioinen, J.; Benko, G.; Sundstrom, V.; Korppi-Tommola, J. E. I.; Yartsev, A. P., Electron transfer from the singlet and triplet excited states of Ru(dcbpy)(2)(NCS)(2) into nanocrystalline TiO2 thin films. *J. Phys. Chem. B* **2002**, *106* (17), 4396-4404.
237. Damrauer, N. H.; Cerullo, G.; Yeh, A.; Boussie, T. R.; Shank, C. V.; McCusker, J. K., Femtosecond dynamics of excited-state evolution in Ru(bpy)(3) (2+). *Science* **1997**, *275* (5296), 54-57.
238. Asbury, J. B.; Ellingson, R. J.; Ghosh, H. N.; Ferrere, S.; Nozik, A. J.; Lian, T. Q., Femtosecond IR study of excited-state relaxation and electron-injection dynamics of Ru(dcbpy)(2)(NCS)(2) in solution and on nanocrystalline TiO2 and Al2O3 thin films. *J. Phys. Chem. B* **1999**, *103* (16), 3110-3119.
239. Flender, O.; Scholz, M.; Klein, J. R.; Oum, K.; Lenzer, T., Excited-state relaxation of the solar cell dye D49 in organic solvents and on mesoporous Al2O3 and TiO2 thin films. *Phys. Chem. Chem. Phys* **2016**, *18* (37), 26010-26019.
240. Fakis, M.; Hrobarik, P.; Yushchenko, O.; Sigmundova, I.; Koch, M.; Rosspeintner, A.; Stathatos, E.; Vauthey, E., Excited State and Injection Dynamics of Triphenylamine Sensitizers Containing a Benzothiazole Electron-Accepting Group on TiO2 and Al2O3 Thin Films. *J. Phys. Chem. C* **2014**, *118* (49), 28509-28519.
241. Rehorek, M.; Dencher, N. A.; Heyn, M. P., Long-Range Lipid-Protein Interactions. Evidence from Time-Resolved Fluorescence Depolarization and Energy-Transfer Experiments with Bacteriorhodopsin-Dimyristoylphosphatidylcholine Vesicles. *Biochemistry* **1985**, *24* (21), 5980-5988.
242. Ramos-Ortiz, G.; Oki, Y.; Domercq, B.; Kippelen, B., Forster energy transfer from a fluorescent dye to a phosphorescent dopant: a concentration and intensity study. *Phys. Chem. Chem. Phys* **2002**, *4* (17), 4109-4114.
243. Lee, B. R.; Lee, W.; Nguyen, T. L.; Park, J. S.; Kim, J. S.; Kim, J. Y.; Woo, H. Y.; Song, M. H., Highly Efficient Red-Emitting Hybrid Polymer Light-Emitting Diodes via Forster Resonance Energy Transfer Based on Homogeneous Polymer Blends with the Same Polyfluorene Backbone. *ACS Appl. Mater. Interfaces* **2013**, *5* (12), 5690-5695.
244. Zhang, X.; Marocico, C. A.; Lunz, M.; Gerard, V. A.; Gun'ko, Y. K.; Lesnyak, V.; Gaponik, N.; Susha, A. S.; Rogach, A. L.; Bradley, A. L., Experimental and Theoretical Investigation of the Distance Dependence of Localized Surface Plasmon Coupled Forster Resonance Energy Transfer. *ACS Nano* **2014**, *8* (2), 1273-1283.
245. Ran, J. R.; Jaroniec, M.; Qiao, S. Z., Cocatalysts in Semiconductor-based Photocatalytic CO2 Reduction: Achievements, Challenges, and Opportunities. *Adv. Mater.* **2018**, *30* (7).
246. Gueret, R.; Poulard, L.; Oshinowo, M.; Chauvin, J.; Dahmane, M.; Dupeyre, G.; Laine, P. P.; Fortage, J.; Collomb, M. N., Challenging the Ru(bpy)(3) (2+) Photosensitizer

with a Triazatriangulenium Robust Organic Dye for Visible-Light-Driven Hydrogen Production in Water. *ACS Catal.* **2018**, *8* (5), 3792-3802.

247. Yang, S. Z.; Pattengale, B.; Lee, S.; Huang, J., Real-Time Visualization of Active Species in a Single-Site Metal-Organic Framework Photocatalyst. *ACS Energy Lett.* **2018**, *3* (3), 532-539.

248. Yang, S. Z.; Fan, D. H.; Hu, W. H.; Pattengale, B.; Liu, C. M.; Zhang, X. Y.; Huang, J. E., Elucidating Charge Separation Dynamics in a Hybrid Metal-Organic Framework Photocatalyst for Light-Driven H<sub>2</sub> Evolution. *J. Phys. Chem. C* **2018**, *122* (6), 3305-3311.

249. Morabito, J. V.; Chou, L. Y.; Li, Z. H.; Manna, C. M.; Petroff, C. A.; Kyada, R. J.; Palomba, J. M.; Byers, J. A.; Tsung, C. K., Molecular Encapsulation beyond the Aperture Size Limit through Dissociative Linker Exchange in Metal-Organic Framework Crystals. *J. Am. Chem. Soc.* **2014**, *136* (36), 12540-12543.

250. Dobryakov, A. L.; Kovalenko, S. A.; Ernsting, N. P., Coherent and sequential contributions to femtosecond transient absorption spectra of a rhodamine dye in solution. *J. Chem. Phys.* **2005**, *123* (4).

251. Boulesbaa, A.; Issac, A.; Stockwell, D.; Huang, Z.; Huang, J.; Guo, J.; Lian, T., Ultrafast charge separation at CdS quantum dot/rhodamine B molecule interface. *J. Am. Chem. Soc.* **2007**, *129* (49), 15132-15133.

252. Hu, W. H.; Yang, F.; Pietraszak, N.; Gu, J.; Huang, J. E., Distance dependent energy transfer dynamics from a molecular donor to a zeolitic imidazolate framework acceptor. *Phys. Chem. Chem. Phys.* **2020**, *22* (44), 25445-25449.

253. Masciocchi, N.; Bruni, S.; Cariati, E.; Cariati, F.; Galli, S.; Sironi, A., Extended polymorphism in copper(II) imidazolate polymers: A spectroscopic and XRPD structural study. *Inorg. Chem.* **2001**, *40* (23), 5897-5905.

254. Li, R.; Ren, X. Q.; Ma, H. W.; Feng, X.; Lin, Z. G.; Li, X. G.; Hu, C. W.; Wang, B., Nickel-substituted zeolitic imidazolate frameworks for time-resolved alcohol sensing and photocatalysis under visible light. *J. Mater. Chem. A* **2014**, *2* (16), 5724-5729.

255. Tian, Y. Q.; Yao, S. Y.; Gu, D.; Cui, K. H.; Guo, D. W.; Zhang, G.; Chen, Z. X.; Zhao, D. Y., Cadmium Imidazolate Frameworks with Polymorphism, High Thermal Stability, and a Large Surface Area. *Chem. Eur. J.* **2010**, *16* (4), 1137-1141.

256. Park, K. S.; Ni, Z.; Cote, A. P.; Choi, J. Y.; Huang, R. D.; Uribe-Romo, F. J.; Chae, H. K.; O'Keeffe, M.; Yaghi, O. M., Exceptional chemical and thermal stability of zeolitic imidazolate frameworks. *Proc. Natl. Acad. Sci. U.S.A* **2006**, *103* (27), 10186-10191.

257. Morris, W.; Leung, B.; Furukawa, H.; Yaghi, O. K.; He, N.; Hayashi, H.; Houndonougbo, Y.; Asta, M.; Laird, B. B.; Yaghi, O. M., A Combined Experimental-Computational Investigation of Carbon Dioxide Capture in a Series of Isorecticular Zeolitic Imidazolate Frameworks. *J. Am. Chem. Soc.* **2010**, *132* (32), 11006-11008.